A High Performance Micromachined Sub-Millimeter-Wave Radar Technology

by

Armin Jam

**A dissertation submitted in partial fulfillment
of the requirements for the degree of
Doctor of Philosophy
(Electrical Engineering)
in The University of Michigan
2017**

Doctoral Committee:

**Professor Kamal Sarabandi, Chair
Associate Professor Ehsan Afshari
Professor Mark A. Burns
Emeritus Research Scientist Jack R. East
Professor Anthony Grbic**

Armin Jam

arminjam@umich.edu

ORCID iD: 0000-0001-6244-5134

© Armin Jam

2017 All Rights Reserved

To my family with love and gratitude

ACKNOWLEDGEMENTS

First and foremost, I am most grateful to my family for their unconditional love, support, and sacrifices. My greatest gratitude to my parents, Faranak and Mohammad, to whom I owe everything, and to my little sister, Anahita, for being the best sister ever. Most importantly, I am forever indebted to my best friend and the love of my life, Avish, for all the late nights and early mornings and for always being there for me. I also want to thank my in-laws, Soheila and Zia, and my grandmother, Parvin, for their love and support. It is for all of this that I dedicate this dissertation to them.

I would like to acknowledge and express my gratitude towards many people who contributed to my academic success, from my first grade teacher to my Ph.D. advisor, to only some of whom it is possible to give particular mention here. I would first like to sincerely thank my research advisor, Professor Kamal Sarabandi. This has been a prodigious experience, and I am grateful for his continuous guidance, support, and encouragement. It has been an honor to be his student. I am also very thankful to Dr. Jack East for his valuable guidance and mentorship throughout my research endeavors. I am certainly going to miss our Friday morning meeting conversations! I also would like to extend my gratitude to Professor Ehsan Afshari, Professor Mark Burns, and Professor Anthony Grbic for their precious time and valuable advice while serving as my dissertation committee members. It has been an honor and privilege to have you on my committee. I also would like to thank my undergraduate advisor, Professor Esfandiar Mehrshahi,

for teaching me the foundations of electromagnetics and for his contagious passion for science and engineering.

I would like to take the opportunity to thank current and former colleagues, staff, and friends at the Radiation Laboratory of the University of Michigan for providing a friendly and productive research environment. I specifically would like to thank Dr. Mehrnoosh Vahidpour, Dr. Meysam Moallem, Dr. Brian Tierney, Amr Alaa, and Michael Benson for all their technical discussions and collaborations. I would also like to thank Dr. Adib Nashashibi and Dr. Leland Pierce for their helping hand whenever needed.

The experimental research of this work would not have been accomplished if it was not for the technical support of the friendly staff and colleagues at the Lurie Nanofabrication Facility at the University of Michigan. I am grateful for their valuable ideas and comments in development of fabrication processes and their mentorship, specifically in early stages of my microfabrication process.

I am truly blessed to be surrounded by wonderful friends, whom made Ann Arbor home away from home for me. Much gratitude for their priceless friendships and love, and all the good memories I shared with them.

Go Blue!

TABLE OF CONTENTS

Dedication……………………………………………………………………………………...ii

Acknowledgments……………………………………………………………………….....iii

List of Figures……………………………………………………………………………...vii

List of Tables………………………………………………………………………………xvi

List of Abbreviations……………………………………………………………………..xvii

Abstract…………………………………………………………………………………xviii

CHAPTER 1 Introduction……..……….……………………………………………….….1

1.1 Motivation………………………………………………………………………2
1.2 Applications……………………………………………………………………5
1.3 History and Background………………………………………………………11
1.4 Proposed sub-MMW Radar Technology………………………………………17
1.5 Overview of the Dissertation…………………………………………………..…20

CHAPTER 2 Co-Polarized Beam Steering Radar Antenna Design……………….………...24

2.1 Antenna Configuration Overview……………………………………………..…26
2.2 One-Dimensional Antenna Array Design……………………………………...29
2.3 Two Dimensional Antenna Array Design……………………………………...35
2.4 Simulation of the Beam-Steering Array Antenna and Summary of the Radiation Characteristics...44
2.5 Summary……………………………………………………………............47

CHAPTER 3 Cross-Polarized Beam Steering Radar Antenna Design…………...…………48

3.1 Antenna Design……………………………………………………………….….49
3.2 Simulation of the Complete Horizontally-Polarized Patch Array Antenna..…….55
3.3 Summary………………………………………………………….………...57

CHAPTER 4 Chip Integration and Packaging………………………………..……………59

4.1 Packaging Structure and Design ………………………………………………61
4.2 Bias Network and Broadband RF-Choke Design.…………………………….…65
4.3 Packaging Sensitivity Analysis.…………………………………………………67
4.4 Summary.……………………………………………………………….…..69

CHAPTER 5 Microfabrication Processes…...……………………………………………...70

5.1 Bottom Wafer……………….…………………………………………………71
5.2 Top Wafer…………………………………………………………….… 76
5.3 Gold Deposition and Bonding.…………………………………………………...77
5.4 Patch Array Elements over the Membrane.………………………………………79
5.5 Side-Wall Smoothing.………………………………………………………....82
5.6 RF Front-End Prototype.……………………………………………………....86
5.7 Summary.…………………………………………………….........................88

CHAPTER 6 Measurement Techniques………..…………………………………………...90

6.1 On-wafer S-Parameter Measurement……………………………………………91
6.2 Proposed Non-Contact On-wafer Waveguide Measurement Method……………93
6.3 Antenna On-wafer 3-D Pattern Measurement…………………………….….105
6.4 Near-field Antenna Gain Measurement Method……………………………...116
6.5 Chip Package Measurements…………………………………………………124
6.6 Summary………………………………………………………………….…128

CHAPTER 7 Concluding Remarks ……………………………………………………..131

7.1 Summary of Contributions.…………………………………………….…131
7.2 Future Directions.……………………………………………….……….....134

Bibliography………………………………………..136

LIST OF FIGURES

1.1 Some of the spectral content in the submillimeter band for an interstellar cloud (Reprinted from [4])…………………………………………………………………………...3

1.2 Atmospheric attenuation at sea level pressures for various different conditions of temperature, humidity, and atmospheric particulates. The graph shows the atmospheric windows with unrestricted bandwidths at high MMW and sub-MMW frequencies, suitable for applications ranging from high data-rate communications to high-resolution imaging (modified reprint from [6]). ……………………………………………………………4

1.3 Measured attenuation versus visibility at optical frequencies under (a) fog, and (b) smoke conditions. (Reprinted from [23]). ………………………………………………………...5

1.4 Autonomous vehicles offer significant benefits to our welfare: (a) saving lives and reducing crashes; (b) increasing mobility for the disabled people; and (c) improving land use as well as reducing congestion, fuel consumption, and pollution are some instances of the benefits of this technology. ……………………………………………………………………...6

1.5 An overview of a state of the art self-driving car equipped with multiple different sensors for reliable navigation. The sensors are often too bulky, heavy, and power hungry, which makes them not suitable for ubiquitous autonomous applications…………………………………………………………………………....7

1.6 Diagram of micro-robotic platforms: (a) a micro quadcopter drone, and (b) a miniature mechanical bat for autonomous micro robotic applications. The navigation sensors for such miniature robotic platforms are required to have a low size, weight and power consumption (SWaP) with all-weather functionality. …………………………………………………..8

1.7 Applications of micro robotic systems in complex and hazardous environments for both civilian and military purposes. (a) Using micro robotic systems equipped with reliable navigation sensors can replace the role of humans in firefighting, emergency and disaster rescue, etc. (b) Autonomous robotic platforms can be used in various combat scenarios to extract the complete 3D map of the battle field while autonomously navigating itself

through adverse weather conditions (smoke, dust, etc.), and (c) autonomous micro robotics can be used in surveillance and spying applications. ……………………………………..9

1.8 Applications of MMW sensors for security and surveillance. (a) MMW imaging systems used in the public areas such as airports for detection of concealed threatening objects, e.g. weapons and explosives. (b) MMW systems used for surveillance and perimeter security in protected areas. As shown, the sensors currently used are often too bulky, heavy and expensive which makes them less desirable compared to the proposed radar technology……………………………………………………………………………..10

1.9 Stanford Geospatial Center report on the number of victims in the mass shootings in the US from 1966 to 2015 [38]. According to Mass Shootings in America database, an annual average of approximately 70 fatalities have occurred in the US since 2010 (2010-2015). Mass shooting is a global issue that takes hundreds of lives annually. One effective way of preventing mass shootings is to use gun detector sensors in public areas (airports, schools, universities, etc.) to identify and disarm shooters. ………………………………………10

1.10 Examples of MMW systems, (a) a 60 GHz CMOS Doppler radar system with simple patch antennas as the radiators [46], (b) an integrated 77-GHz FMCW CMOS radar with patch array antennas [47], and (c) combination of planar and dish antenna implementation at 94 GHz radar system [49]. Even though, traditional microwave and MMW radar technologies (up to 100 GHz) have well maturated, extension of current technologies to higher MMW and sub-MMW frequencies is very challenging. Some of the challenges pertain to integration of active and passive modules, low antenna efficiencies and gains, complex and costly fabrication requirements, as well as challenges with characterization of these systems at such high frequencies. ……………………………………………………..14

1.11 (a) Photograph of a machined 600 GHz radar imager with reflector lens and mirrors as the radiators [15], and (b) an integrated FMCW radar transceiver module (Left) at 230 GHz with simple horn antennas as radiators (The antenna separation is 21 mm) [60]. The radar modules are machined and assembled accordingly, as shown in the CAD diagram (Right). Although this approach offers robust and reliable integration of radar systems at sub-MMW frequencies, it suffers from high fabrication machining costs of waveguide blocks and antennas. Additionally, these systems are bulky and heavy, and limited to mechanical scanning due to the complexity of the radar RF front-end………………………………16

1.12. (a) Lens-packaged radar transceiver module at 210-270 GHz [63]. The radar chip is mounted on the backside of a hyperhemispherical 9-mm lens made of high-resistivity silicon with the primary on-chip feed antenna aligned with the lens center. (b) Packaged MMIC-based receiver module at 220-GHz [62] with silicon lens antenna. While the lens packaging offers a simple, reliable, and low-cost solution, it is mostly suitable for short-range applications due to the low antenna radiation efficiencies and wide beamwidth.

Moreover, it suffers from limited antenna functionality (i.e. antenna low gain, limited field of view, etc.)……………………………………………………………………………...16

1.13 Schematic diagram of the proposed monolithic beam-steering radar system. The radar system is designed to be compatible with silicon micromachining technology for minimal size, weight, and power consumption (SWaP)……………………………………………19

1.14 Simplified block diagram of the proposed micromachined frequency scanning beam-steering radar system operating at 230-245 GHz…………………………………………19

2.1 Configuration of a travelling wave antenna consisting of (a) a straight segment of a hollow rectangular waveguide with radiating slots placed along its broad wall, (b) a twisted waveguide structure with cuts along the wall of the waveguide, and (c) a meandered planar waveguide structure with radiating slots placed along its wall……………………………28

2.2 Configuration of the one-dimensional beam-steering array antenna, highlighting various design parameters in the array……………………………………………………………29

2.3 Diagram of the (a) curved bend, (b) optimized bend, and (c) full-wave simulated reflection magnitude from the bends…………………………………………………………………..30

2.4 Field distribution along the meandered waveguide structure with adjacent elements excited with (a) l chosen to be a modulus of the waveguide wavelength where adjacent elements are fed 180° out of phase, and (b) l corrected by adding a $\lambda g_0/2$ waveguide segment for in phase feed of the adjacent array elements………………………………………………...32

2.5 Simulated attenuation in the waveguide versus the width of the waveguide for different waveguide height values………………………………………………………………35

2.6 Configuration of a hybrid-coupled patch array where the energy from the meandered waveguide is fed into a patch array placed on top of each slot…………………………..37

2.7 (a) Diagram of the cavity-backed patch array design with the patches patterned on a membrane layer and suspended ~80 μm over the slot, and (b) the slot extended through the top wall with a thickness of 250 μm, coupling to the patch array positioned 80 μm above it……………………………………………………………………………………….38

2.8 (a) Configuration of the cavity-backed patch array with two side-by-side patch arrays positioned per each slot to suppress grating lobe along the azimuth plane. (b) Seven element cavity-backed patch array design to provide 10° of beam confinement along the elevation direction…………………………………………………………………………………40

2.9 (a) Reflection cancellation pillars with optimized dimensions and distance from slots are devised to suppress scan blindness at the center frequency in the beam-steering array. (b)

Comparison between simulated reflection from the slot with and without the reflection cancellation post. Reflection cancellation pillars offer less than -55dB of reflection coefficient at the resonance frequency……………………………………………………43

2.10 Schematic diagram of the complete array antenna with over 600 patch antenna elements as the radiating elements…………………………………………………………………45

2.11 Simulated normalized pattern of the beam-steering array in (a) azimuth plane, and (b) elevation plane……………………………………………………………………….. 46

2.12 Simulated gain, directivity, and radiation efficiency of the beam-steering array over the operation frequency band…………………………………………………………...47

3.1 (a) Diagram of the travelling wave frequency scanning antenna consisting of a meandered waveguide structure with 180˚ H-Plane turns, and (b) the configuration of a single element in the array……………………………………………………………………………..51

3.2 Diagram of the slot-coupled patch array implementation with the patch array elements separated by an inter-element spacing of one wavelength to provide in-phase excitation of all patch elements for bore sight radiation……………………………………………..53

3.3 Schematic diagram of the proposed slot-coupled horizontally-polarized patch array design for beam confinement in the elevation direction. (a) Top view of a single patch array showing flipped configuration of the patch elements with half wavelength inter-element spacing, providing in-phase excitation of all antenna elements, and (b) 3-D view of the patch arrays positioned on the meandered waveguide. The electromagnetic power is coupled to the center patch and is distributed to the patch elements through the center line……………………………………………………………………………………..54

3.4 Schematic diagram of the complete horizontally-polarized array antenna with 450 patch antenna elements as the radiating elements……………………………………………55

3.5 Full-wave simulated normalized pattern of the beam-steering array in (a) azimuth plane, and (b) elevation plane………………………………………………………………...56

3.6 Simulated gain, directivity, and radiation efficiency of the beam-steering array over the operation frequency band…………………………....…………………………..57

4.1 (a) Diagram of a wire-bonded chip for integration of active MMIC with the rest of the system, and (b) Full-wave simulated *S*-parameters of the back-to-back wire-bonded thru-line chip showing deteriorated performance of packaging with the increase in the frequency…………………………………………………………………………..…..60

4.2 Schematic diagram of the peg and socket packaging block with the associated transitions and the bias circuitry for integration of active MMIC. The structure is composed of five main sections: a mounting block where the MMIC (peg) is inserted into the package

(socket); RF transitions from the chip to the package RF lines; low-loss cavity-backed coplanar (CBCPW) on-wafer lines; transitions from CBCPW lines to on-wafer rectangular waveguides; and on-wafer bias circuitry with incorporated broadband RF-choke………62

4.3 After insertion of the MMIC, an etched silicon block is also mounted in the socket to support the integrated MMIC in eth package……………………………………………..64

4.4 Full-wave simulated *S*-parameters of the back-to-back transition from the on-wafer CBCPW line to the microstrip line on a delay line chip. The results only include the losses associated with the package…………………………………………………………....64

4.5 Configuration of the wideband RF-choke incorporated in the chip packaging block, (a) 3-D view, and (b) top view showing implementation of the RF-choke with a series of open-ended stubs with optimized dimension each tuned at different center frequencies………66

4.6 Full-wave simulated response of the proposed RF-choke showing broadband (40-330 GHz) isolation (>10 dB) of the two ports……………………………………………………….67

4.7 (a) Schematic diagram of the package with possible misalignments (d_x , d_y) and gaps (d_z) between the on-wafer pads and those of the MMIC, (b) full-wave simulation of the effect of the gaps on the RF performance of the package, and (c) sensitivity analysis of the RF performance of the package with respect to misalignments over the entire WR-3 band…………………………………………………………………………………….68

5.1 Overview of the radar RF front-end micromachining process. 1) The meandered waveguide trench as well as chip package socket and the associated transitions are etched in the bottom silicon wafer, 2) The slots, cavity-backed trenches for the patch array, and the DC and RF lines of the chip package are realized on the top silicon wafer, 3) Top and bottom wafers are metalized and are bonded to each other using thermocompression bonding process, 4) Patch array antennas are patterned on a thin membrane layer, and 5) The membrane is attached to the bonded wafers to complete the microfabrication of the RF front-end…………………………………………………………………………………..72

5.2 Multi-step patterning and etching process of the meandered waveguide trench in a thick (1 mm) silicon wafer. (a) Low pressure chemical vapor deposition (LPCVD) silicon dioxide (SiO2) deposited and patterned as the first mask layer, (b), (c) Plasma-enhanced chemical vapor deposition (PECVD) SiO2 deposited and patterned as the second and third mask layers, (d), (e) and (f) first, second and third steps are etched in the silicon wafer using Bosch deep reactive-ion etching (DRIE) process and the corresponding mask layers are removed after each etch…………………………………………………………………..74

5.3 Gold plated bottom wafer containing the meandered trench of the waveguide structures for two side-by-side antennas. The close-up highlights microfabricated reflection cancellation posts in the meandered structure……………………………………………………………75

5.4 Thru-wafer opening etched in the bottom wafer for mounting the MMIC in the package. Multi-step waveguide to CBCPW trench as well as waveguide probe to on-wafer waveguide transitions are fabricated on the bottom wafer using the multi-step microfabrication process……………………………………………………………………75

5.5 Microfabricated top wafer with slots and the cavity-backed patch array trenches etched on both sides of the wafer, (a) top view, and (b) bottom view………………………………77

5.6 (a) Scanning Electron Microscope (SEM) of the package top wafer showing the gold plated pillars on the RF and DC pads, and (b) close up of the broad-band RF-choke and the netwrok for biasing active MMIC……………………………………………………………..78

5.7 (a) Cross-section of diced waveguide section confirming metallization of the etched waveguide trenches, and (b) Micrograph of the diced waveguide showing the quality of the gold-to-gold bonding at the bonding interface…………………………………………...79

5.8 Diagram of microfabrication steps for realization and attachment of the patch array elements to the bonded bottom and top wafers. (a) Photoresist sacrificial layer spun on a carrier glass wafer, (b) 5 μm of Parylene deposited on the wafer as the membrane layer, (c) 0.5 μm of gold evaporated and patterned on the carrier wafer to form the patch array elements, (d) photoresist sacrificial layer dissolved and removed to release the membrane layer, (e) 1 μm of adhesive spun on the sample using, and (f) membrane aligned and attached to the bonded bottom and top wafers, and the carrier wafer detached…………..81

5.9 (a) Patterned patch array on the Parylene membrane layer deposited on a glass wafer before releasing, and (b) Patterned patch arrays for the vertically-polarized antenna are patterned are transferred to the bonded wafers using low stress adhesive (Dymax 4-20418)……….82

5.10 (a) SEM of the etched trench showing (a) roughness and grassing effects at the bottom and edges of an etched waveguide trench, and (b) sidewall roughness and scalloping effect formed on a three-stepped etched waveguide……………………………………………83

5.11 (a) SEM of a corner of the etched waveguide trench showing grassing effects formed at the corners of the trench, and (b) SEM of the waveguide trench corner etched with the modified DRIE recipe……………………………………………………………………………84

5.12 SEM of the sidewall of the waveguide trench after multi-step DRIE etching showing sidewall roughnesses, and (b) sidewall of the multi-step etched waveguide trench after applying the smoothening technique……………………………………………………..86

5.13 SEM of the cross-section of a diced waveguide showing the DRIE etch profile of the deep trench. The sidewalls have a slope of about 89◦ with an undercut of approximately 2 μm……………………………………………………………………………………..86

5.14 Close-up of the micromachined frequency scanning beam-steering antenna at 240 GHz. (a) Vertically-polarized Tx/Rx set with over 1200 radiation elements and weighs only 4.4 g, and (b) Horizontally-polarized antenna set with 900 patch antenna elements……………88

5.15 Close-up of the micromachined chip package with incorporated RF-choke and the bias network for integration of active and passive MMIC, (b) bottom-view of the package before insertion of the MMIC, showing the RF pads and the associated transitions, and (c) top view of the package with an integrated through-line MMIC…………………………89

6.1 Photograph of the WR3 measurement setup…………………………………………...92

6.2 Photograph of a WR3 GSG probe. The fragile tip of the probe makes repeatable and reliable measurements challenging, specifically because of the mechanical instability after a few measurements……………………………………………………………………………92

6.3 Conceptual illustration of the proposed measurement approach showing the open-ended waveguide probes coupling the electromagnetic power to on-wafer waveguide components through proper micromachined transitions………………………………………………93

6.4 Schematic of the micromachined waveguide probe to on-wafer waveguide transition (a) 3D view of half of the structure showing the waveguide probe in contact with stepped E-plane bend transition, (b) Side view of the structure showing an alignment accuracy of 10 μm……………………………………………………………………………………..95

6.5 Diagram showing the probe opening on the top wafer for accurate alignment of the probe with the waveguide opening…………………………………………………………….….96

6.6 Full-wave simulation results of the optimized two-step transition from the WR3 waveguide probe to on-wafer WR3 waveguide. Optimized dimensions: d_1=184 μm, h_1=118 μm, d_2=109 μm, h_2=182 μm…………………………………………………………….….97

6.7 Diagram of the optimized choke design……………………………………………….98

6.8 Full-wave simulation results of the effect of the choke on the performance of the measurements……………………………………………………………………………98

6.9 Choke milled on the cross-section of waveguide probe using the EDM technique………99

6.10 Full-wave simulation results of the optimized full-band choke design for different values of gap between the probe cross section and the surface of the wafer…………………..…99

6.11 Transmission coefficient of the transition for different misalignments of the waveguide probe with the on-wafer waveguide opening……………………………………………100

6.12 Variations in transmission coefficient of the transition with respect to height variations of the micromachined steps in the DRIE process…………………………………………..101

6.13 Transmission coefficient of the transition for different displacements between the centers of the milled choke and the waveguide….………………………………………………101

6.14 WR3 waveguide probe measurement setup……………………………………………..102

6.15 Simulated and measured S-parameter of an on-wafer back-to-back transition………….102

6.16 (a) Repeated transmission coefficient measurements of a single on-wafer back-to-back transition (N=30), (b) Transmission coefficient of the back-to-back transition for repeated measurements normalized to a reference measurement………………………………...104

6.17 (a) Diagram of the proposed near-field measurement system for MMW, sub-MMW and THz on-wafer antenna characterizations, and (b) Photo of the proposed WR-3 band near-field measurement setup used for on-wafer characterization of the antenna array. Special waveguide probe with tapered tip is used for near-field measurement of the antenna under test. Another open-ended waveguide with on-wafer transition are devised to feed the waveguide port of the antenna…………………………………………………………..107

6.18 Measured normalized field intensity distribution at the center frequency over the area of the beam-steering antenna in the (a) co-polarized orientation, and (b) cross-polarized orientation with the measurements normalized to the co-polarized measurements……..110

6.19 Measured (a) field intensity, and (b) phase distribution at the center frequency over the array elements along the azimuth (lateral) direction…………………………………….111

6.20 Normalized pattern of the co-polarized beam-steering antenna in the (a) azimuth plane, and (b) elevation plane…………………………………………………………………………113

6.21 Measured normalized 3-D pattern of the co-polarized beam-steering antenna at (a) 230 GHz, (b) 237.5 GHz, and (c) 245 GHz……………………………………………………114

6.22 Measured directivity of the co-polarized antenna over the operation frequency range….114

6.23 Normalized pattern of the cross-polarized beam-steering antenna in the (a) azimuth plane, and (b) elevation plane……………………………………………………………………115

6.24 Measured directivity of the antenna over the operation frequency range……………….116

6.25 Close-up of the WR-3 pyramidal horn antenna as the reference antenna……………….118

6.26 Photo of the WR-3 band antenna far-field measurement setup for gain characterization of the WR-3 band pyramid horn antenna as the reference antenna………………………..119

6.27 Measured gain of the standard pyramidal horn antenna……………………………....119

6.28 Photo of the WR-3 band antenna near-field measurement setup for characterization of the pyramidal horn antenna fed by custom-made waveguide segment……………………..120

6.29 Normalized pattern of the pyramidal horn antenna at 260 GHz……………………..…120

6.30 Comparison between the measured and simulated gain of the co-polarized beam-steering antenna……………………………………………………………………………….121

6.31 Measured and simulated efficiency of the microfabricated co-polarized beam-steering antenna over the desired frequency band……………………………………………121

6.32 Comparison between the measured and simulated gain of the cross-polarized beam-steering antenna………………………………………………………………………123

6.33 Measured and simulated efficiency of the microfabricated cross-polarized beam-steering antenna over the desired frequency band……………………………………………123

6.34. Close-up of the package along with the RF transitions from waveguide ports of the package to the on-chip CPW ports of the packaged chip. The MMIC is packaged at the center and its *S*-parameters are measured using a non-contact on-wafer measurement technique [121]…………………………………………………………………………………125

6.35 Measured *S*-parameters of a packaged thru-line InP chip over the WR-3 frequency band. For fair evaluation of the RF performance of the package, the insertion loss of the MMIC is measured separately and is de-embedded from the measurements to represent only the performance of the package……………………………………………………………..126

6.36 Measured *S*-parameters of the broad-band RF-choke over various frequency bands showing an RF isolation of better than 10 dB with a reflection loss of less than 2 dB over the entire desired frequency range (30-330 GHz)……………………………………127

6.37 (a) Close-up of a packaged single stage amplifier, and (b) Measured I-V characteristics of the packaged MMIC, verifying successful biasing of active MMIC in the package…….128

6.38 Measured S-parameters of a packaged single stage amplifier with poor gain (loss), before and after packaging. (a) Measured gain (S21) of the amplifier showing minimal effect of the package (<1.2 dB per transition) on the performance of the MMIC, and (b) Measured reflections of the MMIC verifying minimal effects of the packaging technique………..129

LIST OF TABLES

1.1 World Health Organization (WHO) report of total road fatalities in 2015 [27]. Road traffic injuries caused an estimated 1.24 million deaths worldwide in the year 2015: that is one person is killed every 25 seconds. Driver error is the common cause of traffic injuries and fatalities, and by having one extra second of warning (by using advanced navigational sensors), the number of rear-end and head-on collisions can be reduced by 90% and 60%, respectively……………………………………………………………………………..6

1.2 Summary of the specifications of the proposed beam-steering radar……………………18

2.1 Antenna scanning range for various inter-element waveguide length and wall thicknesses………………………………………………………………………………. 31

2.2 One-dimensional array antenna parameters summary……………………………………35

5.1 Optimized DRIE Silicon Etching Recipe Parameters……………………………………85

5.2 Summary of the XeF_2 etching recipe parameters for smoothening the sidewalls of the etched trenches…………………………………………………………………………...86

6.1 Summary of the co-polarized beam-steering antenna radiation characteristics: Comparison of the measured and simulated performance ……………………………………………122

6.2 Summary of the cross-polarized beam-steering antenna radiation characteristics: Comparison of the measured and simulated performance ……………………………..124

LIST OF ABBREVIATIONS

AUT	Antenna under test
CBCPW	Cavity-backed coplanar waveguide
DRIE	Deep reactive ion etching
DUT	Device under test
GSG	Ground-signal-ground
HFSS	High frequency structural simulator
HPBW	Half power beam width
MMIC	Monolithic microwave integrated circuit
MMW	Millimeter-wave
Sub-MMW	Submillimeter-wave
S-parameter	Scattering parameters
SWaP	Size, Weight, and Power consumption
THz	Terahertz
VNA	Vector network analyzer

ABSTRACT

Motivated by the recent interest in high millimeter-wave (MMW) and sub-MMW radar sensors for applications ranging from navigation and mapping in autonomous systems to public safety and standoff detection of concealed weapons, this work presents the technology in support of a novel sub-MMW radar with minimal Size, Weight, and Power consumption (SWaP). This includes development and implementation of novel design, microfabrication, and measurement methods and techniques to develop the passive RF front-end of the radar system operating at 240 GHz. The sub-MMW radar system is designed for navigation and mapping applications in autonomous systems [3], [4]. The salient features of the proposed radar are its ultra-lightweight (less than 5 grams), compact form factor (2 cm^3), low power consumption (6.7 mW for 1 fps), and ease of scalability to higher frequencies (up to 1 THz).

This work introduces novel components and sub-systems for the RF front-end of the radar system. This includes developing high performance radar antenna systems as well as the chip packaging and integration technology with the associated transitions for realization of the radar system. In order to satisfy the requirements for high resolution and wide field of view for this imaging and navigation radar sensor, frequency scanning beam-steering antennas are developed to achieve ±25˚ of beam steering with a very narrow beam of 2.5˚ in the direction of scan. The designed array antenna has over 600 radiating elements and exhibits a radiation efficiency of over 55% over the entire scanning range and provides a gain of over 30 dBi over the entire operation

frequency range. Additionally, for polarimetry applications, two versions of the antenna with both co- and cross-polarizations are developed to allow full-polarimetry imaging at sub-MMW frequencies. This is particularly important as targets show higher cross-pol signatures at such high frequencies. Another contribution of this work is development of a novel chip packaging methodology with the associated biasing network for sub-MMW integration of active and passive MMICs in the RF front-end. The packaging method offers a compact, low-loss (less than 1 dB per transition), and wideband (the entire WR-3 band) integration solution in the sub-MMW to terahertz (THz) frequency band which can be standardized for reliable and repeatable integrations at such frequencies.

Due to the small wavelength at MMW to THz frequency band, fabrication of sub-MMW components and sub-systems requires high fabrication tolerances and accuracies, which is costly and hard to achieve with the standard machining techniques. To overcome this problem, in this work novel silicon micromachining methods are developed to enable reliable fabrication of complex structures, such as the radar RF front end, with low mass and low cost. The fabrication method allows seamless realization of the entire radar RF front-end on a single silicon block with a compact form factor and high level of integration.

Repeatable and reliable characterization of sub-MMW components and sub-systems is a very challenging task and one major contribution of this dissertation pertains to development of novel measurement techniques to enable reliable on-wafer characterization of such devices in the MMW to THz band. This includes development of a novel waveguide probe measurement technique along with specially designed probes and the associated transitions for on-wafer S-parameter measurements at sub-MMW frequencies. Additionally, a novel on-wafer near-field measurement method is also developed to allow 3-D pattern and power (gain and efficiency)

characterization of the antennas at sub-MMW frequencies. These methods are employed to perform full on-wafer characterization of the micromachined RF front-end components, including the co- and cross-polarized antennas as well as the chip packaging, where excellent agreement of designed and measured results are shown.

CHAPTER 1
INTRODUCTION

The millimeter-wave (MMW) frequency band is referred to the range of electromagnetic frequency spectrum where the wavelength is comparable to a millimeter. Strictly defined, this refers to the frequency range where the wavelength is between 10 mm to 1 mm, corresponding to frequencies from 30 to 300 GHz. The terahertz (THz) band, is the frequency range extending from 300 GHz to 3 THz (wavelength of 1 mm to 100 um), with some ambiguity on both ends of this spectrum. Different portions of these bands are also variously called sub-millimeter, far-infrared, and near-millimeter, with the electromagnetic band ranging from about 200 GHz and higher commonly referred to as sub-millimeter-wave (sub-MMW) frequencies [1]. The ambiguity in the frequency range of the MMW and sub-MMW frequency bands is mainly attributed to the overlap of techniques used in each band from different ends of the spectrum [2]. Having originated from microwave frequencies, MMW technology is based on coherent oscillators. High sub-MMW or THz frequencies, on the other hand, are based on the use of incoherent sources and later on the use of harmonics of microwave- or millimeter-wave coherent sources, but often in both cases employing optical techniques.

Sandwiched between the traditional microwave and optical frequency bands, the sub-MMW band is one of the least tapped regions of the electromagnetic spectrum, mostly due to the associated technological challenges in these bands [3]. This, in return, has preserved some unique

scientific and engineering opportunities, which have remained untouched until recently. With recent advancements in this field, sub-MMW has become an active area of research among several research groups. This in turn, has opened the door to completely new applications ranging from spectroscopy, radio astronomy, and remote sensing to security and surveillance, high-resolution imaging and detection, high data-rate communication, and biomedical applications, as further discussed in Section 1.3. The main reasons that makes the MMW and sub-MMW range so appealing for such applications lies in the inherent unique features of this frequency bands as well as some of the limitations of the adjacent frequency bands, as will be discussed in detail in the section.

1.1. Motivation

1.1.1. Unique Thermal Radiation Characteristics

One of the unique features of the MMW and sub-MMW frequencies is the fact that thermal emission lines from various lightweight molecules fall into these frequency spectrums. Figure 1.1 shows the spectral signature of an interstellar dust cloud, explaining the significance of this frequency band for astronomers, planetary, and space scientists as well as biologists and chemists for a wide range of scientific, medical and industrial applications [4]-[7].

1.1.2. Wide Unrestricted Bandwidth

Traditional Microwave and MMW technologies (up to 100 GHz) have seen significant maturity with several decades of research and development. As a result, the electromagnetic spectrums of these frequency ranges are heavily over-crowded and protected for various applications and standards by Federal Communications Commission (FCC). The sub-MMW

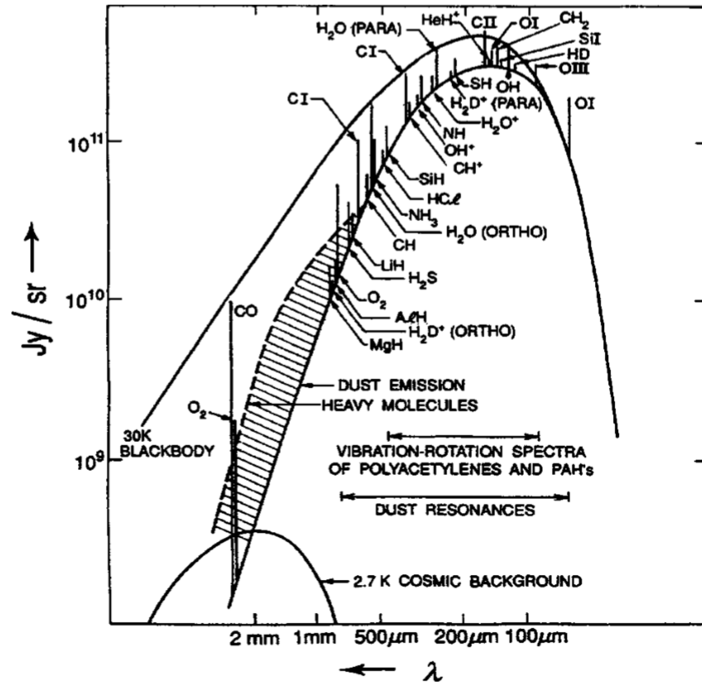

Figure 1.1. Some of the spectral content in the sub-MMW band for an interstellar cloud (Reprinted from [4]).

frequency range, on the other hand, is much less exploited and have the advantage of availability of excessive bandwidth in several atmospheric windows, as shown in Figure 1.2. The availability of abundant bandwidth enables realization of technologies ranging from ultra-fast communication links with tens of Gb/s data rates [8]-[14] to high-resolution active and passive MMW radars and radiometers [15]-[22].

1.1.3. System Miniaturization through Small Wavelength

With the increase in the frequency, the wavelength becomes smaller at sub-MMW and THz frequencies and as a result, realization of compact Radio Frequency (RF) components and systems becomes viable. This is particularly important in large antennas and arrays with narrow beams and high gains for high-resolution imaging and detection systems, where the small wavelength at sub-

MMW frequencies enables realization of electrically large but physically compact antennas and antenna systems.

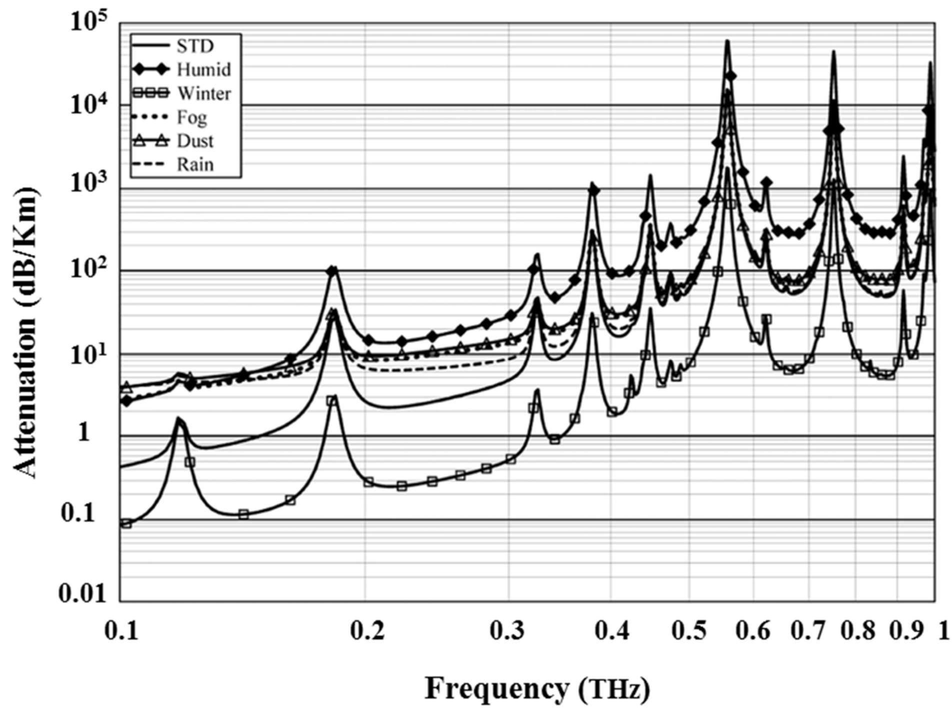

Figure 1.2. Atmospheric attenuation at sea level pressures for various different conditions of temperature, humidity, and atmospheric particulates. The graph shows the atmospheric windows with unrestricted bandwidths at high MMW and sub-MMW frequencies, suitable for applications ranging from high data-rate communications to high-resolution imaging (modified reprint from [6]).

1.1.4. Low-loss Penetration Capability

One major drawback of high-resolution infrared and optical imaging and detection sensor technologies is the fact that their performance is critically hampered under inclement weather (rain, snow, and fog), smoke, dust, and presence of ambient infrared sources. In fact, as shown in Figure 1.3, under heavy fog or smoke conditions the optical attenuation can reach 1 dB/meter, which significantly limits the detection range of such sensors [23]-[25]. This is while, MMW and sub-

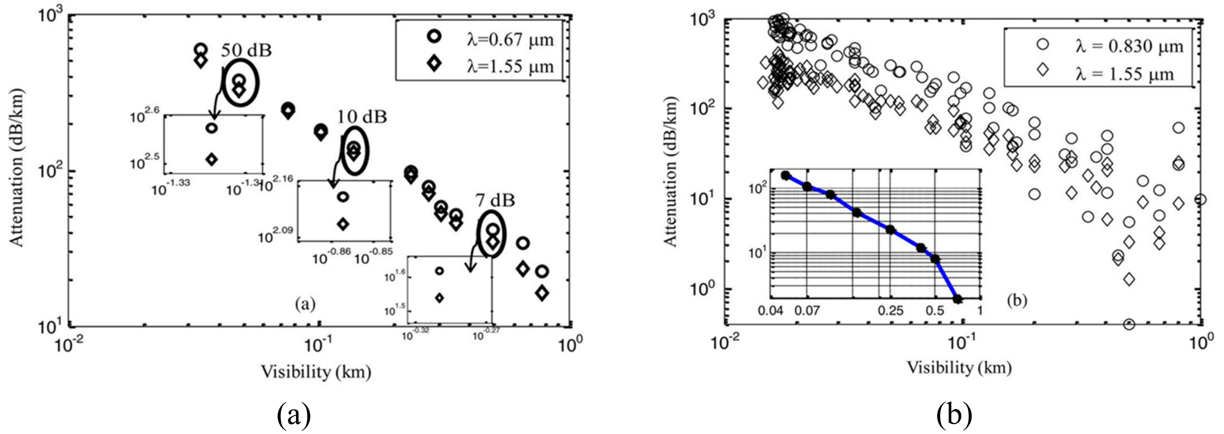

Figure 1.3. Measured attenuation versus visibility at optical frequencies under (a) fog, and (b) smoke conditions. (Reprinted from [23]).

MMW sensors are much less prone to such environmental parameters due to larger wavelengths, but the wavelength is still small enough to maintain system compactness, as desired [6], [26].

1.2. Applications

1.2.1. Autonomous Vehicle Applications

As the next frontier in the automotive industry, we are now facing a substantial change engendered by autonomous vehicles. This technology offers significant benefits to our welfare-saving lives; reducing crashes, congestion, fuel consumption, and pollution; increasing mobility for the disabled; and improving land use being some of possible instances of the benefits that this technology offers (Figure 1.4). According to the World Health Organization (WHO), in 2015 alone over 1.2 million deaths occurred worldwide with driver error being the main cause of these fatalities (Table 1.1) [27]. These numbers are expected to drop by 90% and 60%, respectively by using advanced navigational sensors in autonomous cars. However, to enable realization of

autonomous vehicles a number of challenges need to be addressed, one of which being development of advanced navigation and collision avoidance sensors.

Table 1.1. World Health Organization (WHO) report of total road fatalities in 2015 [27]. Road traffic injuries caused an estimated 1.24 million deaths worldwide in the year 2015: that is one person is killed every 25 seconds. Driver error is the common cause of traffic injuries and fatalities, and by having one extra second of warning (by using advanced navigational sensors), the number of rear-end and head-on collisions can be reduced by 90% and 60%, respectively.

Country	**Number of Fatalities**
China	261,367
India	238,562
Brazil	41,059
Indonesia	38,279
Nigeria	35,621
United States	34,064
Russia	27,025
Pakistan	25,781
Iran	24,896
Thailand	24,237
World	**1,250,000**

(a) (b) (c)

Figure 1.4. Autonomous vehicles offer significant benefits to our welfare: (a) saving lives and reducing crashes; (b) increasing mobility for the disabled people; and (c) improving land use as well as reducing congestion, fuel consumption, and pollution are some instances of the benefits of this technology.

Current autonomous automotive sensor solutions are based on fusion of sensors where a suite of sensors including lidars, radars, cameras, sonars, etc. are used to enable autonomous navigation of the vehicle (Figure 1.5). Amongst these sensors, lidars and cameras have the highest resolutions with broad field of views, however, as discussed earlier their performance is critically hampered by presence of inclement weather conditions smoke, dust, ambient infra-red sources or darkness. Another drawback of these sensors is their limitation in detection of mesh grids, wires, power lines as well as smooth and reflective surfaces, such as windows or flat metals, at oblique angles. Moreover, these sensors are often too bulky and power hungry for autonomous automotive applications. Current automotive MMW radar technologies (operating at 24 GHz or 77 GHz), on the other hand, are well capable of seeing through snow, rain, fog or other low-loss but optically opaque environments and materials. However, their main disadvantage is lack of sufficient detection resolution due to the limited size of the radar sensors. One promising technology for high-resolution imaging and collision avoidance applications is sub-MMW radar technology, where the small wavelength allows realization of compact and lightweight radar sensors with very high detection resolutions.

Figure 1.5. An overview of a state of the art self-driving car equipped with multiple different sensors for reliable navigation. The sensors are often too bulky, heavy, and power hungry, which makes them not suitable for ubiquitous autonomous applications.

1.2.2. Autonomous Micro Robotic Applications

Recent advancements in robotics, microelectronics, and MEMS technologies have enabled development of micro-robotic systems for a wide range of applications for both civilian and military purposes [28]-[32]. Figure 1.6 illustrates some of the most recent instances of such robotic platforms designed for applications such as remote sensing in complex and hazardous environments, search and rescue operations, ad-hoc sensor networks, security and surveillance, etc. For autonomous micro-robotic applications, these robotic platforms need to be equipped with a suite of sensors to reliably navigate in urban and indoor environments and to avoid potential obstacles. Similar to automotive autonomous sensors, these navigation sensors are expected to operate in adverse environmental conditions where the environment might be filled with smoke, dust, etc. Additionally, due to limited onboard space, load weight, power, and processing capability the sensors are required to have minimal Size, Weight, and Power consumption (SWaP).

As opposed to the state of the art lidars [33]-[37] and cameras, sub-MMW radars are fully capable of operating under such adverse conditions while satisfying the SWaP constrains of the

(a) (b)

Figure 1.6. Diagram of micro-robotic platforms: (a) a micro quadcopter drone, and (b) a miniature mechanical bat for autonomous micro robotic applications. The navigation sensors for such miniature robotic platforms are required to have a low size, weight and power consumption (SWaP) with all-weather functionality.

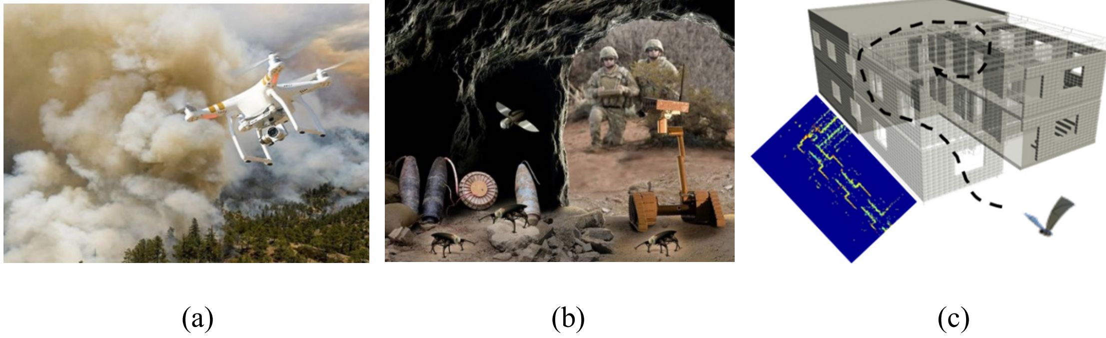

(a) (b) (c)

Figure 1.7. Applications of micro robotic systems in complex and hazardous environments for both civilian and military purposes. (a) Using micro robotic systems equipped with reliable navigation sensors can replace the role of humans in firefighting, emergency and disaster rescue, etc. (b) Autonomous robotic platforms can be used in various combat scenarios to extract the complete 3-D map of the battle field while autonomously navigating itself through adverse weather conditions (smoke, dust, etc.), and (c) autonomous micro robotics can be used in surveillance and spying applications.

micro robotic systems, and therefore present a unique solution to the need for navigation sensors for autonomous micro robotic platforms, as shown in Figure 1.7.

1.3.2. Security and Surveillance Applications

One of the main applications of the MMW radars is in the area of surveillance and perimeter security where the radar technology is used to detect hazardous concealed targets, such as weapons, in heavy-cluttered environments (Figure 1.8). Each year hundreds of mass shootings occur worldwide with thousands of victims. The statistics becomes even more tragic in the US where over 30% of such incidences take place according to the Stanford Geospatial Center. Figure 1.9 summarizes the number of victims in mass shootings occurring in the US alone from 1966 to 2015 [38]. In the US alone, over 80 mass shooting incidences occurred over the last 5 years (2010-2015) with over 280 people (excluding the shooters themselves) losing their lives and approximately 300 injuries. In order to address this global issue, several different technological solutions are proposed and utilized in the public areas such as airports, governmental buildings,

etc. Traditionally, metal detectors and X-ray systems are used for detection of such objects; however, these technologies impose health threats to human health and often are incapable of

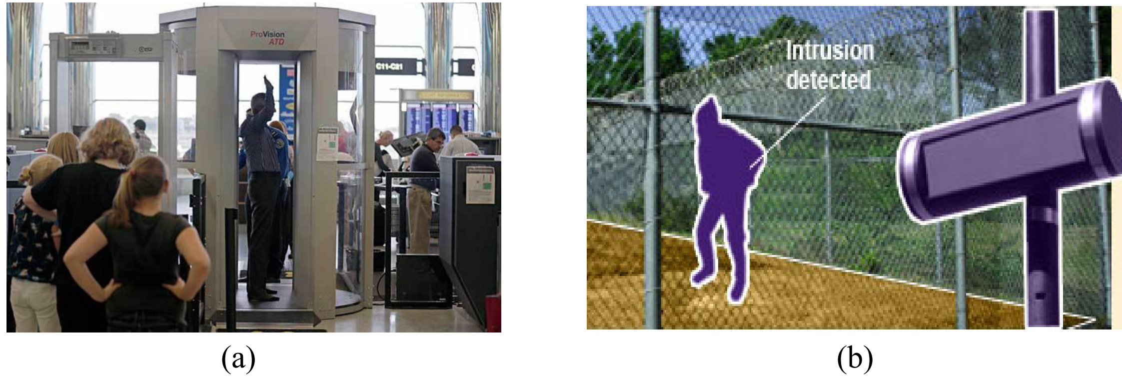

(a) (b)

Figure 1.8. Applications of MMW sensors for security and surveillance. (a) MMW imaging systems used in the public areas such as airports for detection of concealed threatening objects, e.g. weapons and explosives. (b) MMW systems used for surveillance and perimeter security in protected areas. As shown, the sensors currently used are often too bulky, heavy and expensive which makes them less desirable compared to the proposed radar technology.

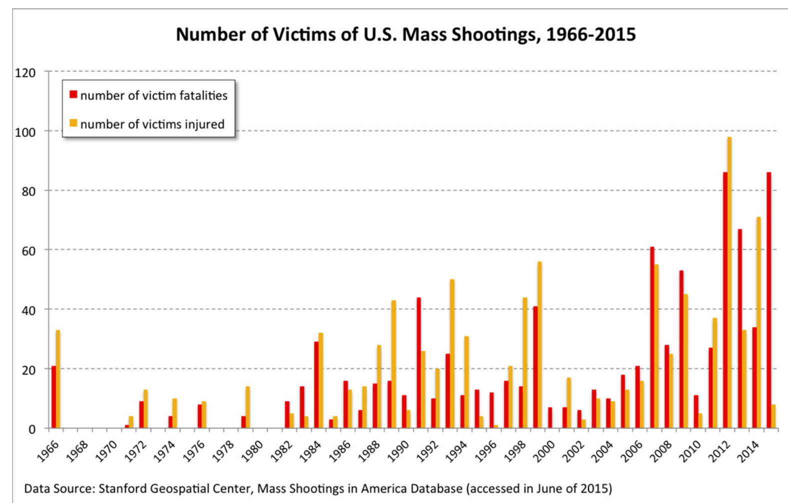

Figure 1.9. Stanford Geospatial Center report on the number of victims in the mass shootings in the US from 1966 to 2015 [38]. According to Mass Shootings in America database, an annual average of approximately 70 fatalities have occurred in the US since 2010 (2010-2015). Mass shooting is a global issue that takes hundreds of lives annually. One effective way of preventing mass shootings is to use gun detector sensors in public areas (airports, schools, universities, etc.) to identify and disarm shooters.

distinguishing harmless small personal objects from weapons. Unlike these technologies, MMW radar radiation is non-ionizing, leading to minimal health risks. Additionally, the abundance of frequency bandwidth as well as feasibility of realizing large radars in compact form factors at MMW and sub-MMW frequencies, results into achieving very high detection resolutions, and hence high quality imaging capabilities. At the same time as opposed to optical sensors (such as lidars or cameras), the wavelength at MMW frequencies is long enough to allow signal penetration through multiple layers of clothing with little or no attenuation, and hence enabling detection of concealed targets. The proposed MMW radar system presents a novel technological solution to this reliable detection of concealed weapons and other hazardous object, at fraction of the size, weight and cost of the state of the art MMW radar systems currently available in the market (such as the imaging systems used in the airport and aviation security).

1.3. History and Background

The first MMW and sub-MMW activity occurred in 1890s when Hertz, Lebedew, Lampa, and Bose independently reported generation and detection of wavelengths as short as 4 mm with spark-gap generators. But it was not until World War II (1939-1945) when first generation of radars operating at high microwave/low MMW frequencies (K-Band) were developed with the goal of better angular resolution with limited aperture size [2], [39]. The early MMW technology was based on klystrons and vacuum tubes, which were bulky, heavy, narrow-band and also suffered from short life span [40]-[42]. Despite all these limitations, however, vacuum tube radars with bulky components and antennas remained un-rival until early 1960s where several different institutions and organizations around the world focused on development of more efficient tube

sources at MMW and sub-MMW frequencies with ongoing active research on this topic until 1980s.

Throughout the 1960's and 1970's decades, several major programs were initiated with the goal of developing radars and radiometers for applications at 35, 95, 140, 220 GHz frequencies [2]. This started a quest for development of solid-state sources, as more reliable and long-living sources for such systems as opposed to conventional costly and bulky vacuum tubes and gyrotrons. With the advent of solid-state sources in this era, the MMW and sub-MMW technology continued to expand in level of effort, diversity, and technical progress. It was during this period that first commercial MMW radar applications emerged. For instance, automotive industry was one of the first adopters of MMW radar technology for Autonomous Intelligence Cruise Control (AICC) systems [43]. In 1970's companies such as RCA Corp. (took over by General Electric in 1986), Nissan Motor Company, and Telefunken developed MMW radars at various low MMW frequencies (18, 24, 34, 50 GHz). The first generation of these radars were based on metal or plastic waveguide blocks with integrated solid state sources which made them bulky, heavy, and costly to fabricate. The radar antennas were also based on bulky horn or parabolic antennas with a single beam, which also suffered from limited functionality, such as beam steering or high resolution.

Throughout 1970's and 1980's the MMW radar technology continuously improved and by early 1990's more advanced generations of radars at higher MMW frequencies emerged from several companies all around the world. Some of these radars were operating at frequencies as high as 77 GHz or even 94 GHz. By the time, solid-state technology had also matured well into monolithic microwave integrated circuit (MMIC) technology, which in turn enabled realization of cheaper, more reliable, and easier to integrate sources for the radars. The radar antennas, had also

witnessed some improvements during this period: with the increase in the operation frequency of the radars, the size of the antennas was reduced which enabled combining multiple antennas into a single multi-beam radar module for a wider field of view and higher resolutions by using beamforming techniques. However, the type of antennas used in the radars remained unchanged with bulky and hard to integrate three dimensional lens, horn, cassegrain or parabolic antennas being the main types of antennas used in these systems.

Motivated to overcome the problems associated with bulkiness and integration of automotive radar antennas, more and more focus was made on planar antennas in late 1990's and 2000's. By this time, with the advent of low-cost MMIC technology based on silicon (Si), silicon germanium (SiGe), and gallium arsenide (GaAs), radar manufacturers focused on planar antenna structures compatible with cost-efficient fabrication methods for 77 GHz radars, as shown in Figure 1.10. The most common type of these planar antennas is based on microstrip. Some examples of these antenna elements include patches or open-ended stubs as the radiators, which are arranged in series or parallel configuration to form an array antenna [44]-[47]. Another common type of planar antennas is based on dielectric guides. This includes travelling antennas with periodic perturbations where portion of the power is radiated per each element of the array. An alternative class of MMW radars are also realized by combining the planar antennas with horn or lens antennas with the goal of achieving higher gains or finer beamwidths [48], [49].

The main advantages of the aforementioned planar antennas are their compatibility with low-cost and mass-producible fabrication methods, ease of integration with MMICs in the radar front-end, and relatively compact form-factor for ease of packaging. However, one major drawback of these antennas is that they suffer from high dielectric losses associated with the substrate, resulting in low antenna gains and efficiencies. This becomes specifically limiting at

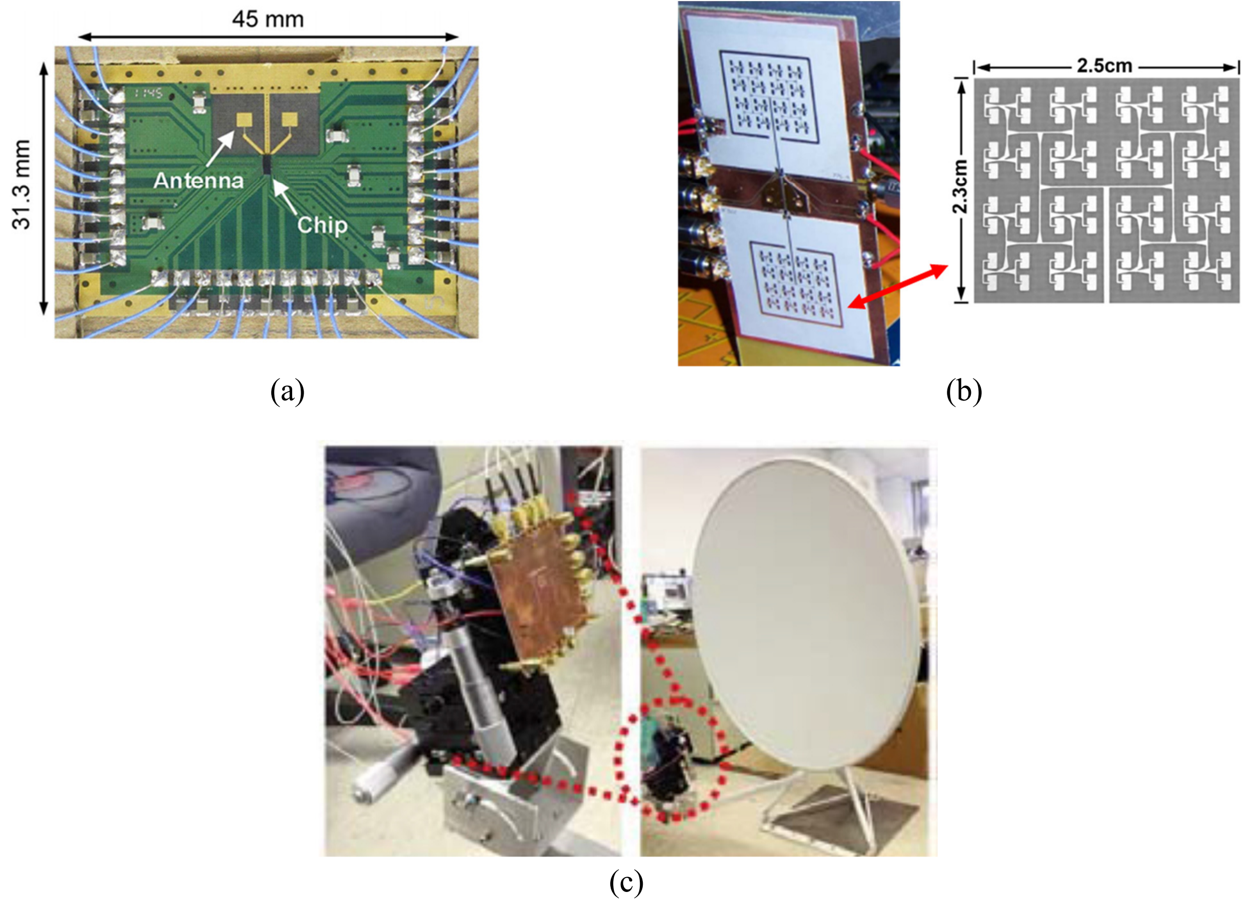

(a)

(b)

(c)

Figure 1.10. Examples of MMW systems, (a) a 60 GHz CMOS Doppler radar system with simple patch antennas as the radiators [46], (b) an integrated 77-GHz FMCW CMOS radar with patch array antennas [47], and (c) combination of planar and dish antenna implementation at 94 GHz radar system [49]. Even though, traditional microwave and MMW radar technologies (up to 100 GHz) have well maturated, extension of current technologies to higher MMW and sub-MMW frequencies is very challenging. Some of the challenges pertain to integration of active and passive modules, low antenna efficiencies and gains, complex and costly fabrication requirements, as well as challenges with characterization of these systems at such high frequencies.

higher MMW and sub-MMW frequencies as the losses associated with the substrate becomes more significant. Additionally, high substrate losses also limit the effective length of the antenna and hence results into wider antenna beamwidths and lower radar angular resolutions.

To address the challenges associated with the resolution and bulkiness of MMW radars, sub-MMW radars have gained considerable attention over the last decade for applications ranging

from navigation and mapping in autonomous systems to imaging for surveillance and security [50]-[55]. The key advantage of radars operating at high MMW and sub-MMW frequencies is that the short wavelength at this frequency bands allows reduction of the size and mass of such sensors to fraction of that of MMW radars. Additionally, the short wavelength enables realization of electrically large but physically compact radar antennas with very narrow beams. This combined with the abundance of bandwidth at this frequency bands enables realization of radars with centimeter-scale angular and range resolutions.

In general, there are two main approaches in development of such systems. The first approach is based on realization of all radar components in a waveguide system. This is mainly due to the superior loss performance of waveguides compared to other types of transmission lines at high MMW and sub-MMW frequencies. In this approach, all active and passive devices and components are packaged in machined waveguide blocks and are connected to each other using standard waveguide-to-waveguide flange connectors [56]-[61]. Some examples of such systems based on horn, reflector or lens antennas, as shown in Figure 1.11. Although this approach offers robust and reliable integration of radar systems at sub-MMW frequencies, it suffers from high fabrication machining costs of waveguide blocks and antennas. Additionally, these systems are bulky and heavy, and limited to mechanical scanning due to the complexity of the radar RF front-end. In the second approach, the entire radar circuitry is realized on a single chip, which is mounted to a simple lens antenna as the radiator [62]-[64] (Figure 1.12). While this method offers a simple, reliable, and low-cost solution, it is mostly suitable for short-range applications due to the low antenna radiation efficiencies and wide beamwidth. Moreover, similar to the first approach it suffers from simple antenna functionality.

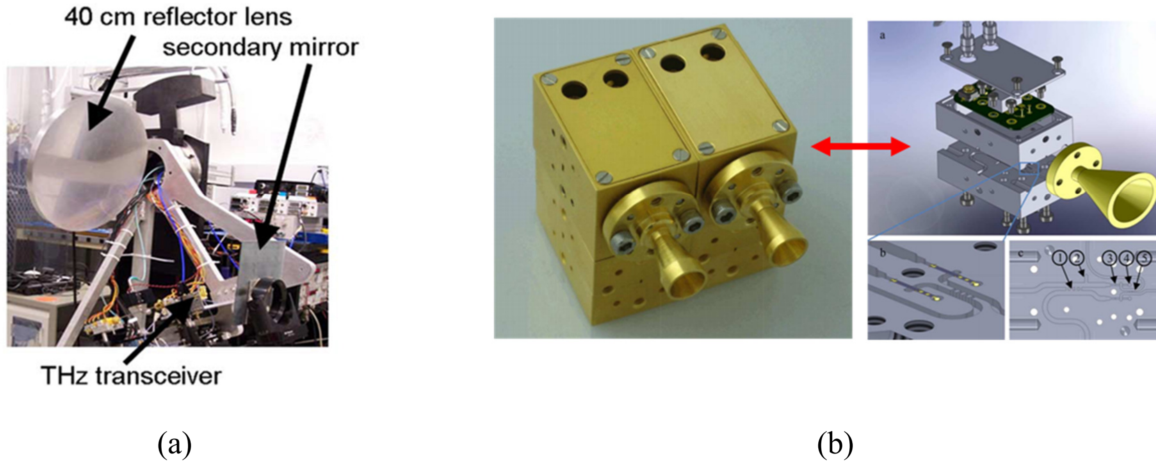

(a) (b)

Figure 1.11. (a) Photograph of a machined 600 GHz radar imager with reflector lens and mirrors as the radiators [15], and (b) an integrated FMCW radar transceiver module (Left) at 230 GHz with simple horn antennas as radiators (The antenna separation is 21 mm) [60]. The radar modules are machined and assembled accordingly, as shown in the CAD diagram (Right). Although this approach offers robust and reliable integration of radar systems at sub-MMW frequencies, it suffers from high fabrication machining costs of waveguide blocks and antennas. Additionally, these systems are bulky and heavy, and limited to mechanical scanning due to the complexity of the radar RF front-end.

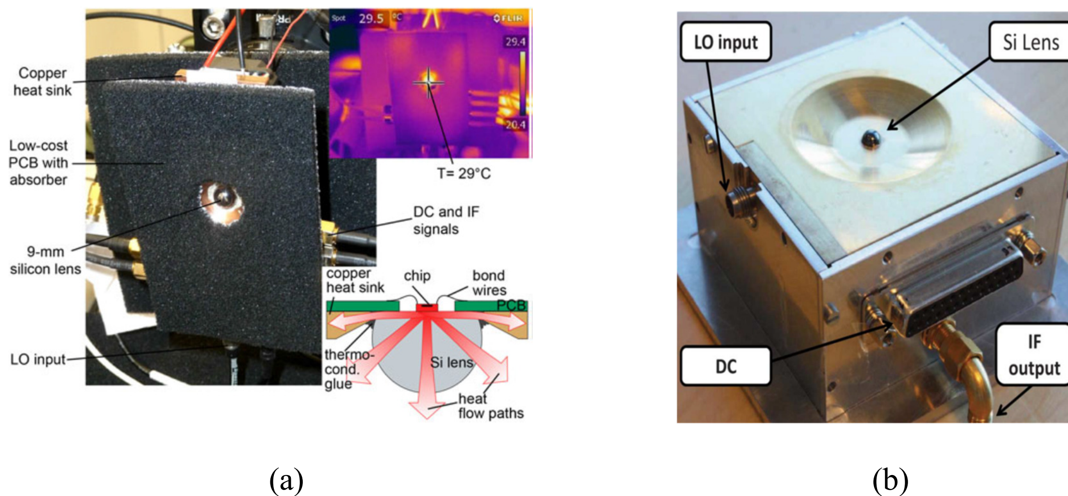

(a) (b)

Figure 1.12. (a) Lens-packaged radar transceiver module at 210-270 GHz [63]. The radar chip is mounted on the backside of a hyperhemispherical 9-mm lens made of high-resistivity silicon with the primary on-chip feed antenna aligned with the lens center. (b) Packaged MMIC-based receiver module at 220-GHz [62] with silicon lens antenna. While the lens packaging offers a simple, reliable, and low-cost solution, it is mostly suitable for short-range applications due to the low antenna radiation efficiencies and wide beamwidth. Moreover, it suffers from limited antenna functionality (i.e. antenna low gain, limited field of view, etc.)

1.4. Proposed sub-MMW Radar Technology

Motivated by the aforementioned advantages of sub-MMW radars and driven to overcome the challenges associated with size, weight, cost, functionality, loss, and integration of current state-of-the-art MMW and sub-MMW radar technologies, a novel, ultra-lightweight, beam-scanning FMCW sub-MMW radar architecture is proposed in this work. The salient features of the proposed radar are its ultra-lightweight (less than 5 grams), compact form factor (2 cm^3), low power consumption (6.7 mW for 1 fps), and ease of scalability to higher sub-MMW frequencies (up to 1 THz) [65]. In order to satisfy the requirements for high resolution and wide field of view for this imaging and navigation sensor, electronic beam-steering antennas are devised to achieve 50˚ (±25˚) of beam steering with angular resolution of 2˚ in the direction of scan [66]-[68]. Additionally, for polarimetry applications, two versions of the antenna with both co- and cross-polarizations are developed to allow full-polarimetry imaging at sub-MMW frequencies [69]. This is particularly important as targets show higher cross-pol signatures at such high frequencies. With 15 GHz of bandwidth at the center operation frequency of 237.5 GHz, the radar has a range resolution of 37.5 cm and an alias-free range of 400 m. The specifications of the radar are listed in Table 1.2 [70].

The radar architecture is designed to be compatible with silicon micromachining technology for repeatable, reliable, and cost-efficient fabrications with high accuracies [71], [72]. This combined with the short wavelength at high MMW and sub-MMW frequencies allows realization of a waveguide-based radar system on a single silicon block for minimal size and weight. Additionally, the waveguide-based radar architecture significantly improves the radar power efficiency by eliminating any lossy dielectric substrates and minimizing the losses associated with the lines. This in turn allows implementation of electrically large radar antennas

Table 1.2. Summary of the specifications of the proposed beam-steering radar

Micromachined FMCW Radar	
Operating Frequency	230 GHz-245 GHz
Weight	5 grams
Volume	2 cm^3
Wavelength	1.2 mm
Peak Tx Power	5 dBm
Rx Sensitivity with 5dB SNR	-135 dBm
Beamwidth	Az: 2° El: 8°
Antenna max directivity	32 dB
Waveform	Stepped FMCW
Frame update	33 ms
Field of view	±25°
Alias-free range	400 m
Range resolution	37.5 cm
Polarization	V and H

with high gains and angular resolutions, and also boosts the radar detection range. The schematic diagram of the radar is shown in Figure 1.13. The entire radar passive RF front-end is micromachined in a single silicon block with a size that is primarily defined by the size of the transmit and receive radar antennas. The FMCW transmit source chain, downconverting module, and the IF processor are implemented on chip using CMOS and InP technologies and are integrated into the radar using a novel chip packaging method, as shown in the block diagram of the radar in Figure 1.14 [73].

For such a radar system, the antennas are the most complex components with imposing constraints on size, weight, field of view, resolution, and power efficiency. To satisfy the requirements for high resolution and wide field of view for the radar, an electronic frequency-scanning beam-steering antenna based on a hybrid-coupled patch array travelling-wave structure is devised. The travelling-wave structure is based on micromachined hollow waveguide design for

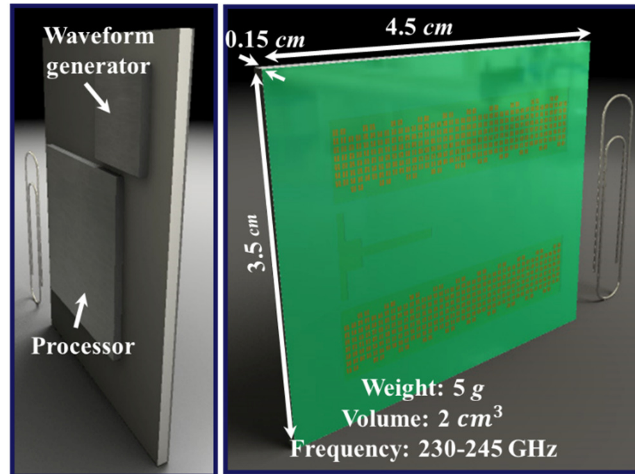

Figure 1.13. Schematic diagram of the proposed monolithic beam-steering radar system. The radar system is designed to be compatible with silicon micromachining technology for minimal size, weight, and power consumption (SWaP).

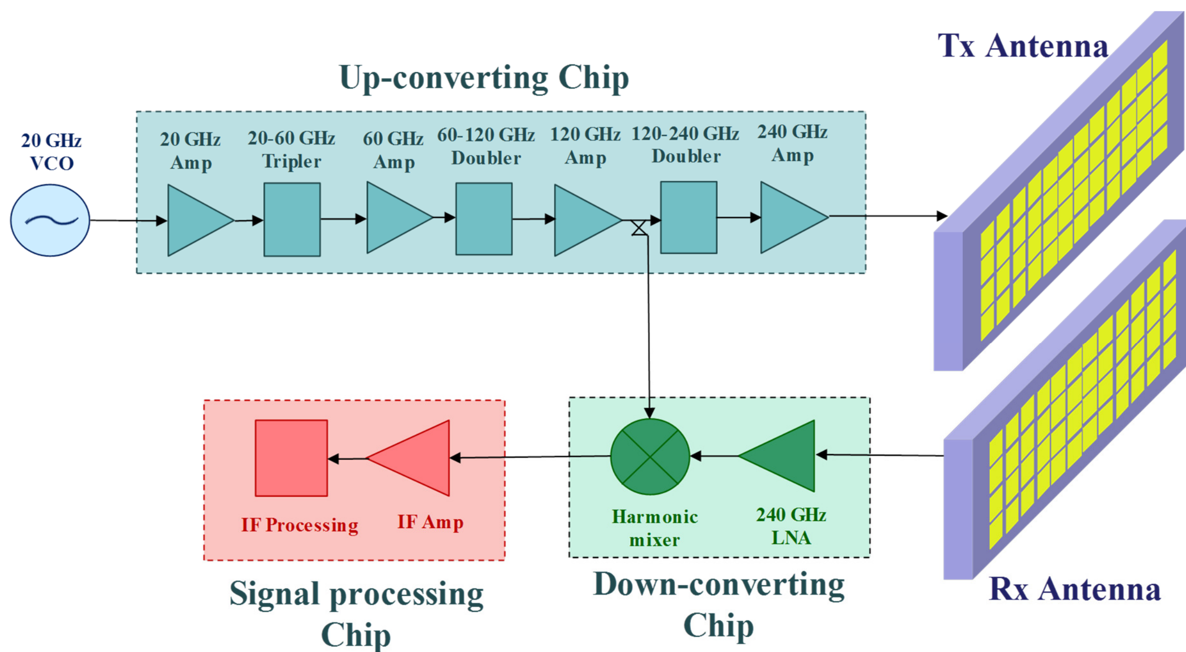

Figure 1.14. Simplified block diagram of the proposed micromachined frequency scanning beam-steering radar system operating at 230-245 GHz.

optimal loss performance, enabling realization of optimum antenna efficiency and radar angular resolution. The range resolution is also achieved using standard FMCW technique with a stepped

chirped signal waveform. Additionally, two versions of the antenna are designed with both co- and cross-polarizations to enable full-polarimetric radar capability on a single platform.

In order to package the active MMIC modules in the radar RF front-end, a packaging block compatible with silicon micromachining is devised. The package is composed of a mounting block, RF transitions from the chip to the package RF lines, and on-wafer bias circuitry with incorporated broadband RF-choke [74], [75]. The RF transition is based on a broadband planar design that is devised to transition from the on-chip RF pads to the on-wafer low-loss cavity-backed coplanar waveguide (CBCPW) lines. Additionally, in order to connect the CBCPW line with the packaged MMICs to the waveguide port of the transceiver antennas, a broadband multi-step transition compatible with silicon micromachining technology is developed [76]. This completes the signal chain from the active modulus to the antennas.

1.5. Overview of the Dissertation

This dissertation presents the development details of a micromachined sub-MMW radar technology for imaging and autonomous navigation applications. This includes the design details of the radar RF front-end consisting of the transmit and receive antennas, MMIC packaging blocks and the associated transitions in the front-end; development of novel silicon micromachining techniques for microfabrication of the radar front-end as well as other MMW and THz components; and devising novel measurement techniques for on-wafer characterizations at sub-MMW frequencies.

In Chapter 2, the design details of a novel frequency scanning antenna architecture for the radar antennas is presented [68]. The proposed antenna is a travelling-wave antenna, with a meandered rectangular waveguide structure as the propagating medium. The array is designed to

generate a very narrow beamwidth (~2˚) at the boresight of the antenna with ±25˚ of beam steering capability as the frequency sweeps from 230 to 245 GHz. Additionally, in order to confine the beamwidth of the antenna along the elevation plane, a second set of array based on a slot-coupled cavity-backed patch array design is employed which reduces the elevation beamwidth to 10˚ or less. The proposed vertically polarized array configuration provides a gain of over 30 dBi and exhibits a radiation efficiency of over 55% over the entire desired frequency range. A prototype of the antenna with over 600 array elements is fabricated using silicon micromachining and is characterized using a WR-3 (220-325 GHz) near-field measurement setup. The microfabrication process and the characterization results of the antenna are also briefly discussed in this chapter.

In order to enable polarimetry imaging using the micromachined radar, a cross-polarized version of the beam-steering antenna is developed and its design details are presented in Chapter 3. Polarimetric imaging is particularly important at high MMW and sub-MMW frequencies as targets show higher cross-pol signatures at such high frequencies. Similar to the vertically polarized antenna, the antenna concept is based on a travelling-wave structure composed of slot-coupled cavity-backed patch antenna elements. The array generates a very narrow beam (~2.5˚) with ±25˚ of steering capability. The horizontally polarized antenna is designed to share the same fabrication process as the horizontally polarized antenna to enable realization of both antennas on a single platform. A prototype of the antenna is fabricated and characterized at WR-3 band and its measurement results are presented where a minimum gain of 26 dBi, and beamwidths of less than 3˚ and 10˚ in azimuth and elevation planes, respectively, are reported.

Chapter 4 presents the design, fabrication and evaluation of a novel packaging method for integration of active MMIC at MMW and sub-MMW frequencies. This packaging approach is intended for integration of active MMIC chips in the radar RF front-end. The concept is based on

a peg and socket structure composed of RF transitions and biasing circuitry, which enables reliable integration of MMIC with waveguide-based components over a wide bandwidth. The RF transition consist of a broadband planar transition to a CBCPW line and a multi-step micromachined transition to the waveguide antennas. The design of the transition is performed to be compatible with other radar components. A prototype of the package is fabricated using silicon micromachining technology at WR-3 band and its performance is evaluated where a low-loss integration is achieved over the entire frequency band.

In Chapter 5, the details of the microfabrication process of the RF front-end of the sub-MMW radar is discussed. The microfabrication of the radar front-end is performed using three different layers. The first layer contains the trenches for the meandered waveguide structure of the phased array antenna as well as the multi-step transitions to the chip packaging block. All the trenches and steps are micro machined on a thick silicon wafer using a Deep Reactive Ion Etching (DRIE) process. The second layer provides the top wall of the waveguide and consists of the antenna slots, CBCPW lines, antenna cavity-backed trenches and slots, all of which are realized on a second silicon wafer, which is bonded to the first layer. Finally, the third layer consists of a released membrane layer with the patch array elements patterned on it that is next aligned and attached to the bonded wafers to complete the radar RF front-end fabrication. The fabrication of the radar involves several microfabrication procedures that are all optimized to enable reliable and repeatable fabrication of the radar front-end. Multi-step patterning and mask deposition, silicon multi-step DRIE, metallization and gold-to-gold thermos-compression bonding, membrane deposition and release, wafers top and bottom alignment and attachment, chemical processing and plasma treatment, etc. are some examples of such procedures used in development of the fabrication process.

Chapter 6 presents novel measurement methods devised for characterization of the micromachined components in MMW to THz frequency band. This includes development a non-contact on-wafer S-parameter measurement method along with specially designed probes and on-wafer transitions to enable characterization of waveguide based components and systems. This method offers a low-loss, repeatable, and low-cost measurement approach that is successfully used to characterize on-wafer waveguides, transitions, chip packaging blocks, etc. as well as to effectively feed the waveguide port of the antennas in the near-field measurement technique discussed next [76]. In order to enable characterization of the beam-steering antennas, a measurement system for on-wafer characterization of antennas operating in MMW to sub-MMW bands is proposed and implemented. Most existing antenna measurement systems at these frequencies require complex custom-made structures, which are costly and hard to set up. To address this problem a simple and yet effective near-field antenna measurement setup is used to characterize the three-dimensional pattern of the antenna [77]. Moreover, a comparative near-field measurement technique is also developed to characterize the absolute gain and efficiency of antennas at sub-MMW frequencies. The near-field method is used to successfully characterize the vertically- and horizontally- polarized antennas where a measured scan capability of over 48˚, a gain of better than 30 dBi, and radiation efficiency of better than 55% over the entire scanning range is reported.

The thesis concludes with a summary of its contributions and future work on this research topic in Chapter 7.

CHAPTER 2
CO-POLARIZED BEAM STEERING RADAR ANTENNA DESIGN

This chapter presents the design details of a novel beam steering antenna for the radar system. The antenna is designed to provide a wide field of view with very narrow beam widths for high detection resolutions. For high resolution applications with wide field of view, beam steering antennas can be realized either mechanically or electronically. The mechanical approach is bulky and susceptible to mechanical failure. Additionally, mechanical scanning systems are often complex and costly to implement and slow for most applications [78], [79]. Electronic beam steering is achieved using phased array antennas wherein a phase shifting mechanism is incorporated in the array elements. Conventionally, this is achieved using either phase shifters or frequency scanning using travelling wave structures where the inter-element spacing provides the required phase shift in the array. One main disadvantage of the phase shifters is that at high MMW and sub-MMW frequencies they are rather lossy and hard to implement and at high frequencies are not available [80], [81]. Most radars require narrow beamwidth and this will in turn need a large number of array elements. Beam steering of such arrays electronically is not only limited by the requirement of large number of lossy phase shifters but also losses associated with power distribution to each element. Considering these limitations, a traveling-wave frequency scanning

approach is the simplest method of beam steering if enough bandwidth is available for the radar operation.

In a traveling-wave frequency scanning antenna array, scanning is achieved as a result of the frequency dependence of the complex propagation constant of the wave propagating along the transmission line feeding the radiating elements. To minimize power loss, a waveguide as the transmission line is used. Elements are fed in series with equal lengthened waveguide segments providing the desired progressive phase difference among the array elements. At the center frequency, the delays are designed to keep all the elements in phase, generating a beam in the broadside direction. As the frequency sweeps, the phase shift between the adjacent elements changes, resulting in a steered beam. Generally, there are two basic approaches in implementing travelling-wave antennas: 1) using dielectric materials which result in slow wave radiation [82], or 2) utilizing hollow structures which result in fast wave radiation [83]. In the former approach, where dielectric based transmission lines are used as the propagating medium, excessive dielectric loss becomes a major problem at higher MMW frequency ranges. In order to suppress surface waves in this approach, a very thin substrate is required which is hard to implement given the short wavelength at sub-MMW frequencies [84]. Construction of scanning arrays based on hollow waveguide structures is convenient since they provide enough bandwidth, do not incorporate dielectric materials and the associated losses, and yet present high power handling capabilities. Another advantage of the hollow waveguides is their light weight which makes them attractive in fabrication of large arrays, such as the one presented in this work.

In this work a 2.5-D micromachined structure is devised to implement frequency scanned beam-steering array antenna over a meandered WR-3 waveguides. The array is designed to provide 50˚, i.e. ±25˚, of beam steering around the boresight of the antenna as the frequency sweeps from

230 to 245 GHz. The array generates a very narrow beamwidth of less than 2.5˚ for all scan angles in the azimuth direction. To confine the beam in the elevation direction series fed cavity-backed patch arrays excited by waveguide slots are designed. The half-power beamwidth (HPBW) of the patch array is about 10˚. The proposed array configuration provides a gain of over 30 dBi and exhibits a radiation efficiency of over 55% over the entire desired frequency range. The microfabrication of the antenna is carried out using a silicon micromachining technique and the microfabrication process along with the characterization methods and results are presented in Chapters 5 and 6, respectively.

This chapter is organized as follows. In Section 2.1, an overview of the array antenna configuration together with its beam-steering requirements is presented. Section 2.2 presents the design principles of the one-dimensional beam-steering antenna array where waveguide dimensions, inter-element spacing, number of array elements, and waveguide segment adjustments are discussed. The design steps of the two-dimensional array are discussed in Section 2.3 and finally in Section 2.4, the simulation results of the entire antenna array are presented. Details of the fabrication and measurement methods and the results are discussed in Chapters 5 and 6, respectively.

2.1. Antenna Configuration Overview

A waveguide-based travelling-wave structure is shown in Figure 2.1 (a) in which the provision of slot cuts along the broad wall of the waveguide as the radiating elements provides radiation along boresight of the antenna. The successive slots are to be less than half a wavelength apart to avoid generation of grating lobes as the beam is scanned. The frequency scanning antenna to provide large scanning angles to cover ±25˚ around the broadside direction. Since rectangular

waveguide is a fast wave structure and its propagation constant is smaller than that of the free space (λ_0), the phase shift between radiating elements is calculated as:

$$\varphi = \beta l < kl \xrightarrow{l<\frac{\lambda_0}{2}} \varphi < k\frac{\lambda_0}{2} \rightarrow \varphi < \pi \tag{2.1}$$

where β is the propagation constant of TE_{10} mode in the waveguide and l is the distance between array elements. To achieve broadside radiation, it is required that the phase shift between elements is $2n\pi$ which is not feasible with this configuration. To resolve this problem, slots can be positioned with spacing larger than half a wavelength and the grating lobes can be suppressed using spatial filters. Another approach is to have longitudinal or diagonal slots and take advantage of the phase reversal phenomenon. However, these methods are not suitable for frequency scanning applications since with a limited bandwidth, none of them can provide a sufficient amount of phase shift between slots along the waveguide to generate large scanning angles. For a linear and uniformly excited array, the array factor is given by

$$AF = \frac{\sin(N\psi/2)}{\sin(\psi/2)} \tag{2.2}$$

where, $\psi=kd\sin(\theta)+\varphi$, k is the wavenumber, d is the spacing between array elements and, φ is the phase shift between adjacent elements given by $\varphi=\beta d$. The maximum achievable scanning angle is then independent of the spacing between slots and can be obtained from

$$\theta = \sin^{-1}\left[\lambda_1\left(\frac{1}{\lambda_{g0}} - \frac{1}{\lambda_{g1}}\right)\right] \tag{2.3}$$

where, λ_{g0} and λ_{g1} are guide wavelengths at the center and maximum frequencies. At WR-3 band, considering the dimensions of WR-3 standard waveguide, W = 864 μm and H = 432 μm, we need to provide approximately 130 GHz bandwidth around 230 GHz (185 ~ 315 GHz) to achieve ±25°

scanning angle around an off-broadside angle of 43° if we were to use a straight section of the waveguide.

One way to achieve broadside radiation and wide scan angle without the need for a large bandwidth is to meander the waveguide structure. This results in an increased phase shift between the adjacent elements while maintaining a small physical spacing between them to avoid generation of grating lobes. One such structure is shown in Figure 2.1 (b). The spacing between

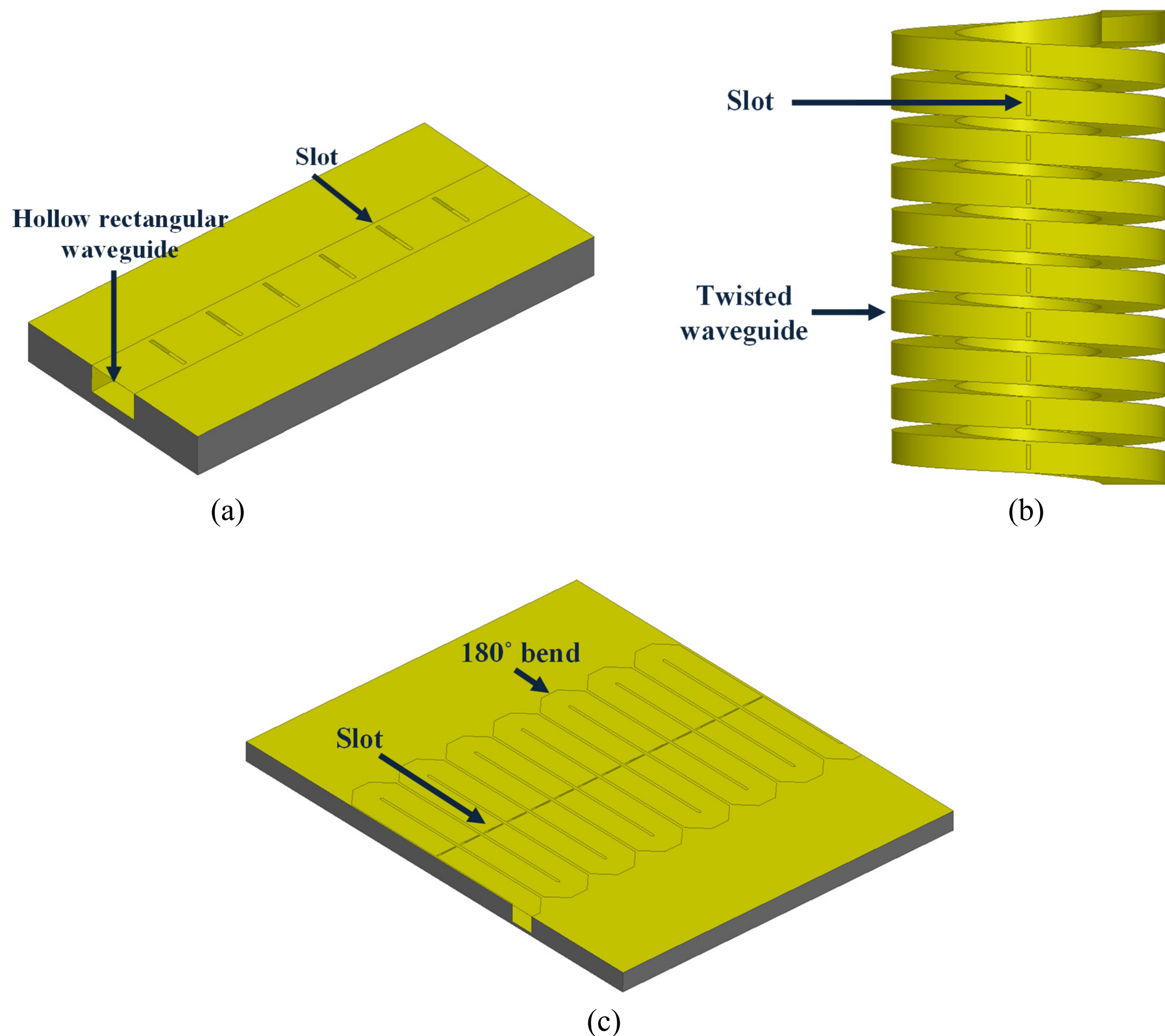

Figure 2.1. Configuration of a travelling wave antenna consisting of (a) a straight segment of a hollow rectangular waveguide with radiating slots placed along its broad wall, (b) a twisted waveguide structure with cuts along the wall of the waveguide, and (c) a meandered planar waveguide structure with radiating slots placed along its wall.

adjacent slots is approximately the width of the waveguide while the circumference of one turn of the helix is the delay segment between the elements. However, this structure is bulky, heavy and difficult to fabricate at sub-MMW frequencies. Therefore, a planar meander waveguide is considered instead. Figure 2.1 (c) illustrates a section of the proposed planar design where the waveguide structure is meandered in the H-plane and the slots are placed on broad wall of the waveguide. The planar configuration of the meandered waveguide is conducive for microfabrication of the structure using standard silicon microfabrication techniques. The choice of the H-plane versus E-plane meandered waveguide structure is partly based on the fabrication limitation which allows easier etching of the height of the waveguide compared to the larger width of the waveguide. Other features related to the design and fabrication of the radiating elements is discussed in the next section.

2.2. One-Dimensional Antenna Array Design

The detailed design of the proposed planar travelling-wave frequency scanned array is presented in this section. The design includes determination of the micromachined waveguide dimensions, the length of the meandered lines, parameters of the H-plane bend, and selecting the

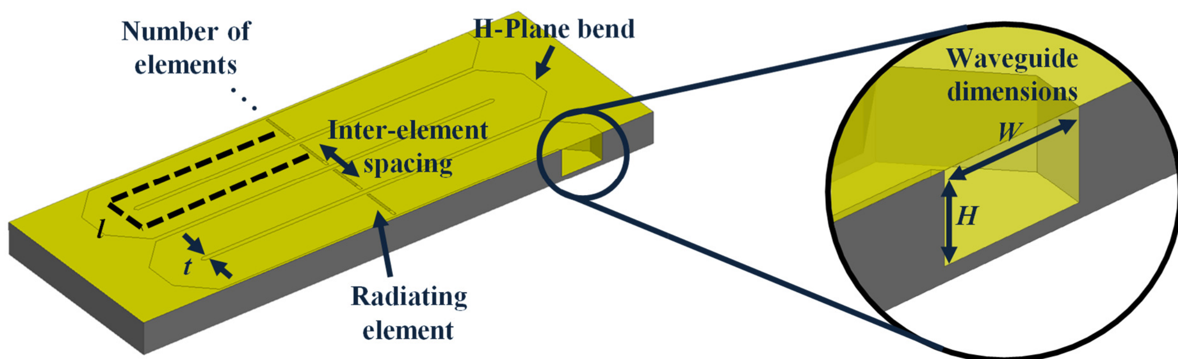

Figure 2.2. Configuration of the one-dimensional beam-steering array antenna, highlighting various design parameters in the array.

number of radiating elements in the array as identified in Figure 2.2. The design details of the slots and radiating elements in the array are described in the next section.

2.2.1. Optimum H-plane Bend Design

The bends need to be designed for minimum reflection. This can be performed by optimizing the shape of the bends using a full-wave simulator (Ansoft HFSS). Simulations results show that a diagonal cut around the edges provides a better transmission over the desired bandwidth than a curved turn as shown in Figure 2.3 (c). The optimized bend has a return loss of over 30 dB over the entire range of the frequency band.

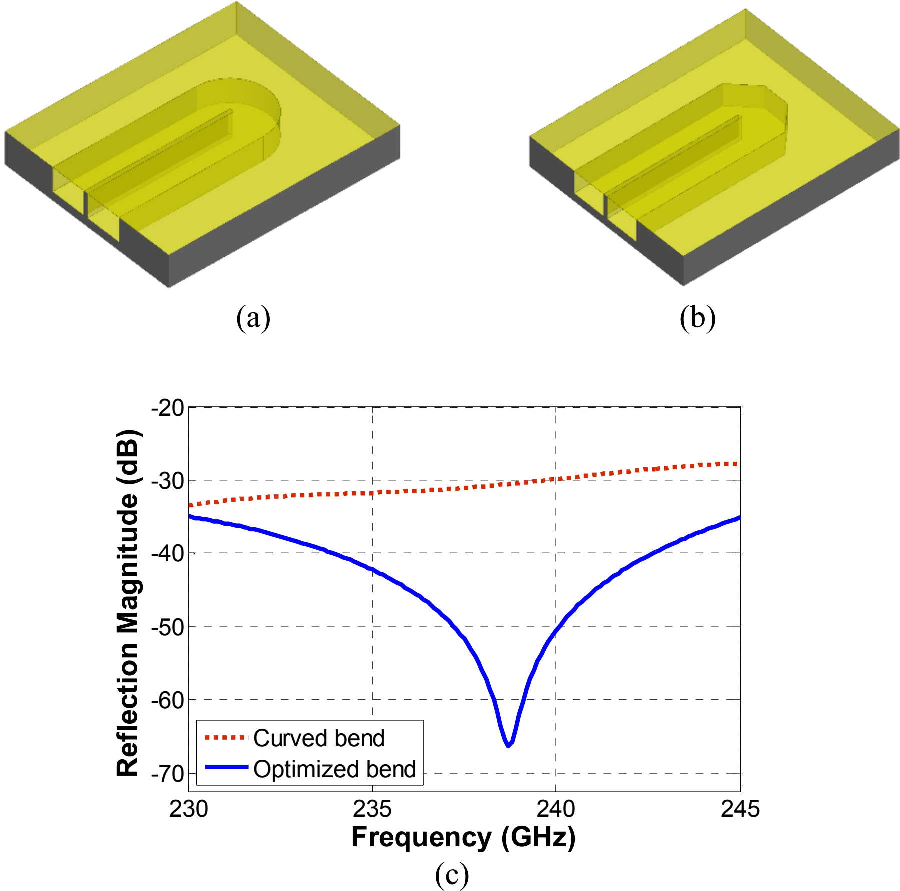

Figure 2.3. Diagram of the (a) curved bend, (b) optimized bend, and (c) full-wave simulated reflection magnitude from the bends.

2.2.2. Inter-Element Waveguide Segment Length

As discussed earlier, the array antenna is designed to achieve a broadside radiation with the beam pointing at the boresight of the antenna at the center frequency of 237.5 GHz. The waveguide segment length between the consecutive elements, l, is designed to generate $2n\pi$ phase shift between the adjacent elements at the center frequency. This requires l to be a modulus of the guided wavelength of the wave at the center frequency, λ_{g0}. However, since the direction of propagation of the field is in the opposite direction after the H-bend, the current distribution on the broad wall of waveguide should be reversed after a turn to excite in-phase electric field over the slots as shown in Figure 2.4. Therefore, the length between the consecutive slots must be adjusted by adding a $\lambda_{g0}/2$ segment to ensure that the equivalent magnetic currents on the slots are in phase at the center frequency.

In addition, the valued l must be chosen in such a way as to provide sufficient beam steering range as the frequency is swept from 230 to 245 GHz. This is feasible by choosing a sufficiently large l that provides the required phase shift while satisfying the $\beta l = 2n\pi + \pi/2$ condition at the center frequency of 237.5 GHz. Table 2.1 shows the range of scanning angle with 15 GHz bandwidth (230 ~ 245 GHz) around the boresight for different values of wall thicknesses and l values. As mentioned earlier, the meandered waveguide trenches are covered by a metalized silicon wafer and the metallic contact is established by gold-to-gold thermos-compression

Table 2.1. Antenna scanning range for various inter-element waveguide length and wall thicknesses

Inter-element waveguide length	Wall thickness (μm)	Scanning range (˚)
$4.5\lambda_{guided}$	100	-27.9 ~ +25.0
	200	-25.1 ~ +22.6
$5.5\lambda_{guided}$	100	-34.1 ~ +30.5
	200	-30.5 ~ +27.4

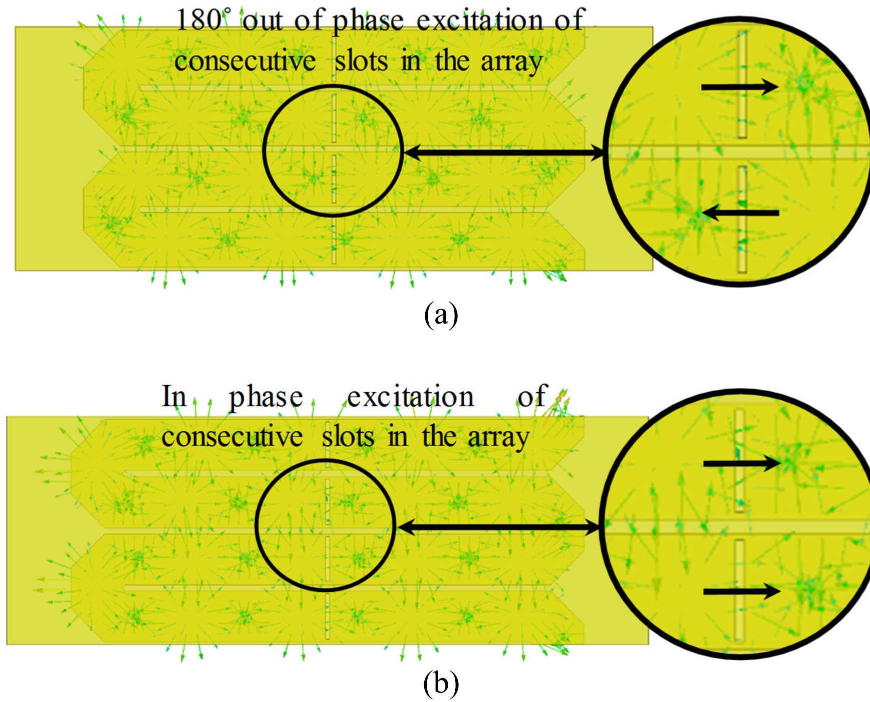

Figure 2.4. Field distribution along the meandered waveguide structure with adjacent elements excited with (a) l chosen to be a modulus of the waveguide wavelength where adjacent elements are fed 180˚ out of phase, and (b) l corrected by adding a $\lambda g_0/2$ waveguide segment for in phase feed of the adjacent array elements.

bonding. The minimum wall thickness between the adjacent waveguide lines, t, is determined by the thermo-compression bonding ability to reliably establish a metallic bond between the top and lower wafers across the wall as will be discussed in Chapter 6. For the current design a thickness of 100 μm with a waveguide segment length of 9.8 *mm* is chosen to ensure scan range of ±25˚. Longer value of l provides wider scan range at an expense of radiation efficiency due to additional propagation loss in the waveguide.

2.2.3. Narrow Beamwidth Requirement and Minimum Number of Elements

The array antenna is expected to have a very narrow beamwidth with a HPBW of around 2˚. To achieve this, the length of the antenna should be extended by using a large number of array radiating elements. The approximate minimum number of elements can be estimated using relation

($\alpha = \frac{\lambda}{L}$) where L and λ represent the total length of the antenna along the azimuth direction and the free space wavelength at the lowest frequency (i.e. 230 GHz), respectively. The length of the array for N radiating slots is given by $L=N(W+t)$. For $\alpha = 0.035$, $W=864$ μm (the width of standard WR-3 waveguide) and $t=100$ μm, the number of elements is calculated to be $N=44$.

2.2.4. Waveguide Dimensions for Achieving Minimal Loss

With the required large number of radiating elements, the overall waveguide length of the meandered structure becomes quite large (~ $193\lambda_g$ = 43 cm). This in turn increases the loss from the finite conductivity of the metalized wall of the waveguide and reduces the radiation efficiency of the antenna. Increased loss in the waveguide results into lower excitation of the end elements in the array which in turn increases the antenna beamwidth. Therefore, for optimum radiation performance of the antenna, accurate management of the loss in the waveguide is required.

One important factor affecting the loss in the micromachined waveguide is the choice of the metal deposited on its walls. However, this is mostly defined by the fabrication process and the physical and chemical properties of the metal. As will be discussed in Chapter 5, gold is a strong candidate due to its superior electric conductivity as well as its property for relatively low temperature and pressure for wafer to wafer bonding. Apart from the choice of the metal used for covering the walls of the waveguide, the dimension of the micromachined waveguide plays an important role in the attenuation rate of the waveguide. In a rectangular waveguide, the conductor loss is calculated from [85]

$$\alpha = \frac{R_m(2Hk_c{}^2+Wk_0{}^2)}{WH\beta_{TE_{10}}k_0Z_0} \tag{2.3}$$

where $R_m = \sqrt{\frac{w\mu_0}{2\sigma}}$, σ is the electrical conductivity, k_c the cut-off frequency of the waveguide, k_0 wavenumber, Z_0 free space characteristic impedance, W and H are width and height of the waveguide. As shown in Figure 2.5, the attenuation in the waveguide is reduced by increasing both the height and width of the waveguide. For minimum loss in the waveguide, the height of the micromachined waveguide is adjusted to the maximum allowable height for single-mode propagation in the waveguide. There is a tradeoff between optimal loss performance of the waveguide and the pattern of the antenna. Increasing the width of the waveguide for lower waveguide losses, results in a larger inter-element spacing in the array. Larger inter-element spacing leads to generation of grating lobes as the beam steers in the azimuth plane. Although the grating lobe can be suppressed by using spatial filters, this approach often require complex layered structures which are hard to fabricate. Another approach to avoid the appearance of the grating lobes at the end scanning angles while maintaining reasonable loss values, is to reduce the width of the micromachined waveguide to 600 μm or below where the angular separation of the main beam and the grating beam is over 115° (90°+25°=115°) and the grating lobe doesn't appear in the desired frequency range. This choice of width, however, results into very high waveguide losses that are not tolerable for realization of a narrow beamwidth with reasonable antenna radiation efficiency of higher than 40%. Therefore, the appearance of the grating lobe in the azimuth plane is inevitable but its' value can be reduced by the pattern of the radiating elements of the array. In other words, based on the array multiplication principle, the pattern of the array antenna, i.e. $F(\theta,\varphi)$, can be calculated from

$$F(\theta,\varphi) = AF(\theta,\varphi).\,g(\theta,\varphi) \tag{2.4}$$

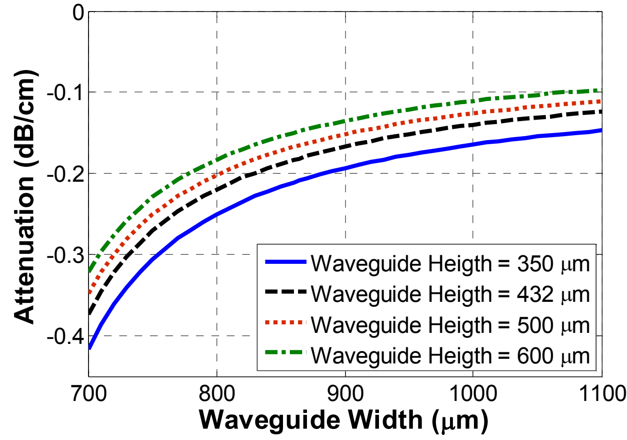

Figure 2.5. Simulated attenuation in the waveguide versus the width of the waveguide for different waveguide height values.

Table 2.2. One-dimensional array antenna parameters summary

	(μm)
Waveguide width (W)	864
Waveguide width (H)	580
Inter-element waveguide length (L)	980
Wall thickness (t)	100
Inter-element spacing (W+t)	964

where $g(\theta, \varphi)$ and $AF(\theta, \varphi)$ are the gain patterns of a single element and the array, respectively. The array element is chosen to provide much lower gain in the direction of the grating lobe compared to the main lobe. For relatively large (~λ or larger) values of waveguide width suppressing the grating lobe is hard to achieve, whereas for values less than 900 μm (~0.7λ) reasonable side lobe levels are realizable. The finalized one dimensional array parameters are summarized in Table 2.2.

2.3. Two Dimensional Array Design

In the previous section, a one-dimensional array with beam scanning range of close to 50° was presented in the azimuth plane. While the proposed one-dimensional array of slots generates

a narrow beam in the azimuth direction, it produces a relatively wide beam in the elevation direction. For many applications ranging from automotive radar to indoor mapping and navigation, the wide beamwidth is not desired as it capture reflections from other targets not in the direct path of the radar. Additionally, the wide beamwidth gives a low antenna gain and a poor detection range. To overcome these problems, the antenna aperture needs to be extended along the elevation direction to reduce the elevation beamwidth. One approach to achieve this is to introduce a second array along the elevation direction. Figure 2.6 illustrates the configuration of a slot-coupled series patch array where the energy from the slots is fed into a patch array placed on top of each slot to provide a narrow beam in the elevation direction. This array configuration has the advantage of choosing the elevation beamwidth without affecting the beam characteristics in the azimuth plane. The array consists of a center patch which is fed by the slot and the rest of the patches that are series-fed on both directions by the center patch. The reason for connecting series fed patch arrays on both sides of the center patch is to minimize beam scanning in the elevation direction as the frequency is swept. This limits the number of patch elements in the elevation direction. The design of the patch array is broken down into the following partitions.

2.3.1. Choice of Substrate for the Patch Array

Traditionally patch antennas are designed and fabricated on uniform dielectric substrates. However, to minimize the substrate modes, that can cause unwanted mutual coupling and loss of power in undesired directions, very thin substrates are needed. For instance, at the center frequency, 237.5 GHz, a 50 μm thick glass substrate or a 35 μm thick silicon wafer are around one tenth of the guiding wavelength for the respective microstrip patches. In such substrates a significant amount of surface waves can be generated and such substrates are very hard to handle during the microfabrication process. Additionally, the dielectric substrate with finite loss tangent

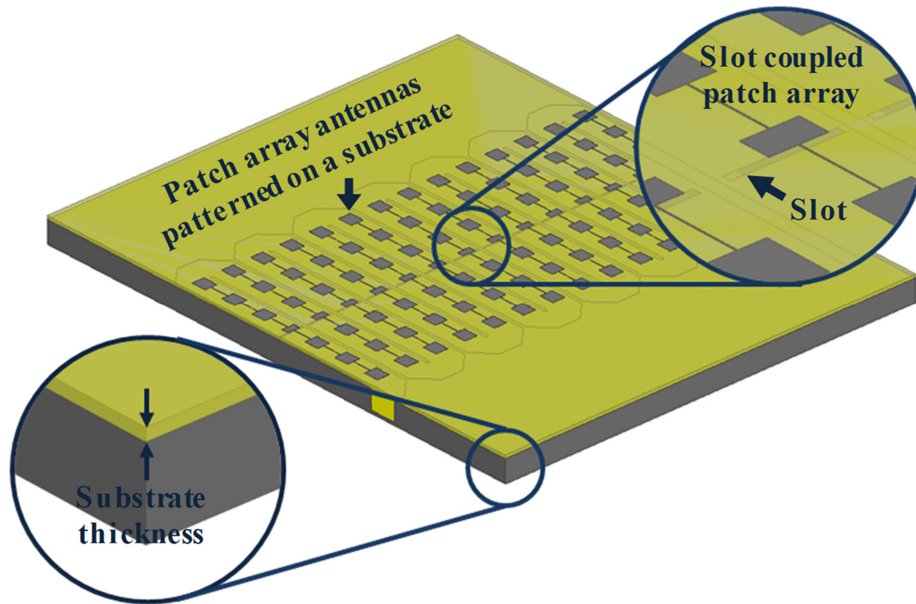

Figure 2.6. Configuration of a hybrid-coupled patch array where the energy from the meandered waveguide is fed into a patch array placed on top of each slot.

adds losses to the resonant patch antennas, resulting into lower radiation efficiency and gain. To avoid the problems associated with using a uniform dielectric substrate, an air substrate around the antenna can be used where the patch array is suspended on a thin layer of a dielectric membrane. This has the advantage of avoiding the dielectric losses while minimizing the excitation of the surface waves. It also improves the bandwidths. To support the membrane, silicon cavities around the patches and trenches around the microstrip lines are created, as shown in Figure 2.7 (a). This totally eliminates the propagation of the surface waves and minimizes the electromagnetic coupling among patch antenna elements. The cavity-backed patch array design also provides a physical support for the suspended membrane carrying the patch antennas.

2.3.2. Slot-Coupled Patch Design

In the proposed cavity-backed patch array design the depth of the etched cavity-backed trench defines the thickness of the air substrate. Since the patch antennas and the microstrip-lines

are made over cavities, a much thicker air substrate thickness than usual can be used. For robustness of design a 100 μm air substrate is considered. This corresponds to about λ/12 substrate thickness at the center frequency However, handling a full-size 4-inch wafer with a thickness of only 100 μm is very hard due to the fragility of the wafer. Additionally, the wafer is likely to break during the bonding process which occurs under high pressures and temperatures. A viable solution to this problem is to realize the cavity-backed trenches on a 250 μm thick silicon wafer and to extend the resulting metalized slot all the way through the wafer in order to excite the center patch. In effect in this approach the slot is transformed into an E-type waveguide junction where a controllable portion of the power is directed to the patch arrays. An overview of the proposed cavity-backed patch array structure with the extended slot is illustrated in Figure 2.7 (b). For a

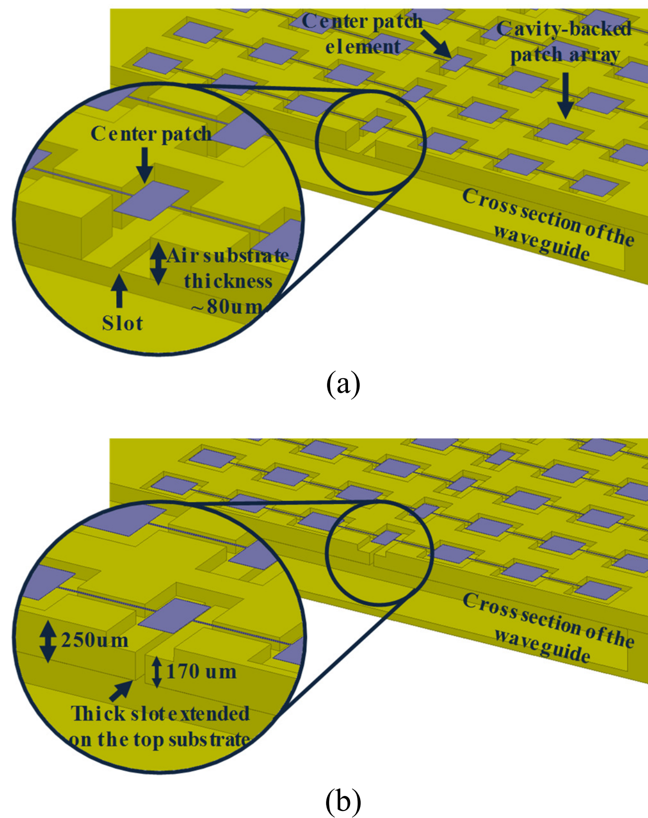

Figure 2.7. (a) Diagram of the cavity-backed patch array design with the patches patterned on a membrane layer and suspended ~80 μm over the slot, and (b) the slot extended through the top wall with a thickness of 250 μm, coupling to the patch array positioned 80 μm above it.

wafer thickness of 250 μm and an air substrate thickness of 80 μm, the slot height is 170 μm. The width and height of the slot waveguide can be adjusted to control the power percentage coupled to each patch array as will be discussed in the following subsections.

2.3.3. Suppression of Grating Lobes in the Azimuth Plane

As discussed in earlier, the appearance of the grating lobe in the azimuth plane is inevitable due to limitation on the width of the waveguide and wall separating the adjacent waveguides, but the level of the grating lobe can be controlled by proper design of the radiation pattern of the elements in the array. An optimum array element should produce a beam along the azimuth plane in such a way to sufficiently suppress the grating lobe in the azimuth plane. One way to achieve this goal is to use two side-by-side patch arrays fed by the same slot. This way the effective length of the array along the azimuth direction is increased and hence a narrower azimuth beam is generated. The two side-by-side patch arrays are used as shown in Figure 2.8 (a). Both patch arrays are fed through a single slot that is placed under the center patches. In Section 2.4 is shown that the two side-by-side patch array design is sufficient enough to achieve a side lobe level of less than 10 dB along the scanning plane. In continue the design of the patch arrays will be discussed.

2.3.4. Design of the Patch Array

To confine the beam in the elevation direction, a series-fed patch array is designed so that all the patch elements are excited in phase. In general, the design procedure of such an array can be carried out in two steps: 1) design of the series-fed patch array that is discussed in this sub-section, and 2) the design of the slot-coupled center patch. The series-fed array consists of patch elements and high impedance transmission lines connecting the patches. To form a standing-wave distribution over the patch array, the length of the connecting transmission-lines is half a guiding wavelength. This ensures that the electric field intensity at the end of one patch is duplicated at the

input of the next patch as the transfer matrix of the half-wavelength line is unitary. The connecting line can also be split into segments in order to provide a better control over the array excitation as well as the matching between the patches, if required [86]. For this radar application, an elevation antenna beamwidths of less than 10˚ is required. With a uniformly excited patch array with an inter-element spacing of half a guiding wavelength, 7 patch elements are required to achieve the desired beamwidth. This translates into two three-element series-fed patch arrays at each side of the center patch. For uniform illumination of the patches, the widths of the patches are all chosen to be identical. To achieve maximum radiation, the optimum patch width is approximated as $W =$

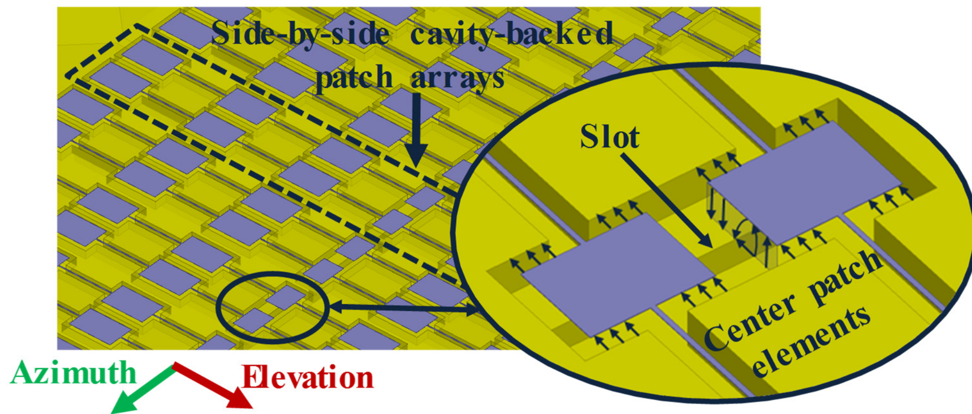

(a)

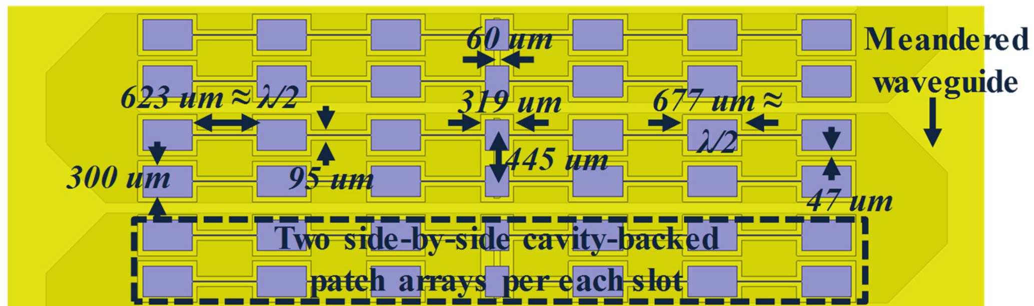

(b)

Figure 2.8. (a) Configuration of the cavity-backed patch array with two side-by-side patch arrays positioned per each slot to suppress grating lobe along the azimuth plane. (b) Seven element cavity-backed patch array design to provide 10˚ of beam confinement along the elevation direction.

$\frac{\lambda}{2}\sqrt{\frac{2}{\varepsilon_r+1}} = 630\ \mu m$, which exceeds the maximum patch width determined by the size constraint [87]. This is because the side-by-side placement of two patches on each slot requires that the width of the patches be chosen so that two patches can be accommodated over the width of the waveguide and the separating wall, 964 μm total width. This limits the maximum width of the patch to around 350 μm, considering the two patch array separation (50 μm) as well as the openings for the cavity-backed patch structure (50 μm).

As for the aperture-coupled patch excitation, the length of the center patch along with the width of slot are chosen to provide a uniform coupling from the waveguide to the patch array over the operation frequency range. The uniform coupling ensures achieving constant antenna efficiencies with frequency variations, as will be discussed in the next. Figure 2.8 (b) shows the configuration of the cavity-backed patch array structure with the optimized dimension for 10° beam confinement in the elevation plane. A lower beamwidth may also be achievable by extending the number of elements but caution may be taken as beam-split may occur in the elevation direction.

2.3.5. Antenna Efficiency

The antenna efficiency is a defined by the ratio of the radiated power to the total loss in the meandered waveguide and the patch antenna elements. For such a periodic antenna structure, this ratio is equal to the ratio per each turn in the meandered antenna. The power loss per each antenna turn is the total ohmic loss in the waveguide turn as well as the ohmic losses of the patch arrays. Based on the full-wave simulation of a single antenna turn, the total loss per each turn is about 5% of the total travelling wave in the waveguide. (In this simulation the conductivity of the gold is reduced to $6\text{x}10^6$ S/m to correspond with the measured micro-fabricated waveguide loss. The radiated power per each antenna turn, on the other hand, is a function of the coupled power to the

patch array elements, which can be controlled by adjusting the width of the slot. For higher antenna efficiencies, larger slot widths can be used to allow higher couplings to the patch elements.

In this design, an antenna radiation efficiency of 50% is targeted. Given that about 5% of the travelling power is dissipated per each turn in the array, the width of the aperture junction is adjusted to ensure at least 5% of power is radiated from each patch array. For wider aperture widths, the coupled power to each element is increased, resulting into higher efficiencies. However, increasing the coupling leads into a sharper power drop along the array elements in the azimuth direction and hence having a wider azimuth beamwidth and lower antenna directivity and perhaps gain. Increasing the number of radiating elements alleviates this problem by narrowing down the beamwidth but results into larger antenna area and mass, which is not desirable. Therefore, a tradeoff exists between the radiation efficiency and beamwidth.

2.3.6. Scan Blindness

As discussed earlier, in the meandered waveguide the length of the waveguide segment between the adjacent elements is designed so that all the elements are excited in phase at the center frequency. A large number of meandered waveguide segments are required to achieve the desired 2° beamwidth in the azimuth direction. Inclusion of many bends and existence of coupling slots on the broad wall of the waveguide all can generate very small reflections. These reflections, due to periodic nature of the structure, can add up coherently at the certain resonant frequencies, in this case the center frequency. In other words, for the frequency scanning antenna, there will be no radiation at certain angles (scan blindness). This is also validated by full wave simulation of the entire array where the antenna exhibits a large input reflection coefficient of approximately -3 dB at its input port, resulting in a 3 dB reduction in the radiation gain of the antenna.

One effective method to avoid the scan blindness is to introduce a perturbation within the waveguide where the reflection from those added perturbations approximately cancel out the reflections from the elements in the array at the resonant frequency. As mentioned earlier, there are two main sources of reflection per each element; 1) the 180˚ H-plane bend, and 2) the slot feeding the patch arrays. As discussed in Section 2.2, the bend is designed for minimum reflection

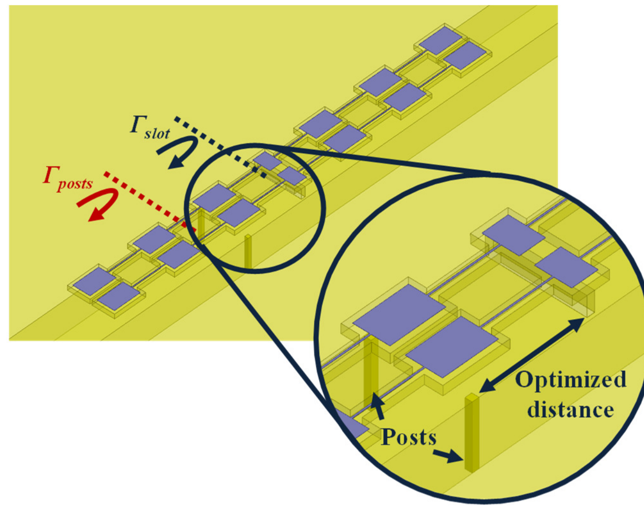

(a)

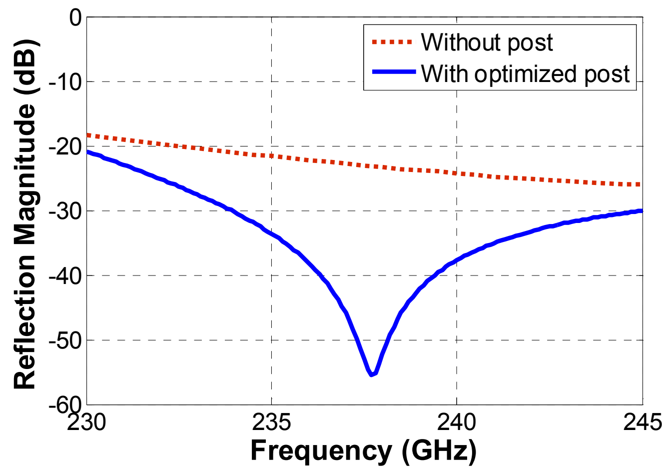

(b)

Figure 2.9. (a) Reflection cancellation pillars with optimized dimensions and distance from slots are devised to suppress scan blindness at the center frequency in the beam-steering array. (b) Comparison between simulated reflection from the slot with and without the reflection cancellation post. Reflection cancellation pillars offer less than -55dB of reflection coefficient at the resonance frequency.

with a realized reflection coefficient of less than -40 dB at the center frequency. This translates to a maximum reflection coefficient of -15 dB or better for all 44 turns if they were to add up coherently. However, the second source of the reflection, (the slots) produces a relatively large (around -20 dB) reflection which needs to be suppressed by a reflection cancellation technique. To cancel out the reflection from the slot at the center frequency, small pillars with optimized size and distance from the slot are introduced so that the reflections from these elements exactly cancels out the reflection form the slot at 237.5 GHz. A figure showing the proposed reflection cancellation posts is presented in Figure 2.9 (a). The pillars are designed to be readily compatible with the microfabrication process of the waveguide trenches, adding no addition step to the entire fabrication process. Figure 2.9 (b) illustrates the simulated reflection coefficient of single slot before and after adding the reflection cancellation pillars, showing a reflection coefficient of less than -55 dB at 237.5 GHz as opposed to -22 dB for the case without any pillars. A full-wave simulation of the entire array antenna with reflection cancellation pillars is also carried out. It is shown that by applying this technique, the reflection coefficient at the input port has dropped by over 30 dB to about -55 dB. This results into nearly 3 dB increase in the antenna gain and overcomes the scan blindness observed in the initial array design.

2.4. Simulation of the Beam-Steering Array Antenna and Summary of the Radiation Characteristics

The full-wave simulation of the entire beam-steering array antenna is presented in this section. To limit the overall length of the array to 4.5 cm, the number of array elements is set to 44 with two side-by-side vertical patch arrays per each coupling slots (Figure 2.10). With 7 patches per each vertical patch array, the entire array consists of over 600 radiating patch elements. A full-wave simulation (Ansoft HFSS) is used to carry out the antenna radiation characteristics using a

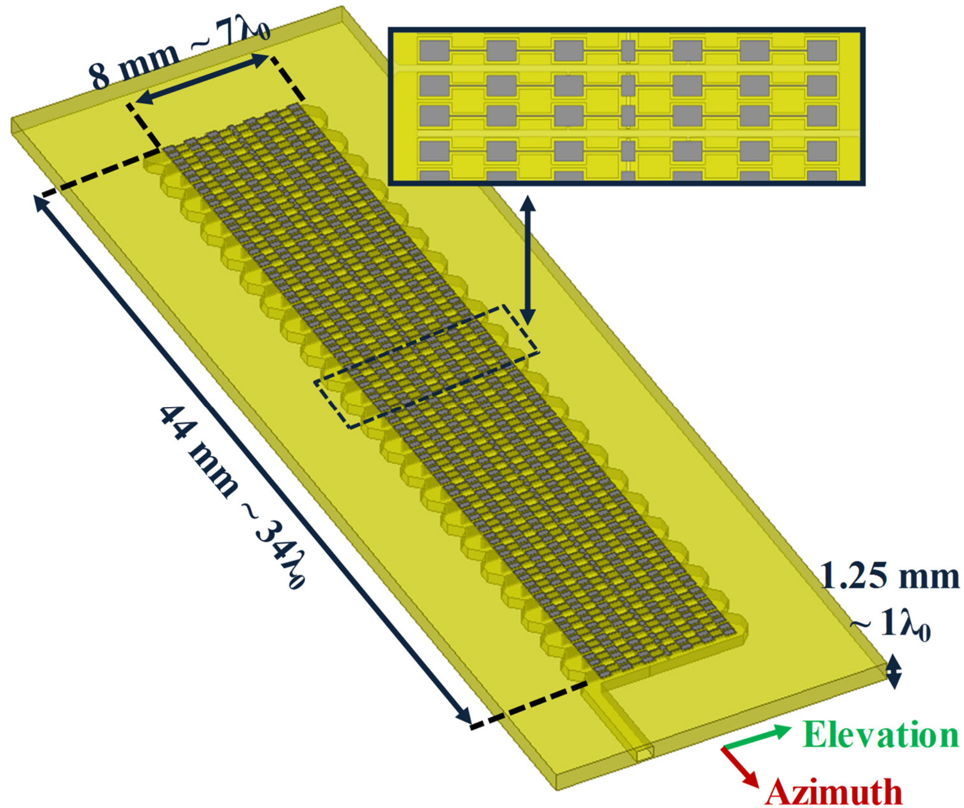

Figure 2.10. Schematic diagram of the complete array antenna with over 600 patch antenna elements as the radiating elements.

high performance computing facility at the University of Michigan. Considering the size of such an electrically large antenna, i.e. 7λ x 34λ x 1λ, each simulation at each individual frequency takes approximately 8 hours to successfully converge using 12 processors and 300 GB of memory. Due to large aspect ratio of the features used in the design over 5 million tetrahedral had to be generated at each individual simulation frequency to represent the geometry in the finite-element simulation tool. Figure 2.11 (a) and Figure 2.11 (b) illustrate the simulated radiation patterns of the antenna in the azimuth and elevation planes, respectively. The antenna generates a very narrow beam in the azimuth plane with a HPBW of less than 2.5˚ over the entire frequency range. It also generates a HPBW of less than 10˚ along the elevation direction. As the frequency sweeps from 230 to 245

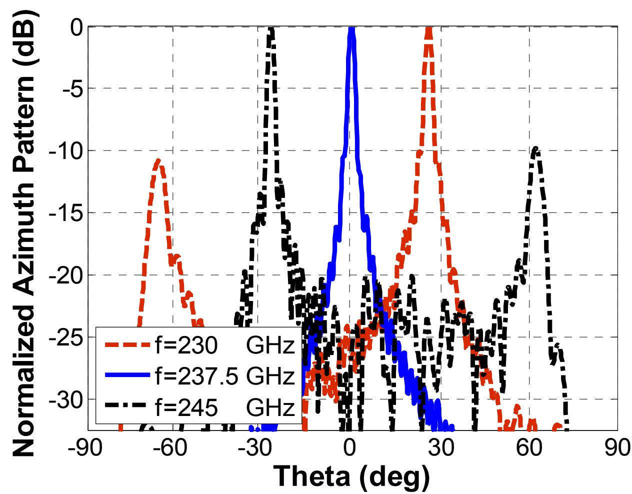

(a)

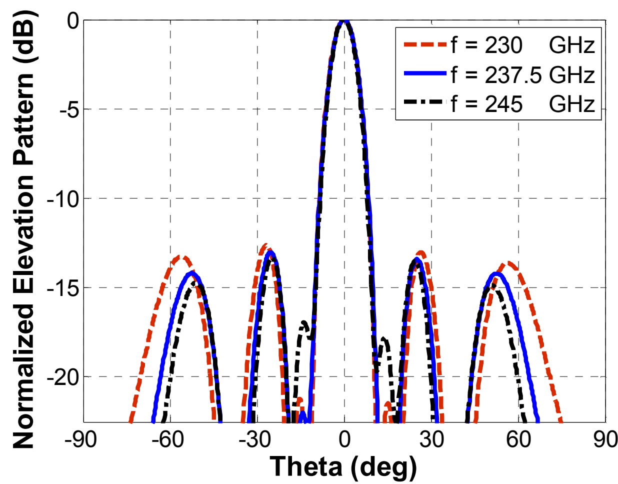

(b)

Figure 2.11. Simulated normalized pattern of the beam-steering array in (a) azimuth plane, and (b) elevation plane.

GHz, the azimuth beam steers from -24.1˚ to 24.7˚ with the beam directed right at the broadside at the center frequency, i.e. 237.5 GHz. It is also noted that using two cavity-backed patch arrays per each element, reduces the azimuth grating lobe level to -10 dB as desired and hence further improves the gain at the end frequencies. Figure 2.12 illustrates the radiation efficiency and gain

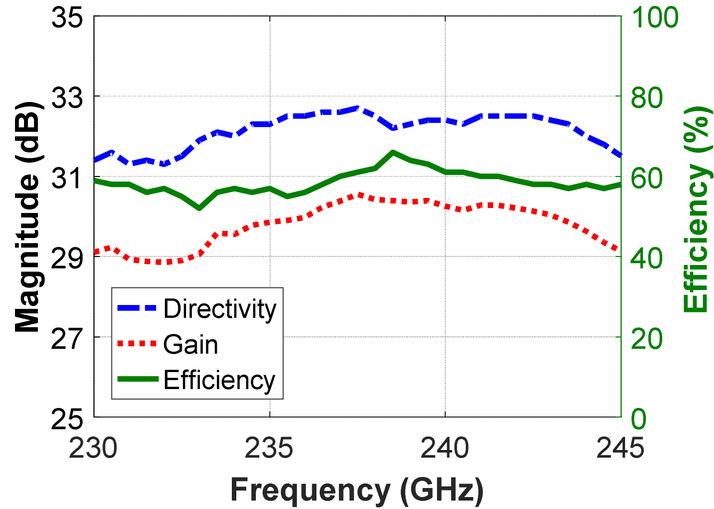

Figure 2.12. Simulated gain, directivity, and radiation efficiency of the beam-steering array over the operation frequency band.

of the antenna over the entire scanning range where a radiation efficiency of over 55% with a gain of over 30 dB is reported.

2.5. Summary

The design principles and simulations of a planar frequency beam-steering array antenna for a low-mass and compact radar are presented in this chapter. The proposed antenna array is a travelling-wave structure with a meandered hollow rectangular waveguide as the propagating medium. The array is designed to generate a narrow beamwidth in both azimuth and elevation planes, with a beamwidth (HPBW) of less than 2.5˚ and 10˚ in each plane, respectively. The entire array consists of over 600 radiating elements and exhibits a beam steering capability of approximately 50˚ around the boresight of the antenna. The antenna maintains a radiation efficiency of over 55% over the entire scanning range and provides a gain of over 30 dBi.

CHAPTER 3
CROSS-POLARIZED BEAM STEERING RADAR ANTENNA DESIGN

Radar polarimetric phenomenology studies show significant differences between the images created by the backscatter responses of vertical and horizontal polarizations. This is particularly the case at high MMW and sub-MMW frequencies as targets show higher cross-pol signatures at such high frequencies [88]. By combining these backscattering data from different polarizations, better understating of the nature of the target (such as geometry, shape, material, etc.) can be extracted [89], [90]. To enable such radar polarimetric capability, radar antennas with both co- and cross-polarizations are needed. To this end, a cross-polarized beam-steering antenna is devised in this work to enable polarimetric radar capability at sub-MMW frequencies. The cross-polarized antenna is designed to have the same fabrication process as of the co-polarized antenna to enable integration of both co- and cross-polarized antennas on a single 2.5-D micromachined radar. This chapter presents the design detail of the cross-polarized radar antenna for polarimetric radar applications.

Similar to the co-polarized antenna, the cross-polarized antenna is designed to provide a wide field of view with very narrow beam widths for high detection resolutions. A traveling-wave frequency scanning approach is utilized to provide 50˚, i.e. ±25˚, of beam steering around the boresight of the antenna as the frequency sweeps from 230 to 245 GHz. The array generates a very

narrow beamwidth of less than 2.5˚ for all scan angles in the azimuth direction. To confine the beam in the elevation direction series fed cavity-backed patch arrays excited by waveguide slots are designed. The HPBW of the patch array is about 10˚. The proposed array configuration provides a gain of over 26 dBi and exhibits a radiation efficiency of over 55% over the entire desired frequency range. The microfabrication of the antenna is carried out using a silicon micromachining technique and the microfabrication process along with the characterization results are presented in chapters 5 and 6, respectively.

This chapter is organized as follows. In Section 3.1, the design principles of the one-dimensional beam-steering antenna array where waveguide dimensions, inter-element spacing, number of array elements, and waveguide segment adjustments are discussed. Section 3.2. presents the design steps of the two-dimensional array and finally in Section 3.3, the simulation results of the entire antenna array are presented.

3.1. Antenna Design

3.1.1. Beam-Steering Mechanism

The design of the proposed vertically-polarized beam-steering antenna can be divided into two main steps: 1) design of a one-dimensional slot array antenna with the desired frequency scanning properties along the azimuth plane, which is carried out in this sub-section, and 2) design of the array radiating elements with the goal of confining the elevation beam and generating the desired polarization, as discussed in the following sub-sections. The proposed antenna is designed for large scanning angles, i.e. ±25°, around the broadside direction with a very narrow beam. In order to achieve the wide beam-steering requirement, a frequency scanning travelling-wave antenna structure is employed in this design. The design of the travelling-wave antenna is similar

to that of the horizontally-polarized antenna, where a hollow meandered rectangular waveguide is used as the travelling-wave structure with slot cuts placed on the H-plane of the waveguide wall as the radiating elements, as shown in Figure 3.1 (a). The length of the waveguide segment between two consecutive slots in the designed array, l, provides the desired phase shift as a function of frequency. As a result, as the frequency sweeps from 230 to 245 GHz, the phase shift between the consecutive elements changes and hence the antenna beam steers from -25° to +25°, with the beam pointing at the broadside direction right at the center frequency, 237.5 GHz. Additionally, the geometry of the 180° H-plane bends in the meandered waveguide structure is optimized using a full-wave simulator (Ansoft HFSS) to minimize the reflections from the corners. The geometry of a single element in the array antenna is shown in Figure 3.1 (b).

In addition to azimuth beam-steering requirement, the array antenna is expected to have a very narrow beamwidth with a HPBW in order of 2° in the azimuth plane. To achieve this, the length of the antenna is extended by using a large number of array radiating elements along the azimuth direction. In this case, 45 radiating elements are used to provide the required narrow beamwidth. Since the slots are all series fed, careful power management in the antenna structure is used to achieve desirable efficiency and narrow beamwidth. Specifically, the conductor loss in the waveguide is minimized by increasing the height of the waveguide to 580 μm.

3.1.2. Elevation Beam Confinement

While the proposed one-dimensional array of slots generates a narrow beam in the azimuth direction, it produces a relatively wide beam in the elevation direction. For many imaging and navigation applications, however, the wide beamwidth is not desired as it reduces the antenna gain and the detection range. Moreover, the wide beam results in capture of reflections from other

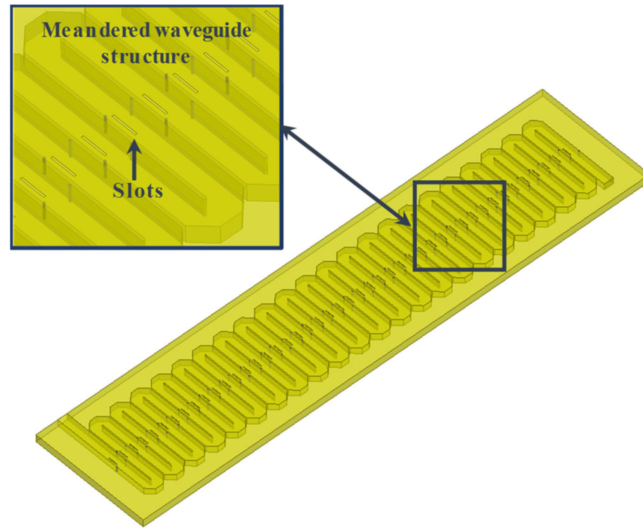

(a)

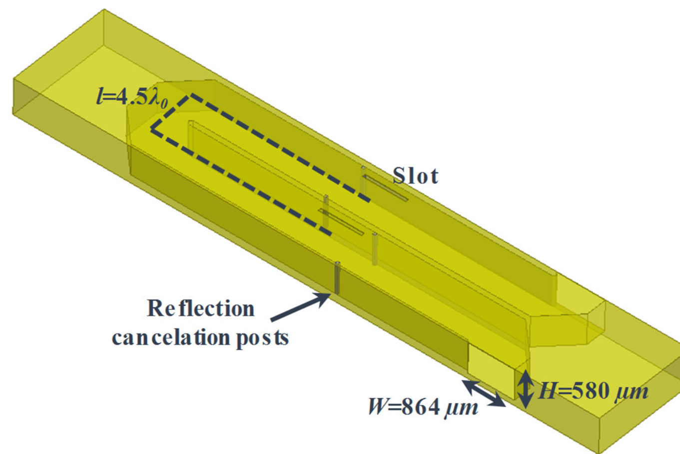

(b)

Figure 3.1. (a) Diagram of the travelling wave frequency scanning antenna consisting of a meandered waveguide structure with 180˚ H-Plane turns, and (b) the configuration of a single element in the array.

targets not in the direct path of the radar. To overcome these problems, the antenna aperture needs to be extended along the elevation direction to confine the beamwidth. Similar to the vertically-polarized antenna, this is achieved by introducing a second array of slot-coupled patch antennas placed above the slots. This way, the electromagnetic energy is fed from the slots into a patch array

placed on top of each slot with the goal of confining the elevation beam and generating the desired polarization. This array configuration has the advantage of choosing the elevation beamwidth without affecting the beam characteristics in the azimuth plane.

Following the same design process of the horizontally-polarized antenna, an air substrate cavity-backed patch array design is devised with the goal of confining the elevation beamwidth while generating the desired horizontal polarization. The main advantage of the cavity-backed design is that it suppresses the losses associated with the finite loss tangent of the substrates, especially at high MMW and sub-MMW frequencies. Additionally, the cavity-backed design also has the advantage of suppressing the excitation of surface-waves as well as the mutual coupling between the patch antenna elements. In the cavity-backed patch array design, the depth of the etched cavity trench defines the thickness of the air substrate. In this design, an 80 μm (~λ/12) air substrate is considered. However, since handling a 4-inch wafer with a thickness of only 80 μm is very hard in the fabrication process, a 250 μm thick wafer is used as the top wall and instead the slot is extended all the way through the wafer with the cavities realized on the reverse side.

3.1.3. Elevation Beam Confinement

One way to implement such a patch array structure is to use a corporate-fed patch array, where the electromagnetic power is coupled from the slots to the center line and is distributed to the patch elements through a corporate feeding network. While this structure provides the desired polarization, it suffers from the excessive losses in the feeding lines, which is not desirable. Another approach is to use a slot-coupled patch array structure, where the array center line is fed by the slot and the rest of the patches are fed through the center line, as shown in Figure 3.2. In this structure, a uniform phase distribution across the patches is required to generate the confined

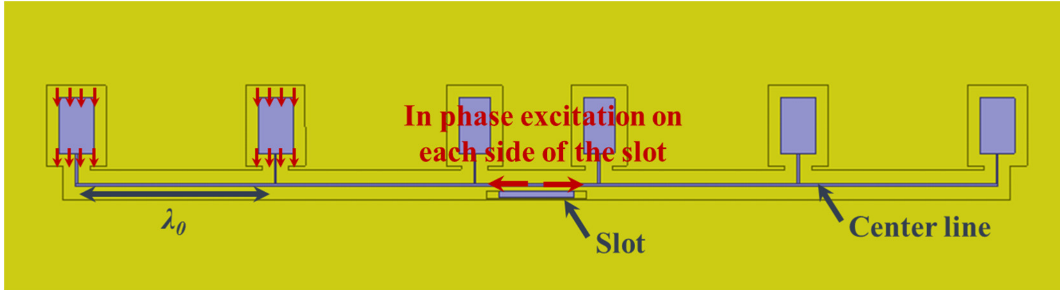

Figure 3.2. Diagram of the slot-coupled patch array implementation with the patch array elements separated by an inter-element spacing of one wavelength to provide in-phase excitation of all patch elements for bore sight radiation.

elevation beam. Since all patch elements are fed through the center line and the phase shift between them is realized through the inter-element delay line, the in-phase excitation of elements translates into λ_0 separation between antenna elements. This, however, results into appearance of the grating lobes in the elevation direction. To avoid this, the length of the line segment between the patches is set to $0.5\lambda_0$ and instead the orientation of the adjacent patches is flipped to provide the uniformity of the phase. Figure 3.3 (a) shows the configuration of the proposed patch array design with the field distributions on the patch elements showing in-phase excitation of all elements. This flip in orientation in effect provides an extra 180˚ of phase shift between the adjacent patches that together with the 180˚ phase shift from the $0.5\lambda_0$ inter-element line segment provides the desired in-phase excitation of the array elements.

The design of the proposed cavity-backed patch array is carried out in two steps, namely, the design of the series-fed patch array elements and the design of the slot-coupled center line. As for the patch array, the number of patch elements is defined by the desired elevation beamwidth. For this radar application, an elevation antenna beamwidths of less than 10˚ is required. With a uniformly excited patch array with an inter-element spacing of half a guiding wavelength, 10 patch elements are required to achieve the desired beamwidth. The patches are all fed through a high

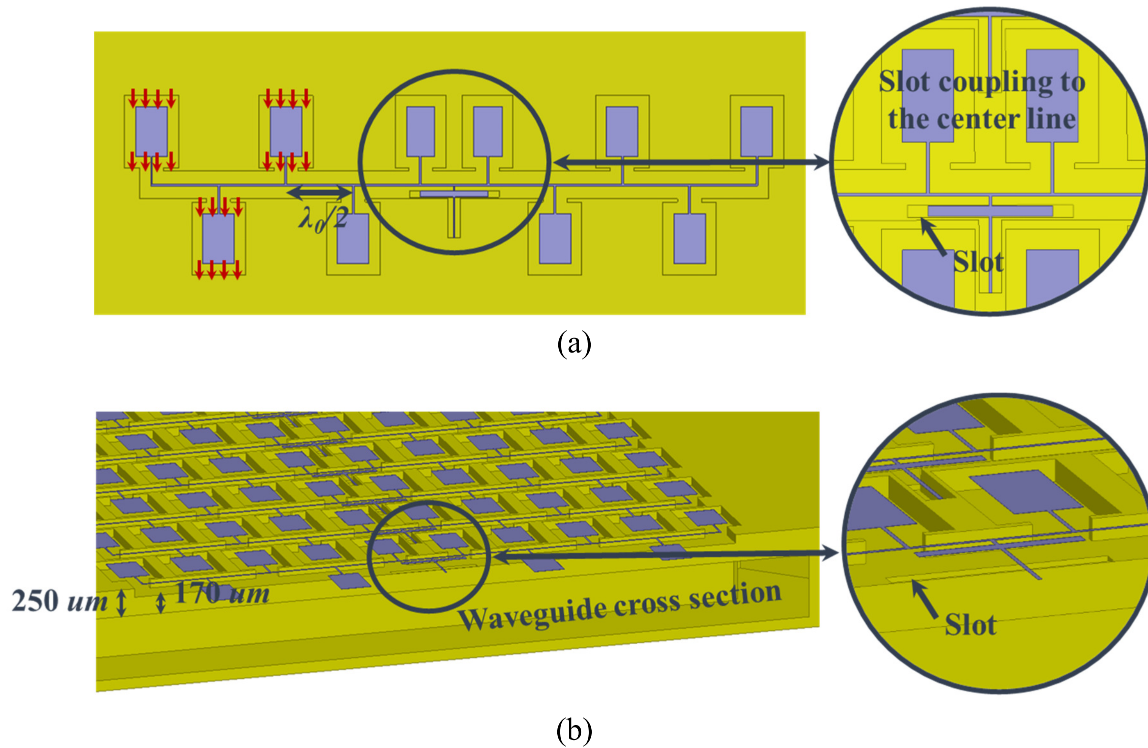

Figure 3.3. Schematic diagram of the proposed slot-coupled horizontally-polarized patch array design for beam confinement in the elevation direction. (a) Top view of a single patch array showing flipped configuration of the patch elements with half wavelength inter-element spacing, providing in-phase excitation of all antenna elements, and (b) 3-D view of the patch arrays positioned on the meandered waveguide. The electromagnetic power is coupled to the center patch and is distributed to the patch elements through the center line.

impedance cavity-backed center line which is excited by the extended slot positioned at the center of the line. Additionally, a strip is also placed at the middle of the line and above the slot to effectively couple the electromagnetic power from the slot to the center line, as shown in Figure 3(b). The width and height of the extended slot together with the dimension of the strip is adjusted to control the power percentage coupled to the center line. For larger slot heights, higher power levels are coupled to the center line which in turn leads into higher antenna efficiencies and vice versa.

3.2. Simulation of the Complete Horizontally-Polarized Patch Array Antenna

The configuration of the complete beam-steering horizontally polarized antenna is shown in Figure 3.4. The antenna consists of 45 elements along the azimuth direction with 10 patch antennas per each slot. The patch arrays are interleaved into each other to form a 2-D array antenna with 450 patch radiating elements. To validate the radiation characteristics of the antenna, full-wave simulation (Ansoft HFSS) of the antenna is carried out using a high performance computing facility at the University of Michigan, where 12 processors with 300 GB of memory are used to successfully simulate the antenna performance at each individual frequency. Due to large aspect ratio of the features used in the design over 5 million tetrahedral had to be generated at each individual simulation frequency to represent the geometry in the finite-element simulation tool.

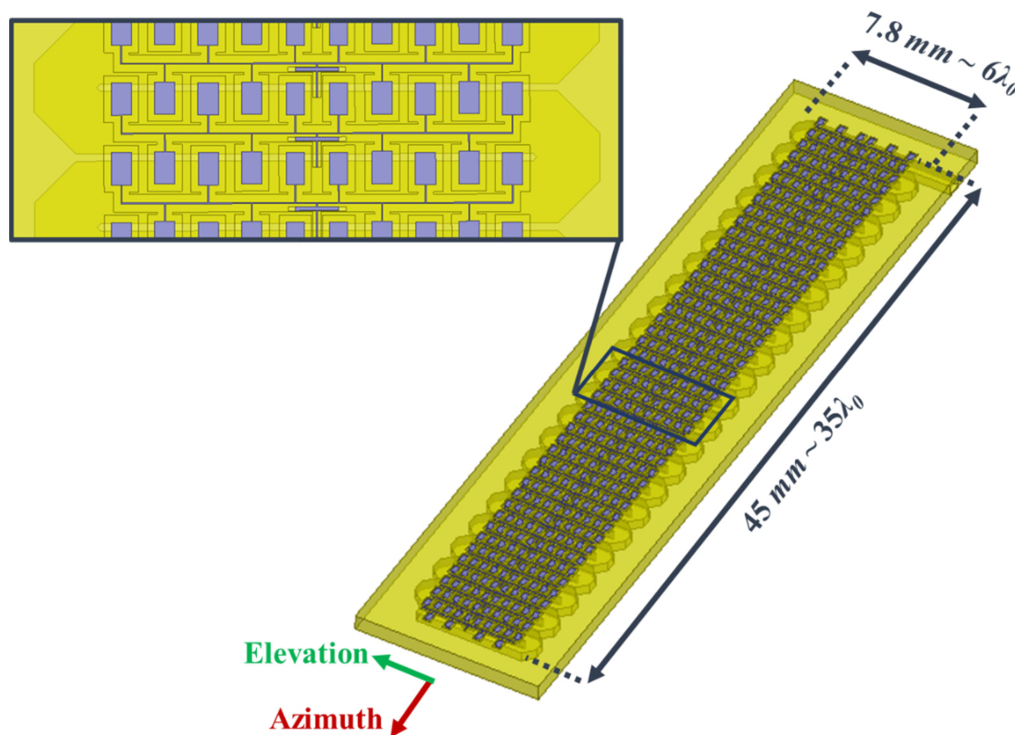

Figure 3.4. Schematic diagram of the complete horizontally-polarized array antenna with 450 patch antenna elements as the radiating elements.

Figure 3.5 (a) and Figure 3.5 (b) illustrate the simulated radiation patterns of the antenna in the azimuth and elevation planes, respectively. The antenna generates a very narrow beam in the azimuth plane with a HPBW of less than 2.5˚ over the entire frequency range. It also generates a

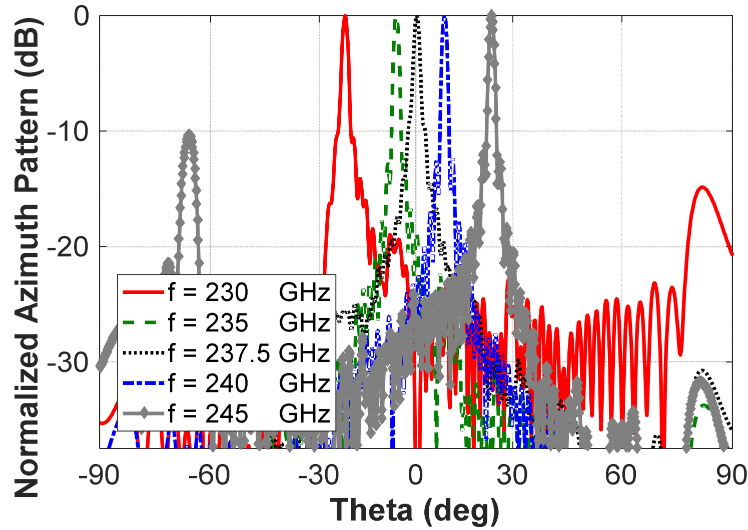

(a)

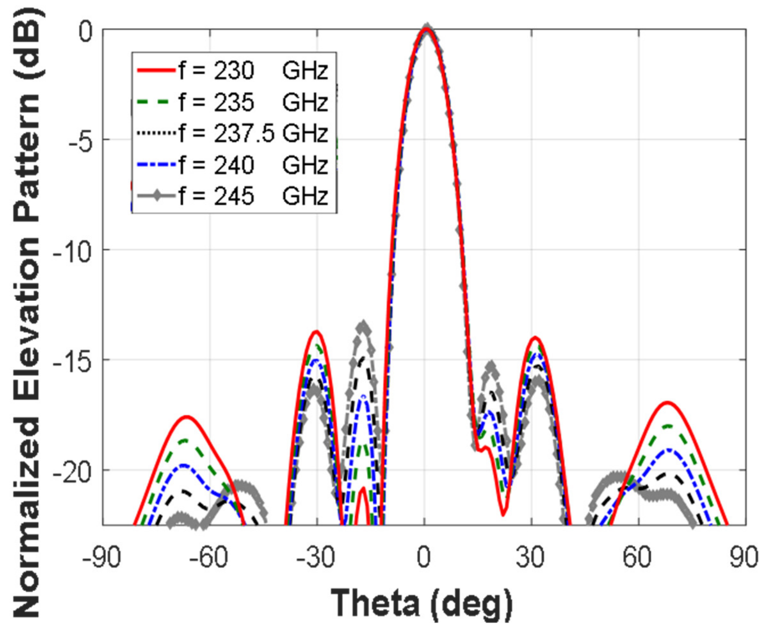

(b)

Figure 3.5. Full-wave simulated normalized pattern of the beam-steering array in (a) azimuth plane, and (b) elevation plane.

b)

HPBW of less than 10˚ along the elevation direction. As the frequency sweeps from 230 to 245 GHz, the azimuth beam steers from -23.1˚ to 23.8˚ with the beam directed right at the broadside at the center frequency, i.e. 237.5 GHz. Figure 3.6 illustrates the radiation efficiency and gain of the antenna over the entire scanning range where a radiation efficiency of over 55% with a gain of over 26 dB is reported.

3.3. Summary

The design principles and simulations of a novel cross-polarized frequency scanning array antenna are presented in this chapter. The cross-polarized antenna is designed to have the same structure and fabrication process as of the co-polarized antenna to enable integration of both co- and cross-polarized antennas on a single 2.5-D micromachined polarimetric radar. Radar polarimetric capability is specifically more important at high MMW and sub-MMW frequencies as targets show higher cross-pol signatures at such high frequencies. The proposed antenna array

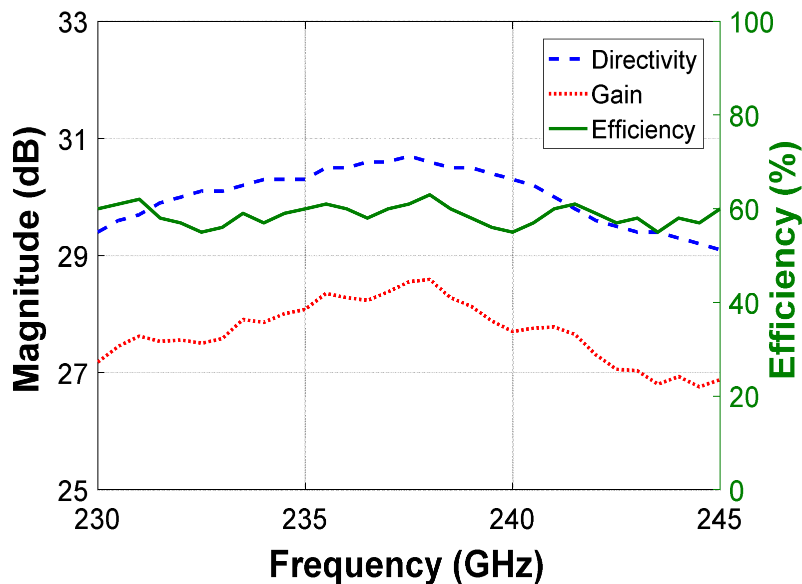

Figure 3.6. Simulated gain, directivity, and radiation efficiency of the beam-steering array over the operation frequency band.

is a travelling-wave structure with a meandered hollow rectangular waveguide as the propagating medium. The array is designed to generate a narrow beamwidth in both azimuth and elevation planes, with a beamwidth (HPBW) of less than 2.5˚ and 10˚ in each plane, respectively. The entire array consists of over 450 radiating elements and exhibits a beam steering capability of approximately 50˚ around the boresight of the antenna. The antenna maintains a radiation efficiency of over 55% over the entire scanning range and provides a gain of over 27 dBi.

CHAPTER 4
CHIP INTEGRATION AND PACKAGING

This chapter presents a novel chip packaging methodology for integration of active and passive MMICs in the radar RF front-end. As discussed in Chapters 2 and 3, the beam-steering antennas for the micromachined radar system are based on waveguide structures. This is partly due to the superior loss performance of waveguides compared to other types of transmission lines. Another advantage of waveguides is their compatibility with standard fabrication techniques at sub-MMW frequencies, such as silicon micromachining. Active MMIC modules, on the other hand, are most conveniently fabricated and integrated on planar transmission lines. To connect these devices to the rest of the system, appropriate transitions and packaging methods are required.

The dominant approach used at lower MMW frequencies is to use the wirebond technique to integrate MMICs with the on-wafer lines. However, the performance of this method is hampered at higher MMW frequencies as the effects of the parasitics associated with the wirebond are not negligible anymore (as shown in Figure 4.1). An alternative approach for integration of MMIC at lower MMW frequencies is to use the flip-chip technique, however, in this method the MMIC is exposed to high temperatures and pressures which is not desirable. A number of approaches for integrating MMIC modules with the rest of the system at the higher MMW frequencies have been reported in the literature [91], [92]. The principle of these methods is based on converting the coplanar or microstrip mode in the lines on the MMIC to the lines of the passive portion of the

system using a probe transition that is monolithically integrated on the MMIC chip. Although good performances have been reported, these transitions have complex 3-D geometries which require complicated machining fabrication process with assembly of various parts, which is expensive.

In this work a novel chip integration and packaging methodology for sub-MMW applications is introduced. The integration method is based on a peg and socket approach with transitions from the line on the active MMIC chip to the fabricated lines on a packaging block. In order to enable scalability to the THz regime, the transition and the mounting block are designed

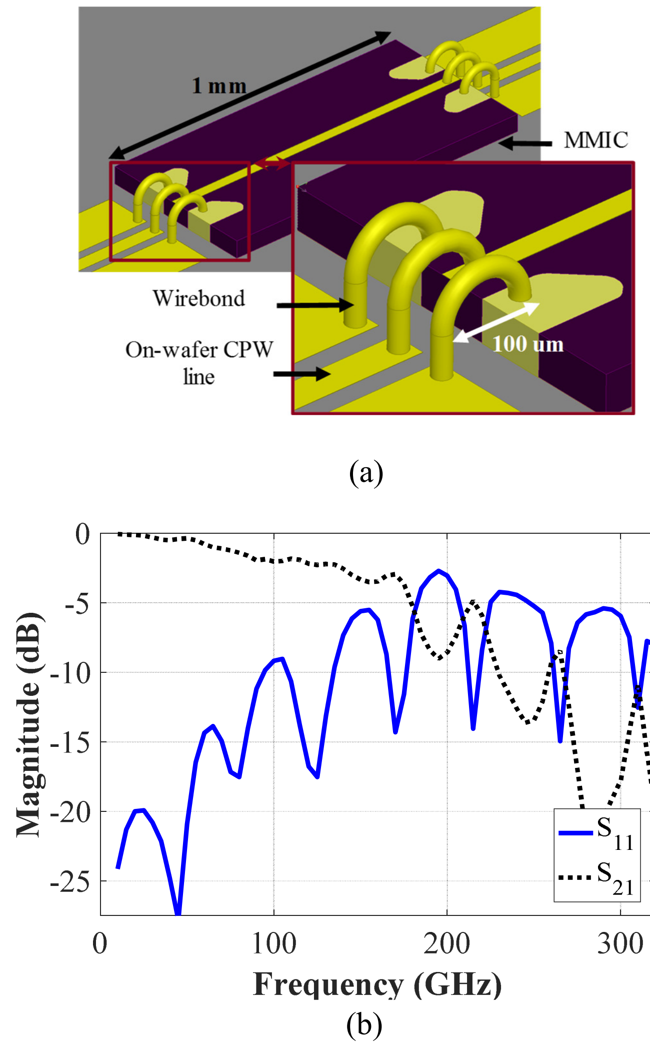

Figure 4.1. (a) Diagram of a wire-bonded chip for integration of active MMIC with the rest of the system, and (b) Full-wave simulated *S*-parameters of the back-to-back wire-bonded thru-line chip showing deteriorated performance of packaging with the increase in the frequency.

to be compatible with silicon micromachining technology which offers a standardized fabrication process with very high accuracies. This results into a compact and cost effective integration and packaging solution in the sub-MMW to THz frequency band which can be standardized for reliable and repeatable integrations at such frequencies. In order to enable biasing of the active MMIC, a seamless biasing network consisting of an ultra-wideband RF-choke with a decade bandwidth (30-330 GHz) as well as the associated DC pads are devised as part of the integration block. The broad-band isolation is particularly important to prevent possible instability of the circuits, as the devices have higher gains at lower portion of the MMW frequencies. In order to validate the performance of the proposed integration methodology a prototype is designed and microfabricated at WR-3 band (220-325 GHz) and excellent measured performance is reported. The new integration method is readily compatible with MMIC and silicon micromachining technology and should find a wide range of applications in sub-MMW frequencies. Here, we present results on this integration and packaging methodology.

This chapter is organized as follows. In Section 4.1, an overview of the chip packaging method as well as the simulated RF performance of the package is presented. Section 4.2 presents the design of the biasing network for integration of active devices, and finally Section 4.3 presents the sensitivity analysis of the package with respect to packaging errors such as misalignments or gaps in packaged pads. The microfabrication process and characterization methods and result of the chip packaging method are presented in Chapters 5 and 6, respectively.

4.1. Packaging Structure and Design

4.1.1. Packaging Structure

Figure 4.2 shows a diagram of the peg and socket chip integration configuration consisting of two bonded wafers that from here onwards are referred to as top and bottom wafers. The bottom

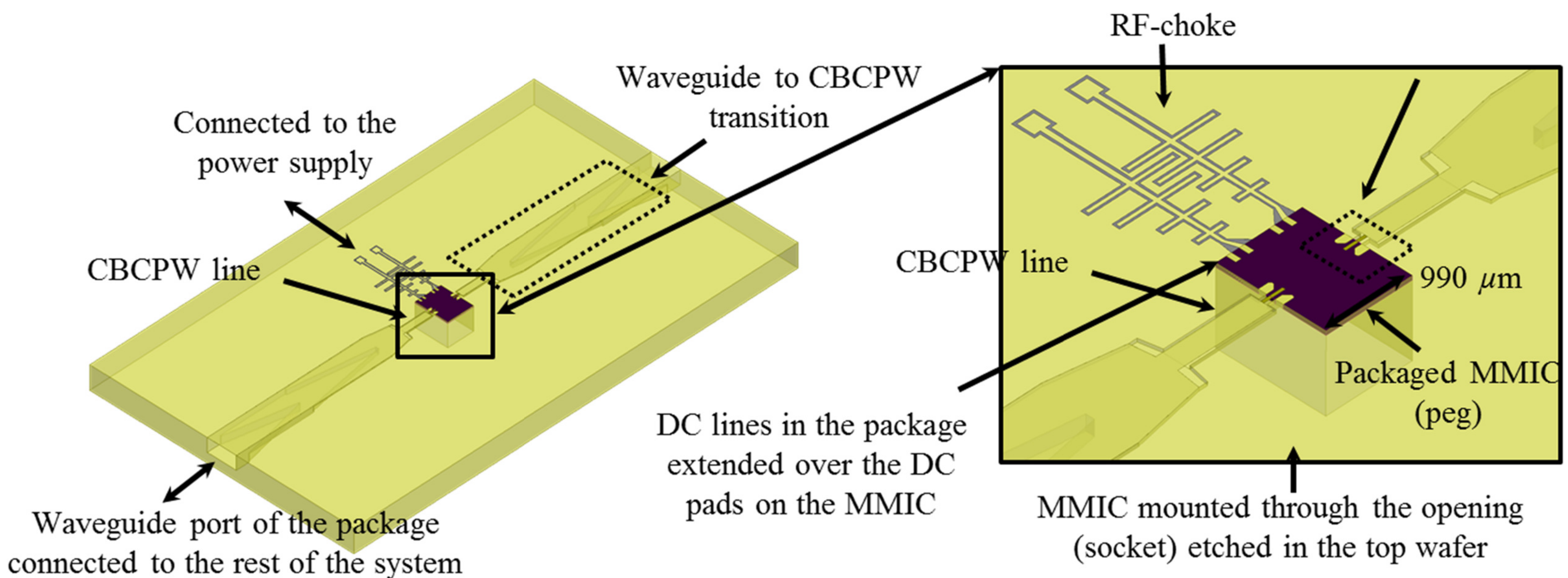

Figure 4.2. Schematic diagram of the peg and socket packaging block with the associated transitions and the bias circuitry for integration of active MMIC. The structure is composed of five main sections: a mounting block where the MMIC (peg) is inserted into the package (socket); RF transitions from the chip to the package RF lines; low-loss cavity-backed coplanar (CBCPW) on-wafer lines; transitions from CBCPW lines to on-wafer rectangular waveguides; and on-wafer bias circuitry with incorporated broadband RF-choke.

wafer consists of an opening to insert and mount the MMIC chip. The size of the opening is chosen based on the size of the chip to allow accurate placement and alignment of the chip with the lines and pads on the wafer. The chip is supported from the top by two ledges on the top wafer over the opening in the bottom wafer. The chip is inserted through the opening from bottom and then supported by a piece of silicon block. The top wafer consists of a membrane that RF and DC lines are patterned on it according to the position of the DC and RF pads on the MMIC chip. With the chip mounted in the opening, the traces on the membrane and the pads on the MMIC chip overlap and a physical contact is established between them. Also to facilitate DC contact between the two, many metallic cylinders with height of 5 μm and diameter of 10 μm are plated on the traces on the top wafer. The traces are next transitioned to RF cavity-backed coplanar waveguide (CBCPW) lines that extend to the next module in the system using a CBCPW to rectangular waveguide transition [75]. Once the MMIC is mounted in the socket, an etched silicon support is also inserted into the package to keep the packaged MMIC in place (as shown in Figure 4.3). As will be shown this method enables effective integration of the chip with other micromachined system modules with high level of accuracy and is a strong candidate for a standardized methodology for chip packaging and integration at sub-MMW and THz frequencies as it does not require a wire bond or soldering.

4.1.2. On-wafer CBCPW to MMIC Transition

To validate the performance of the integration method a prototype at WR-3 is designed and simulated using a full-wave solver (HFSS). In this design a 50 Ω CBCPW line is used to integrate different modules in the system. Although use of other type of lines is also possible, the CPW has the advantage of being readily compatible with most of MMIC applications. This is due to the fact that CPWs are the most widely used planar transmission lines in the MMIC chips due to their ease

of fabrication and integration of components in series or shunt. The cavity-backed feature also overcomes the inherent high insertion loss of the conventional CPW lines due to the presence of the dielectric substrate. The removal of the substrate in the CBCPW design also eliminates the excitation of the substrate modes and also supports the propagation of the TEM mode in the line which makes it preferable for wideband applications. Figure 4.4 illustrates the simulated RF performance of a back-to-back transition from the on-wafer CBCPW line to the microstrip line on a delay line chip. For a fair evaluation of the transition the insertion loss associated with the

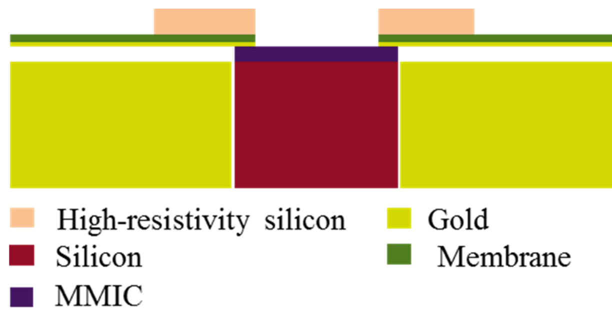

Figure 4.3. After insertion of the MMIC, an etched silicon block is also mounted in the socket to support the integrated MMIC in eth package.

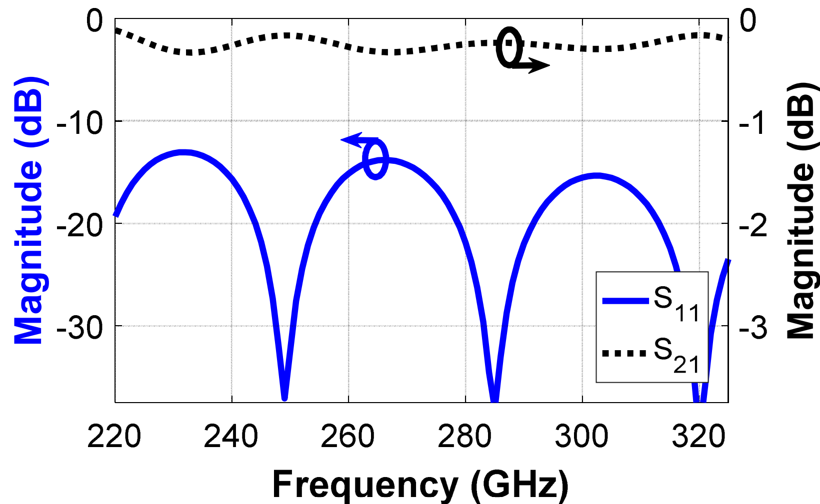

Figure 4.4. Full-wave simulated *S*-parameters of the back-to-back transition from the on-wafer CBCPW line to the microstrip line on a delay line chip. The results only include the losses associated with the package.

dielectric loss in the microstrip line and the conductor loss in the CBCPW line is eliminated. The result shows that the back-to-back transition has a reflection loss of better than 13 dB with an insertion loss of less than 0.4 dB over the desired bandwidth, i.e. 220-325 GHz.

4.2. Bias Network and Broadband RF-Choke Design

A wideband planar RF-choke compatible with silicon micromachining is designed to block the loading effects of the DC bias network from the RF circuit components and avoid the possible instability of the integrated active devices. The proposed RF-choke is composed of two sections, namely, the reflective and the lossy sections. The reflective part of the RF-choke is intended to block the RF signal by providing a high RF impedance. This is achieved by designing a series of open-ended stubs [as shown in Figure 4.5 (b)] implemented on a CBCPW line which is patterned on a high-resistivity silicon wafer. Figure 4.5 illustrates the configuration of the designed RF-choke. The dimensions of the stubs are optimized using a full-wave solver (HFSS) to achieve a high RF reflection over a wide bandwidth. The lossy section of the RF choke is implemented by an extended section of the CPW line (~1 mm) and is intended for a better RF isolation by further suppressing any leaked RF signal that has passed through the reflective section. Figure 4.6 shows the full-wave simulation of the proposed RF-choke showing an isolation of better than 10 dB with a reflection loss of less than 2 dB over the entire desired frequency range (40-330 GHz).

4.3. Packaging Sensitivity Analysis

Accurate alignment of the MMIC and the on-package RF and DC lines is very challenging and without a reliable method it can be the major error source in measurements. In our approach, the provision of the mounting block on the bottom side of the package restricts the possible sources of misalignment (rotation and lateral displacement) significantly. This window limits the probe

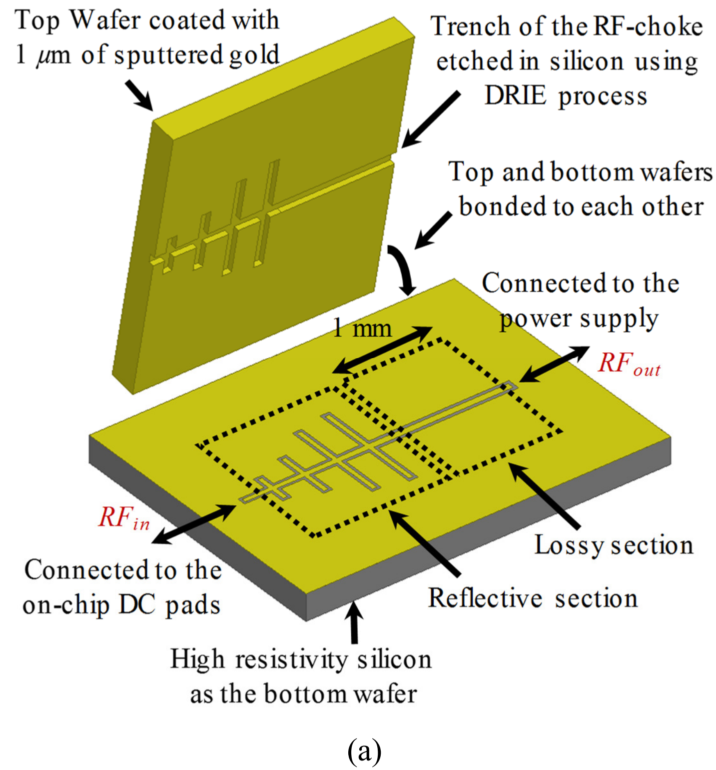

(a)

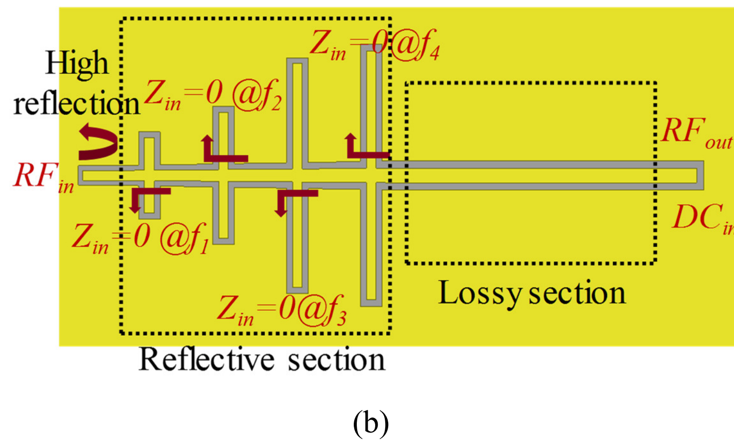

(b)

Figure 4.5. Configuration of the wideband RF-choke incorporated in the chip packaging block, (a) 3-D view, and (b) top view showing implementation of the RF-choke with a series of open-ended stubs with optimized dimension each tuned at different center frequencies.

positioning to a maximum of 10 μm. In addition to the misalignment errors, the packaging is also prone to non-ideal contact between the RF pads on the package and the on-chip RF ports. The gaps

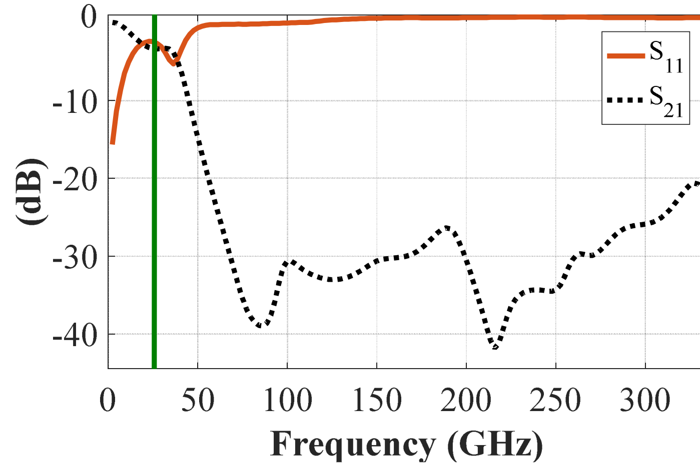

Figure 4.6. Full-wave simulated response of the proposed RF-choke showing broadband (40-330 GHz) isolation (>10 dB) of the two ports.

(up to 2 μm) can degrade the RF performance of the transition to some extent and its effect on the RF performance of the packaging scheme needs to be studied.

In order to validate the performance of the package with respect to the aforementioned sources of errors (d_x, d_y) [Figure 4.7 (a)], full-wave simulation study of the package is carried out and the results are presented here. Figure 4.7 (b) shows the sensitivity analysis of the package for different gap values between the packaged MMIC and the on-wafer lines. As shown, for gap values as large as 2.5 μm, the gap has minimal effect (less than 0.4 dB of loss) on the performance of the packaged MMIC. Figure 4.7 (c) also shows the sensitivity analysis of the package for possible misalignments between the on-chip pads and the on-wafer package lines, where misalignments as large 10 μm and 5 μm in y and x directions, respectively, only increase the insertion loss of the package by 1 dB or less.

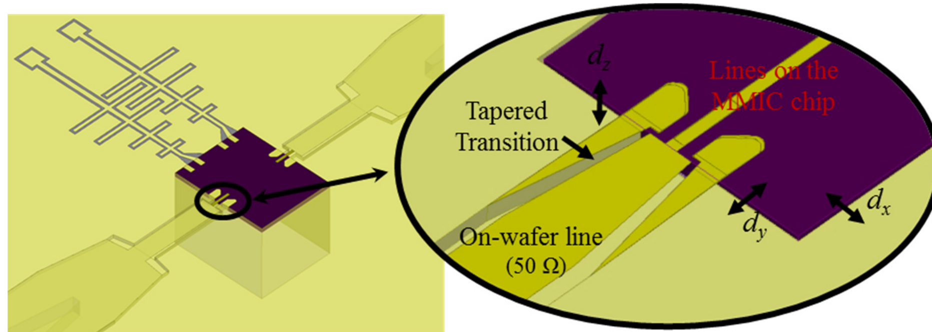

(a)

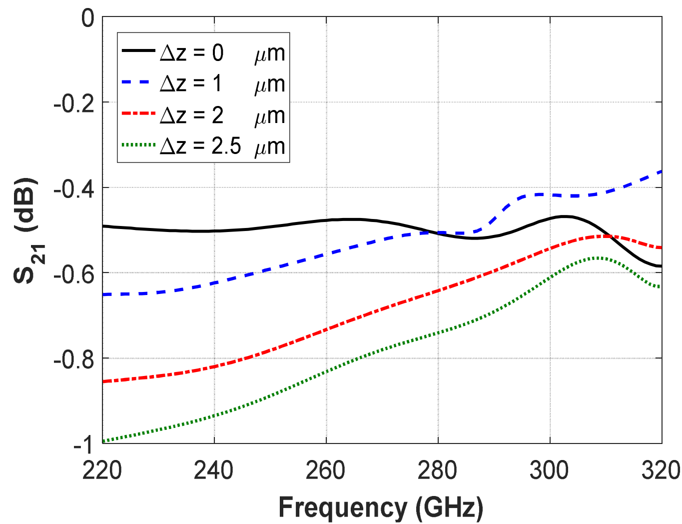

(b)

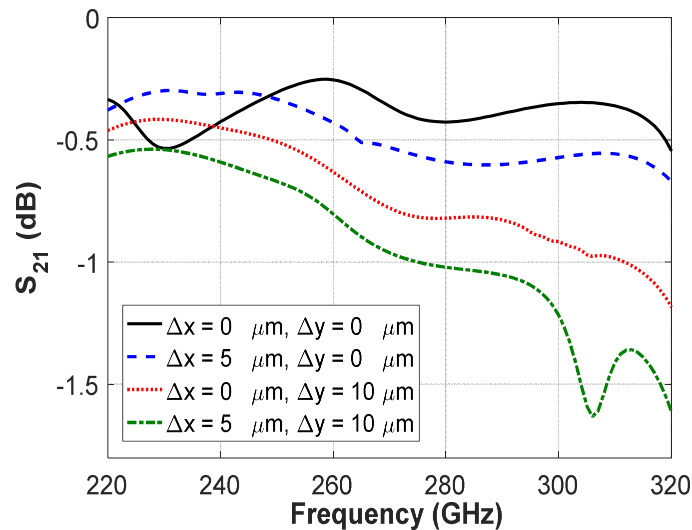

(c)

Figure 4.7. (a) Schematic diagram of the package with possible misalignments (d_x, d_y) and gaps (d_z) between the on-wafer pads and those of the MMIC, (b) full-wave simulation of the effect of the gaps on the RF performance of the package, and (c) sensitivity analysis of the RF performance of the package with respect to misalignments over the entire WR-3 band.

4.4. Summary

A novel packaging method for integration of active MMIC for MMW to THz band applications has been proposed and demonstrated. The packaging block and the associated biasing circuitry are designed to be compatible with silicon micromachining technology for high level of fabrication, low cost, and small form-factor. The high accuracy and repeatability of the fabrication technology also enables scalability of the packaging method up to THz frequencies, where is expected to find a wide range of applications in this area. The packaging method offers a low-loss integration solution for packaging the transceiver MMICs in the micromachined radar RF front-end. The fabrication and measurement information of the package is presented in the following chapters.

CHAPTER 5
MICROFABRICATION PROCESSES

This chapter presents the fabrication process for realization of the radar passive RF front-end, including the Tx and Rx beam steering antennas, antenna waveguide ports to cavity-backed CPW line transitions, and chip packaging blocks. At lower MMW frequencies, standard machining methods can be utilized to fabricate waveguide based components such as slot antennas or cavity-backed patch arrays similar to the ones used in the desired array antenna [93]-[95]. At higher MMW and sub-MMW frequencies, however, the implementation of these techniques is limited due to the small size of the components as well as the high degree of fabrication accuracy required. At these frequencies, microfabrication techniques are often used to fabricate such components [96]-[98]. The dimensions of the lines and waveguides shrink at higher frequencies and micromachining offers fabrication of complex structures with low mass and low cost with the required dimensional control. In this work, a silicon micromachining technique is developed to fabricate the entire radar front-end on a single silicon platform for high level of fabrication tolerance and accuracy.

The microfabrication of the beam-steering antenna is performed using three different layers. The first layer contains the trenches for the meandered waveguide structure of the phased array antenna as well as CBCPW line, the stepped transitions to connect the waveguides to the packaged chips, and E-bend multi-stepped transitions to feed the waveguide port of the antenna

for testing [76]. All the trenches and steps are micro machined on a thick silicon wafer, which is referred to as the bottom wafer. The second layer consists of the through wafer slots, the cavity backed trenches for the patch array antennas, and the opening for placement of the waveguide all of which are realized on a second silicon wafer referred to as the top wafer. This layer also provides the top wall of the meandered waveguide on the bottom wafer as well as the lines and transitions associated with the MMIC packaging blocks including membrane supported CBCPW lines, DC pads with the broad-band RF chokes, and the CBCPW lines to chip RF transitions. Finally, the third layer consists of a membrane layer with the patch array elements patterned on it. Figure 5.1 illustrates an overview of different layers in the microfabrication process of the radar RF front-end including the beam-steering antennas and the chip package with the associated transitions. As shown, once the trenches on the top and bottom wafers are realized, the wafers are gold coated and bonded together using the thermo-compression a gold-to-gold bonding process. Next, the third layer is attached to the bonded layers, which completes the fabrication of the radar front-end. The microfabrication steps of the front-end are described in more detail in the rest of this section.

5.1. Bottom Wafer

The micromachined waveguide trenches in the antenna are later coated with a layer of metal, so the choice of the material's electrical properties is not critical. Commonly, either photoresists or ordinary materials in microfabrication such as silicon or glass are used as the structural material in realization of waveguides at sub-MMW frequencies [99]-[102]. In case of the former, a thick layer of the photoresist is spun on a wafer and the photoresist is next exposed and developed to form the trenches for the meandered waveguide structure. For a waveguide trench as deep as the one used in this application, i.e. 580 μm, a very thick photoresist layer is required

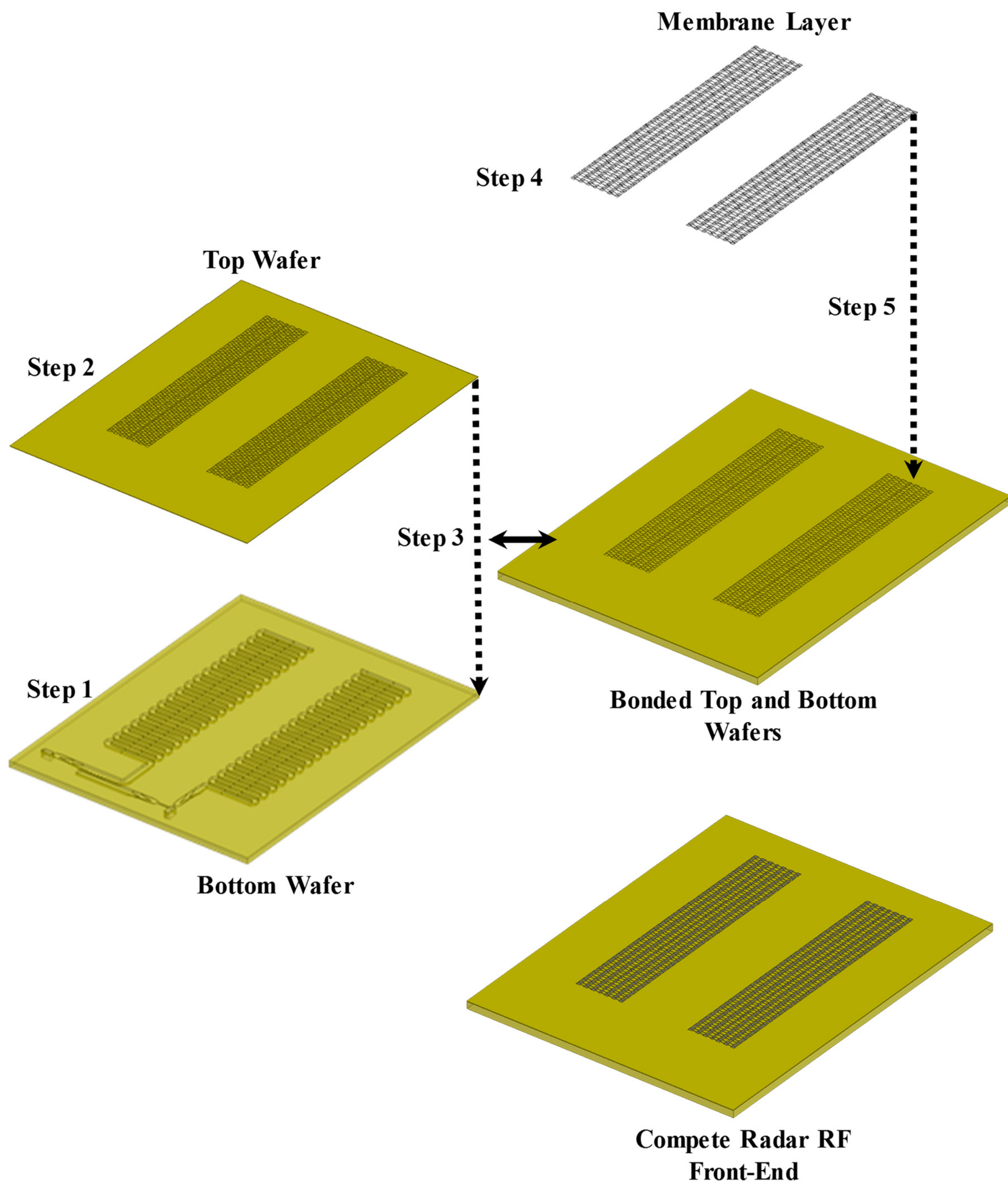

Figure 5.1. Overview of the radar RF front-end micromachining process. 1) The meandered waveguide trench as well as chip package socket and the associated transitions are etched in the bottom silicon wafer, 2) The slots, cavity-backed trenches for the patch array, and the DC and RF lines of the chip package are realized on the top silicon wafer, 3) Top and bottom wafers are metalized and are bonded to each other using thermocompression bonding process, 4) Patch array antennas are patterned on a thin membrane layer, and 5) The membrane is attached to the bonded wafers to complete the microfabrication of the RF front-end.

used photoresist which can be spun up to this thickness, but since the thickness of the photoresist is comparable to the thickness of the silicon, the built-in stress between the photoresist and the silicon wafer becomes significant, which in turn causes the thin walls in the meandered structure to fracture during the developing process. In addition to stress, fabrication of multi-stepped structures, such as the stepped bend transition for feeding the antenna, is not compatible with the photoresist approach. Another drawback of using SU-8 is that precise control over the thickness of the spun photoresist is hard to achieve compared to standard deposition methods. Moreover, the requirement for the uniformity of the thickness of the spun photoresist over a relatively large area, such as the antenna under investigation, is often very difficult to obtain. This is particularly important for the quality of the wafer to wafer bonding in following microfabrication steps. Considering these limitations, using standard micromachining materials, such as silicon or glass, appears to be the most suitable approach for fabrication of the antenna.

When using silicon or similar standard materials, the surface of the material is covered with a patterned mask layer and the material, itself is etched to form the meandered waveguide trench. Due to faster etch rates and superior compatibility with micromachining processes, silicon is the best candidate for the structural material in the antenna's microfabrication process. The etching of silicon can be performed using both wet and dry etching methods. Wet etching of silicon occurs along the crystal planes of the silicon wafer and results into sloped sidewalls. The DRIE process, which is a dry etching method, provides a highly anisotropic etch process with vertical sidewalls and is the most suitable approach for creating deep trenches with accurate control over the depth of the trench, as required in the antenna. Another advantage of the DRIE method is its capability in realizing multi-step structures, such as the stepped E-bend transition for probe. The DRIE

process is capable of realizing trenches with high aspect ratios such as the extended slot on the top wafer to be described later in this section.

The multi-step microfabrication process of the meandered waveguide trench and the stepped transitions from the waveguide port of the antennas to the CBCPW lines are accomplished using a multi-step etching process, shown in Figure 5.2. In this process, the 1 mm thick bottom wafer is patterned successively with different mask materials, in this case two layers of silicon dioxide and one layer of photo-resist. Next, each step is etched to the desired thickness using the DRIE process and then the corresponding mask layer is removed for the next etch. Figure 5.3 illustrates a close up of the bottom wafer where the structure of the metalized micromachined waveguide trench together with the reflection cancellation posts is shown.

As discussed in the Chapter 4, the chip package design contains a thru-wafer opening where the chip is inserted into the package. This opening is etched from the topside of the bottom wafer to the thickness of the waveguide trench. To open the backside of the opening for insertion of the

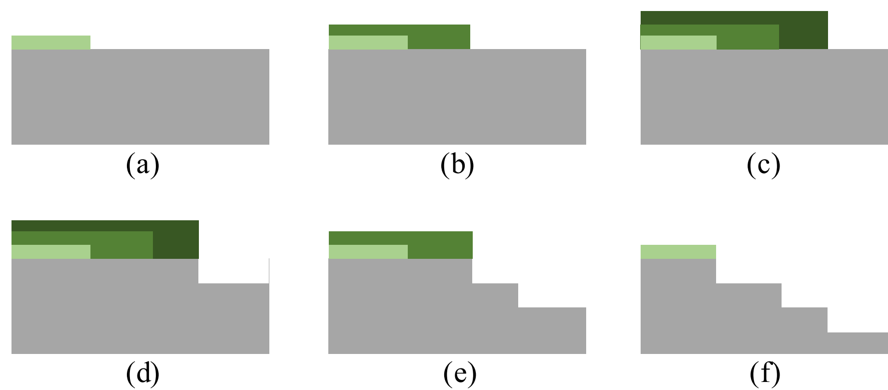

Figure 5.2. Multi-step patterning and etching process of the meandered waveguide trench in a thick (1 mm) silicon wafer. (a) Low pressure chemical vapor deposition (LPCVD) silicon dioxide (SiO_2) deposited and patterned as the first mask layer, (b), (c) Plasma-enhanced chemical vapor deposition (PECVD) SiO_2 deposited and patterned as the second and third mask layers, (d), (e) and (f) first, second and third steps are etched in the silicon wafer using Bosch deep reactive-ion etching (DRIE) process and the corresponding mask layers are removed after each etch.

chip, the mounting opening is also etched from the reverse side of the bottom wafer. Additionally, to facilitate the placement of the chip, the opening is designed to be larger much than the size of the chip. The etching process follows the same DRIE process as described above, where a 5 μm thick SPR 220 (3) photoresist layer is used as the mask layer. Figure 5.4 illustrates the thru-wafer

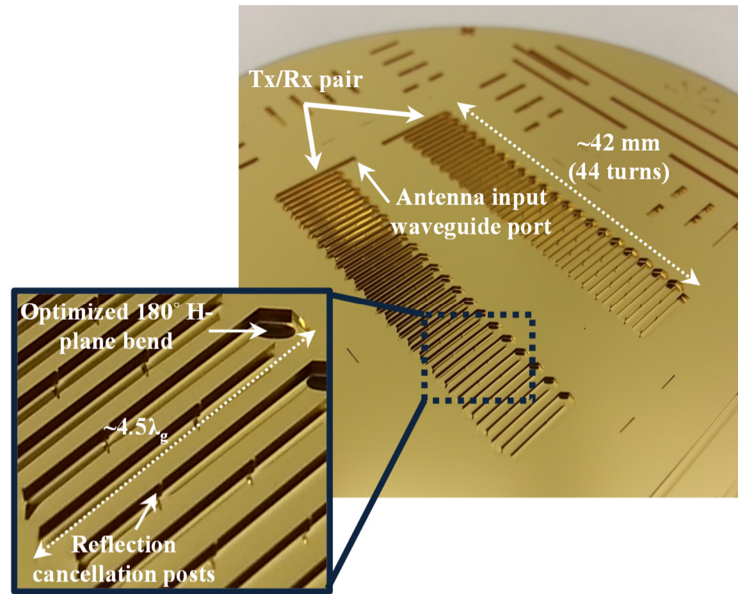

Figure 5.3. Gold plated bottom wafer containing the meandered trench of the waveguide structures for two side-by-side antennas. The close-up highlights microfabricated reflection cancellation posts in the meandered structure.

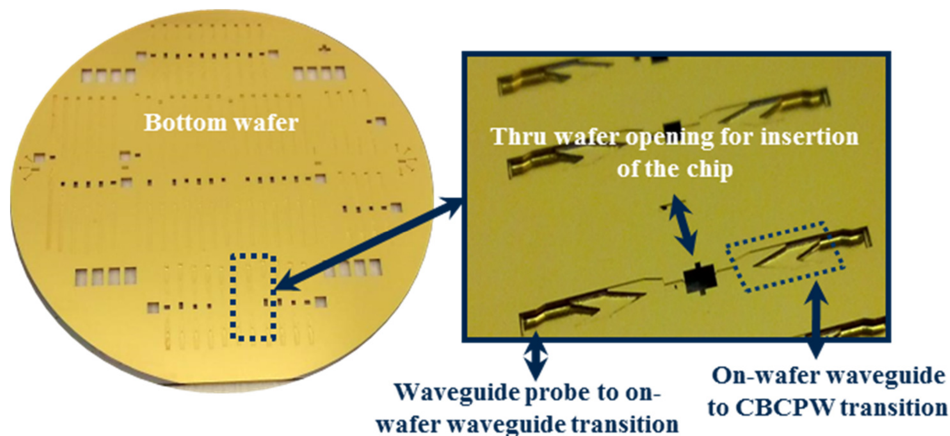

Figure 5.4. Thru-wafer opening etched in the bottom wafer for mounting the MMIC in the package. Multi-step waveguide to CBCPW trench as well as waveguide probe to on-wafer waveguide transitions are fabricated on the bottom wafer using the multi-step microfabrication

etched opening for mounting the MMIC in the package as well as the multi-step waveguide to CBCPW trench fabricated on the bottom wafer using the multi-step microfabrication process.

5.2. Top Wafer

The microfabrication of the top wafer follows a similar process to that of the bottom wafer where the DRIE Bosch process is used to etch the trenches for the cavity-backed patch array as well as the trenches for the membrane supported CBCPW lines on the top side of a 250 μm thick silicon wafer. The top side of the top wafer also includes the probe opening for charachterization of the waveguide based components. The same process is also used to etch the thru wafer slots on the reverse side of the wafer. The bottom side of the top wafer also contains the membrane-supported CBCPW lines and the RF chokes that are patterened on membrane layer. The membrane layer is required to have a very small thickness for minimal effect on the performance of the designed CBCPW lines. Additionally, the it should be robust enough to stand as a membrane layer and to be able withstadning high tempretures (~380° c) in the bonding process. In this process, a 2 μm stack of Low Pressure Chemical Vapor Deposition (LPCVD) SiO_2 –Si_3N_4 –SiO_2 stress-free dielectric layer is chosen and deposited on the bottom side of the top wafer. Next, titanium and gold are deposited and patterened on that layer to realize the CBCPW lines and transitions as well as the RF chokes on the top wafer. A micrograph of the top wafer for the vertically polarized beam-steering antenna is shown in Figure 5.5.

The microfabrication of the top wafer for the chip package is similar to that of the antennas. The chip package top wafer contains the patterns of the CBCPW traces and the transition to the RF pads which are patterned using gold lift-off process over a 1 μm thick layer of SiO_2–Si_3N_4–SiO_2 (ONO) membrane deposited over it. Additionally, in order to facilitate the DC contact of the RF and DC lines of the package to those of the MMIC, gold pilars of the height of 5 μm are plated

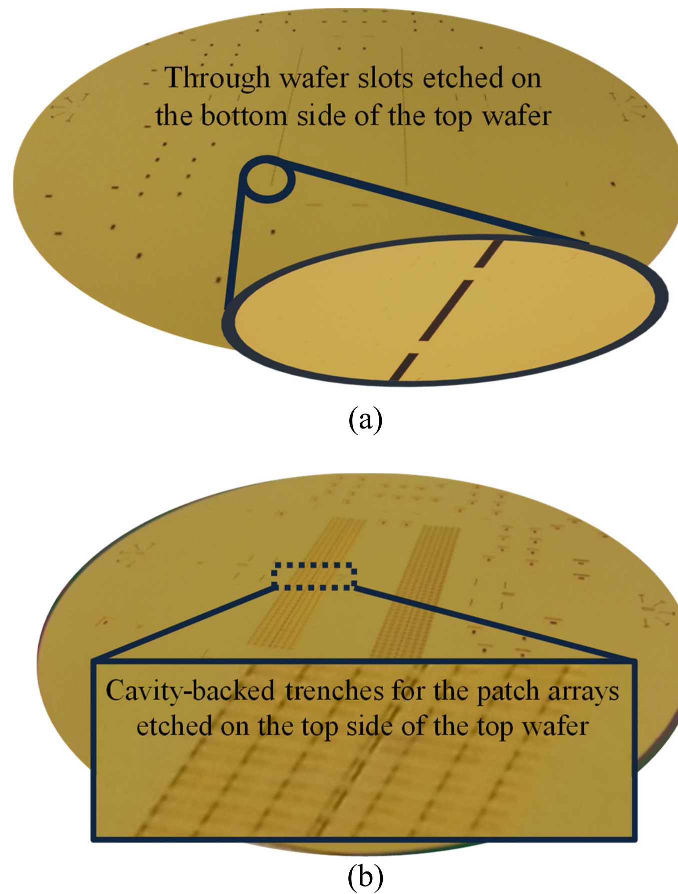

Figure 5.5. Microfabricated top wafer with slots and the cavity-backed patch array trenches etched on both sides of the wafer, (a) top view, and (b) bottom view.

on the on-package RF and DC pads. The topside of the top wafer over the CBCPW line and the pening for the chip mounting is also etched down to the membrane layer using the DRIE silicon etch process. A micrograph of the chip package top-wafer is shown in Figure 5.6 where the CBCPW lines together with patterened RF choke are shown.

5.3. Gold Deposition and Bonding

Once the top and bottom wafers are microfabricated, they are metal coated and bonded to each other to form the desired meandered waveguide structure for the one-dimensional array antenna. Due to superior electric conductivity as well as feasibility for further fabrication processes

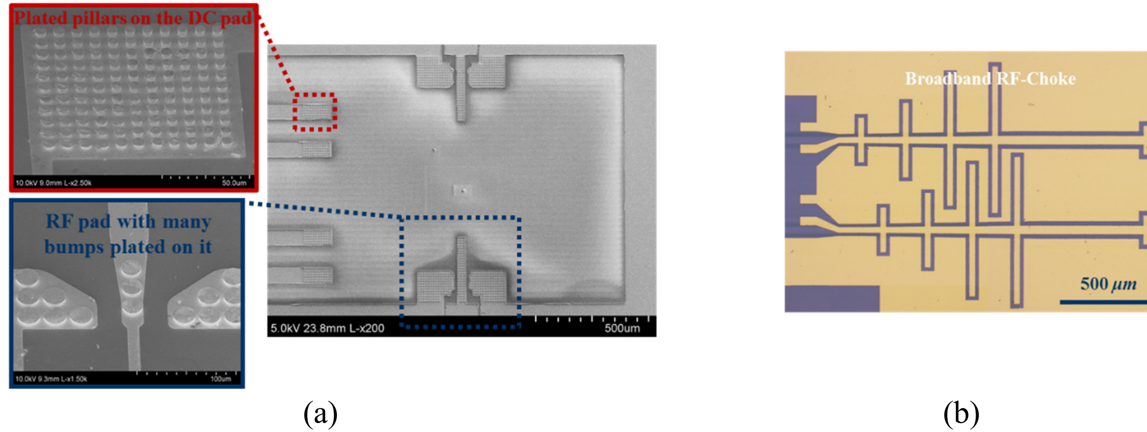

(a) (b)

Figure 5.6. (a) Scanning Electron Microscope (SEM) of the package top wafer showing the gold plated pillars on the RF and DC pads, and (b) close up of the broad-band RF-choke and the netwrok for biasing active MMIC.

such as wafer to wafer bonding, gold is a strong candidate for this process. In order to ensure that the sidewall of the etched trenches on both top and bottom wafers are fully covered with gold (Au), a sputtering gold deposition process is used to deposit 1.5 μm of gold with a thin layer of titanium beneath it on both top and bottom wafers. The titanium (Ti) layer has a thickness of 150 nm and is used to promote the adhesion of gold to silicon, as desired. The sputtering process ensures a sidewall coverage of over 50%, i.e. 750 nm of gold in this case, which is sufficiently thicker that the skin depth of gold at these frequencies (around 150 nm). A micrograph of the waveguide sidewall after the gold deposition process is shown in Figure 5.7 (a) where the high quality of the coating is verified.

The next step after metallization of the two wafers is to bond them using a gold-to-gold thermocompression bonding process occurring at high pressures and temperatures. In this case, the bonding is performed at a pressure of 210 N/cm^2 with a temperature 385˚C for 45 minutes [104], [105]. One issue with exposing the coated wafers to such high temperatures is the diffusion of gold into the silicon which results into deteriorated bonding qualities as well as impurity of the

metal and hence high waveguide losses. To avoid these problems, a thin (2 μm) layer of silicon dioxide is deposited beneath the gold and titanium layers as the diffusion barrier. The quality of the bonding is confirmed by dicing the bonded sample at different spots and inspecting the bonding interface, as shown in Figure 5.7 (b).

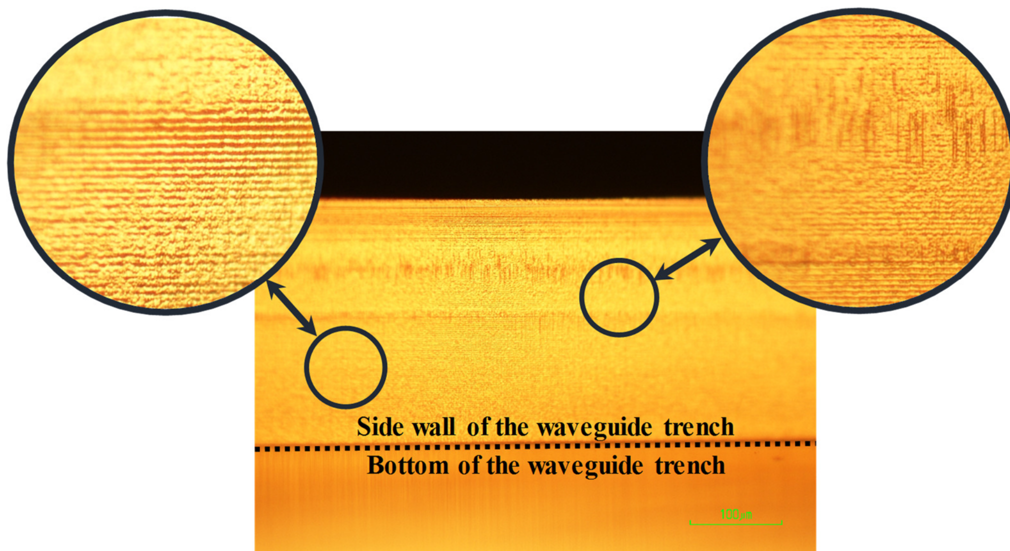

(a)

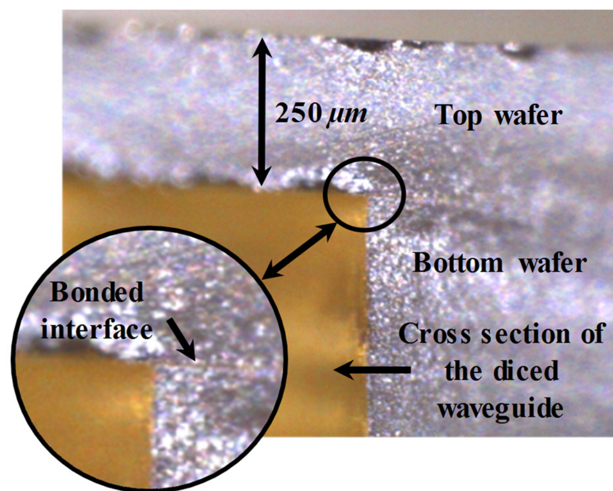

(b)

Figure 5.7. (a) Cross-section of diced waveguide section confirming metallization of the etched waveguide trenches, and (b) Micrograph of the diced waveguide showing the quality of the gold-to-gold bonding at the bonding interface.

5.4. Patch Array Elements over the Membrane

The patch array structure consists of 44 × 2 = 88 (two per each slot) seven-element patch sub-arrays, i.e. a total of 616 patch elements per each antenna. These elements and the connecting lines are realized over a membrane and are suspended on top of the air substrate of the cavity-backed trench. The patterning process of the patches is performed using a standard lift off process where evaporated gold is deposited on a patterned layer of photoresist which is next removed to complete the patterning. It is clear from the lift off and the membrane attachment processes that a membrane layer with high elasticity and low stress is required for this application. This eliminates the use of ONO layer as it cannot be suspended over a large area. Another constrain on the choice of the membrane layer is that it should not react with the standard solvents which are used in the lift off process, such as acetone or isopropyl alcohol (IPA). This also eliminates the choice of photoresist based membranes. Given these constrains, polymer based membranes such as Parylene is a suitable option for this application [106]. Figure 5.8 shows the microfabrication and attachment process of the patch array elements. In this process a 5 μm thick Parylene layer is used as the membrane layer where the patch array antennas are patterned on it using the lift off process. The Parylene membrane is deposited on a glass wafer with a layer of photoresist spun on it as the sacrificial layer [107]. The glass wafer serves as a carrier wafer and allows straightforward alignment of the patterned elements with the cavity backed trenches on the top wafer during the membrane transfer process. In the membrane transfer process, the membrane layer is released from the carrier wafer by removing the sacrificial layer. This is done by creating cuts in Parylene around the circumference of the wafer and soaking it in acetone and next IPA solutions for over 48 hours to allow the solutions to completely dissolve the photoresist through the cuts.

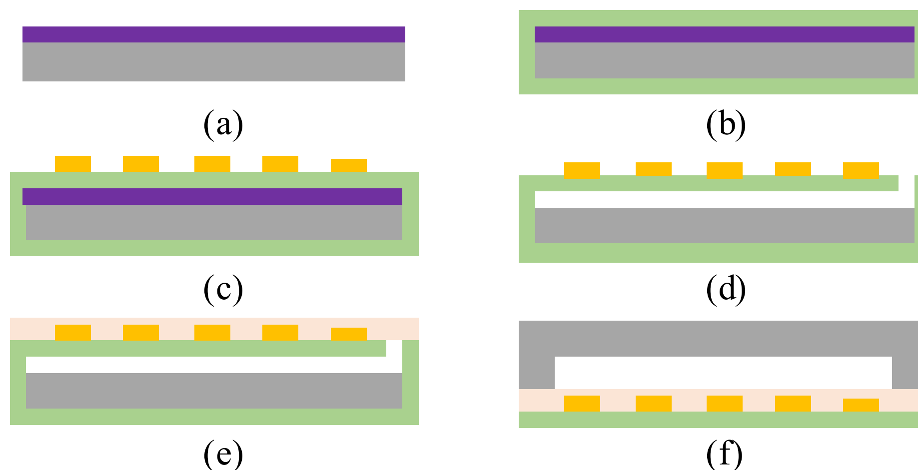

Figure 5.8. Diagram of microfabrication steps for realization and attachment of the patch array elements to the bonded bottom and top wafers. (a) Photoresist sacrificial layer spun on a carrier glass wafer, (b) 5 μm of Parylene deposited on the wafer as the membrane layer, (c) 0.5 μm of gold evaporated and patterned on the carrier wafer to form the patch array elements, (d) photoresist sacrificial layer dissolved and removed to release the membrane layer, (e) 1 μm of adhesive spun on the sample using, and (f) membrane aligned and attached to the bonded bottom and top wafers, and the carrier wafer detached.

The last step in the membrane transfer process is to align and attach the released membrane layer to the bonded top and bottom wafers. The choice of the bonding method is flexible since we do not need a high quality adhesion. One method to perform the boding is to deposit Parylene on the top wafer and to use Parylene to Parylene bonding process to transfer the membrane [108]. This method, however, is more suitable for smaller bonding areas and does not yield a uniform bonding across the entire patch arrays. Another approach is to use standard adhesives used in the clean room environment to attach the membrane to the top wafer. SU-8 and Crystalbond are some of widely used adhesives in the clean room but they are most suitable for non-aligned bonding of membranes. This is mainly due the fact that the built-in stress in these adhesives results in contraction of the membrane layer over time and result into non-aligned transfers. To overcome this problem, a low-stress photo-curable industrial adhesive is used to attach the membrane to the

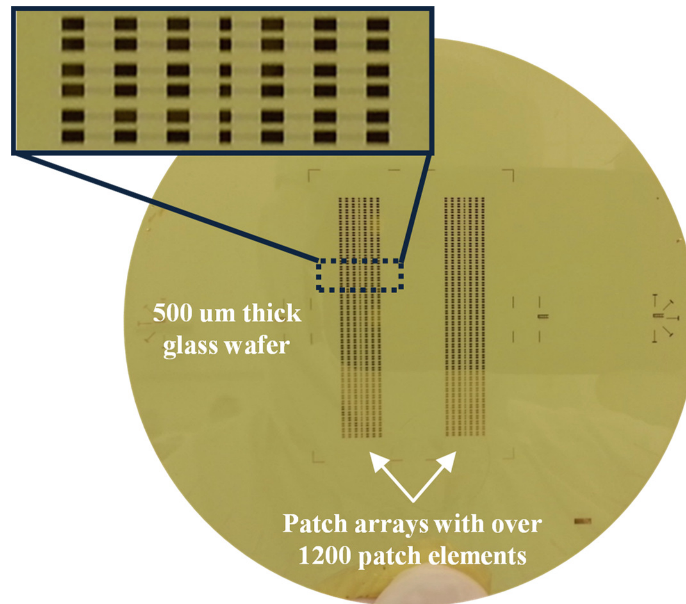

(a)

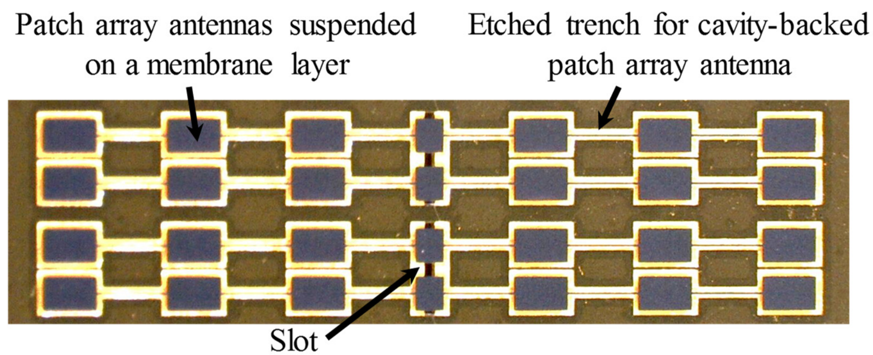

(b)

Figure 5.9. (a) Patterned patch array on the Parylene membrane layer deposited on a glass wafer before releasing, and (b) Patterned patch arrays for the vertically-polarized antenna are patterned are transferred to the bonded wafers using low stress adhesive (Dymax 4-20418),

bonded wafers (Dymax 4-20418) [109]. Dymax 4-20418 is a liquid based adhesive which can be spun on the wafer with thicknesses less than 1 μm and is next photo cured to permanently form the bond. Figure 5.9 illustrates a micrograph of the bonded membrane with satisfactory alignment resolution all across the antenna.

5.5. Side-Wall Smoothing

The radiation efficiency of the antenna and the connecting lines and transitions is primarily defined by the loss in the waveguide, which is a function of the profile of the etched waveguide trench as well as the quality of the metallization. In order to ensure uniform metallization of the etched waveguide and to minimize the waveguide loss, the etching process needs to be optimized to minimize the roughness on the sidewalls and bottom side of the trench. A scanning electron microscope (SEM) image of the etched waveguide trench is shown in Figure 5.10, revealing etching roughness formed on bottom and side walls of the waveguide. The image also shows formation of dense pillars at the corners and the edges of the waveguide trench, referred to as the grassing effect. There are two main reasons contributing to this roughness, namely, (a) accumulation of the passivation layer residuals deposited on the vertical walls at the corners and edges of the trench, (b) deposited residuals on the wafer at each etching step in the multi-step etching process. Extra physical and chemical cleaning processes are applied to the bottom wafer after each etching step to ensure complete removal of the deposited residuals. This includes

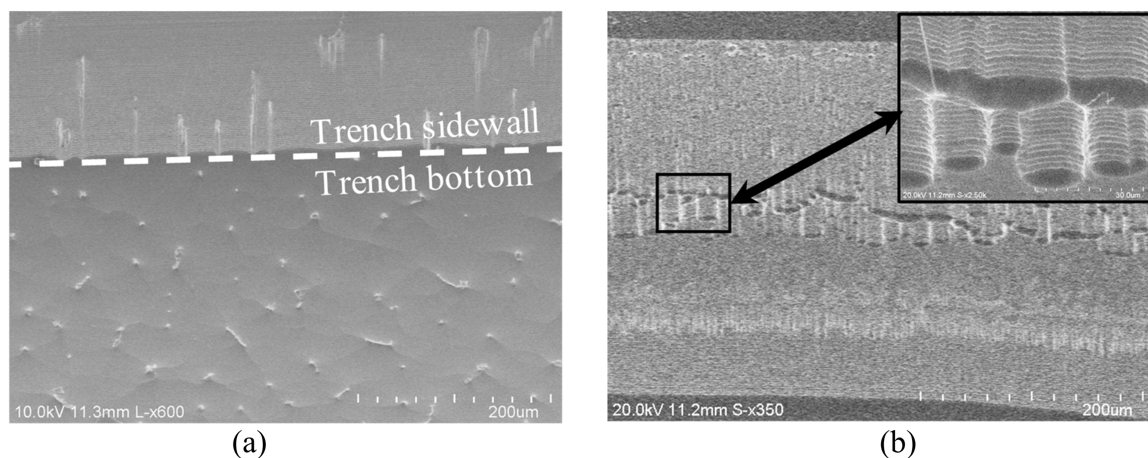

Figure 5.10. (a) SEM of the etched trench showing (a) roughness and grassing effects at the bottom and edges of an etched waveguide trench, and (b) sidewall roughness and scalloping effect formed on a three-stepped etched waveguide.

chemical cleaning of the sample in the Piranha solution [1:1 mixture of sulfuric acid (H_2SO_4) and hydrogen peroxide (H_2O_2)] for complete removal of all organic materials from the surface of the silicon wafer. An oxygen plasma treatment is also applied to the sample, right before each etching, to physically remove other deposited contaminations from the surface.

The role of the passivation layer in the DRIE process is to create a directional etch by preserving the side walls of the trench from the ion bombardment in the Bosch etching process. For deep long etches, such as the one presented in this work, this passivation layer gradually forms a polymer layer that is not completely etched away. This in turn creates a secondary mask layer for the subsequent etching step, specifically at edges and corners, and protects them from etching resulting in grass formation, as shown in Figure 5.11 (a). To mitigate the grassing effect in the multi-step waveguide trench structure, we have optimized the DRIE etching process. This includes increasing the ratio of the etching step to passivation step in each DRIE etching cycle, where the extended etching step results in further etching of the polymer passivation layer from the corners. Additionally, the temperature of the chuck in the DRIE recipe is increased (~40˚C) for a more

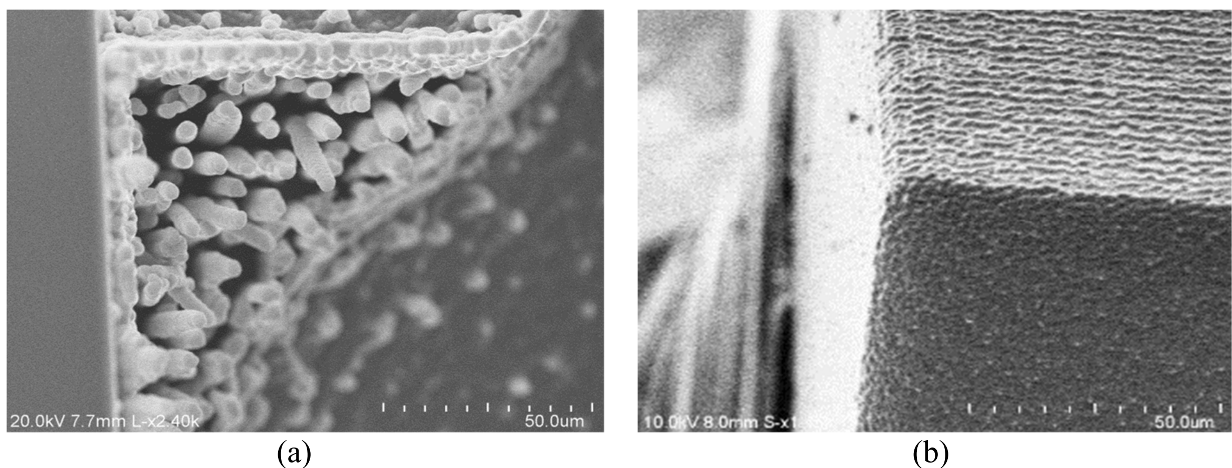

(a) (b)

Figure 5.11. (a) SEM of a corner of the etched waveguide trench showing grassing effects formed at the corners of the trench, and (b) SEM of the waveguide trench corner etched with the modified DRIE recipe.

Table 5.1. Optimized DRIE Silicon Etching Recipe Parameters

Parameter	Passivation Deposition	Etch
Pressure	25 mTorr	100 mTorr
C_4F_8 Flow	200 sccm	0 sccm
SF_6 Flow	0 sccm	450 sccm
O2 Flow	0 sccm	45 sccm
Time	4 s	8.5 s
Etch rate	-	14 μm/min
Undercut	-	2 μm
Scallop height	-	2 μm
Scallop depth	-	1 μm
Sidewall angle	-	89.1°

aggressive and directional etch. The combination of these two techniques allows deep grass-free etches, as shown in Figure 5.11 (b). Table 5.1 summarizes the recipe parameters of the modified DRIE etching process.

In addition to the smoothness of the bottom and edges of the waveguide trench, the smoothness of the trench sidewalls is also of critical importance. This is specifically the case as in the DRIE process a scalloping effect occurs on the sidewalls, as a result of consecutive passivation and etching steps, resulting in sidewall roughnesses that makes metallization coverage on the sidewalls challenging. Additionally, in deep multi-step etchings the residuals of each mask layer at the surface of the wafer along the waveguide sidewalls, forms a secondary mask for the next etch which results into additional sidewall roughness in the next etch [Figure 5.12 (a)]. To smoothen the sidewall of the trench, a technique based on isotropic etch of the waveguide trench is developed. In this method, the waveguide trench is isotopically etched by exposing the sample to Xenon Difluoride (XeF_2) for a short (~60-120s) etch. Since the scallop peaks have more exposure to the etchant gas, the peaks get further etched compared to the scallop's valleys, and hence the sidewalls become smoother. The summary of the XeF_2 etching recipe is presented in Table 5.2. Prior to the etch, the surface of the silicon is cleaned from the passivation layer deposited

in the DRIE process as well as the inherent silicon dioxide (SiO_2) formed on the surface of the

Table 5.2. Summary of the XeF_2 etching recipe parameters for smoothening the sidewalls of the etched trenches.

Parameter	**Etch**
XeF_2 Pressure	3 Torr
N_2 Pressure	0 Torr
Etch rate	0.1 um/cycle
Number of cycles	3-6

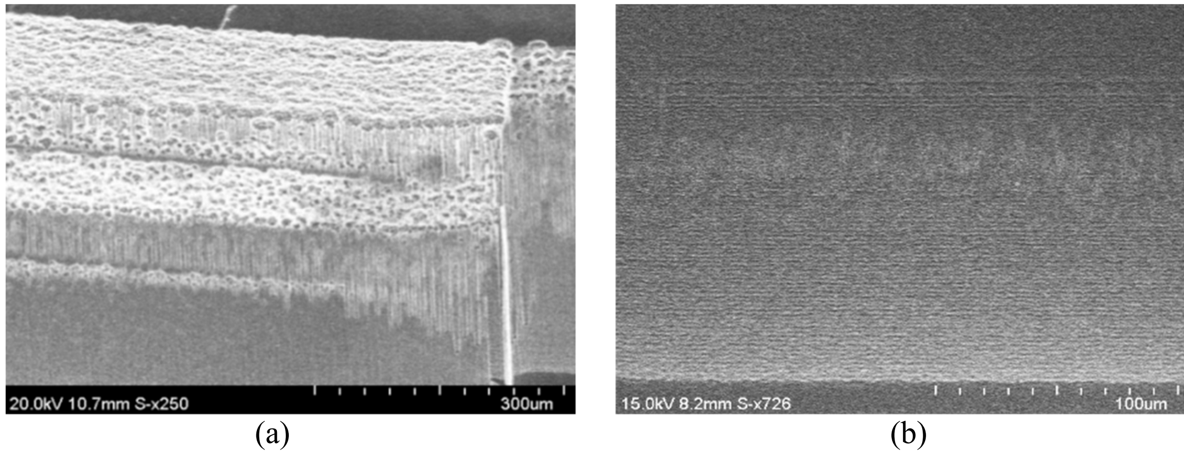

Figure 5.12. (a) SEM of the sidewall of the waveguide trench after multi-step DRIE etching showing sidewall roughnesses, and (b) sidewall of the multi-step etched waveguide trench after applying the smoothening technique.

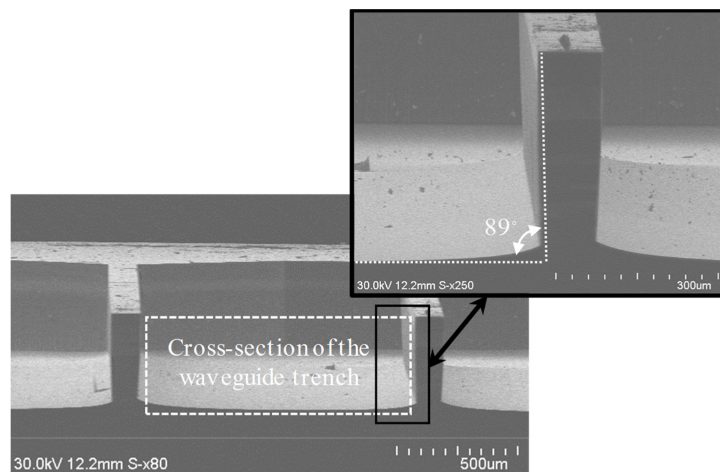

Figure 5.13. SEM of the cross-section of a diced waveguide showing the DRIE etch profile of the deep trench. The sidewalls have a slope of about 89° with an undercut of approximately 2 μm.

silicon, by soaking the sample in Hydrofluoric Acid (HF) for 10 min. Figure 5.12 (b) shows the SEM image of the waveguide trench after smoothening the walls.

As the final note on microfabrication of the bottom wafer, for the deep etch such as the one presented in this work, the etching process creates a sidewall angle (~89°) and an undercut (~2 μm) (as shown in Figure 5.13) which in effect increases the width of the waveguide. This in turn changes the propagation constant of the travelling-wave meandered waveguide and changes the inter-element phase shift in the antenna array, and hence a shift in the direction of the antenna beam. To overcome this issue, the waveguide widening is simply compensated for by narrowing the waveguide width in the patterning process.

5.6. RF Front-End Prototype

The completed prototype of the radar RF front-end components, including the co- and cross-polarized antennas as well as the chip package along with the waveguide probe to on-wafer waveguide transitions are presented in the section. Figure 5.14 shows the complete vertically and horizontally polarized beam-steering patch array antenna. The prototype shown consists of two side-by-side micro-antennas, with a total of over 1200 and 900 patch elements in the co- and cross-pol antennas, respectively. The micro-machined transceiver antenna structures shown has a total size of 4.5 cm by 3.5 cm by 1.25 mm and weighs only 4.4 g (2.2 g per antenna).

The microfabrication of the chip package is performed using the described process and a close up of the package is shown in Figure 5.15. The package consists of a socket for mounting the MMIC [as shown in Figure 5.15 (a)] along with RF lines and transitions with plated pillars [as shown in Figure 5.15 (b) and (c)] patterned on a membrane layer.

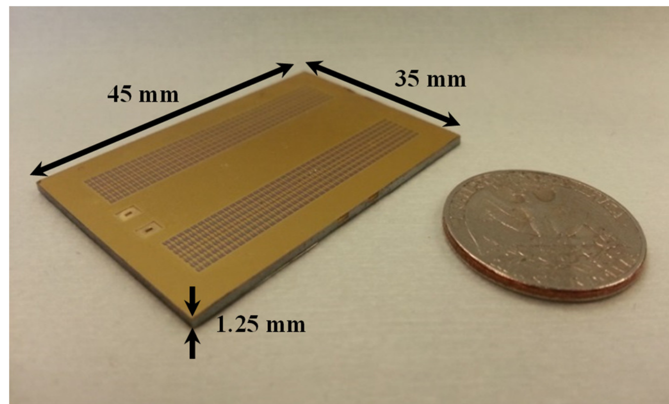

(a)

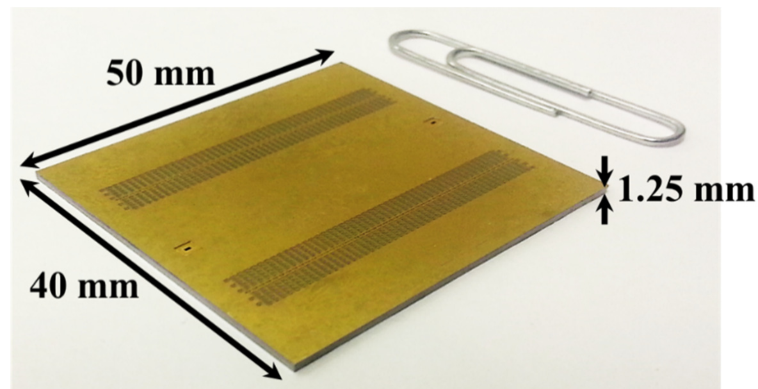

(b)

Figure 5.14. Close-up of the micromachined frequency scanning beam-steering antenna at 240 GHz. (a) Vertically-polarized Tx/Rx set with over 1200 radiation elements and weighs only 4.4 g, and (b) Horizontally-polarized antenna set with 900 patch antenna elements.

5.7. Summary

The microfabrication steps for realization of the components for the proposed MMW radar are discussed in this chapter. Fabrication of the components is performed using three layers. DRIE techniques are used to create multistep structures on the bottom silicon wafer. A novel multistep etching process using glass-in-silicon reflow technique is utilized to enhance the sidewall profile quality. The membrane-supported features are realized on the top silicon substrate. The two

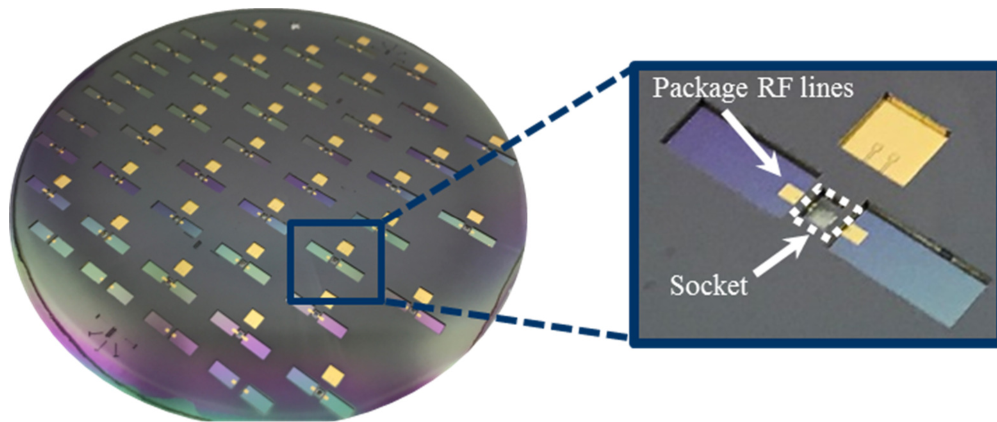

(a)

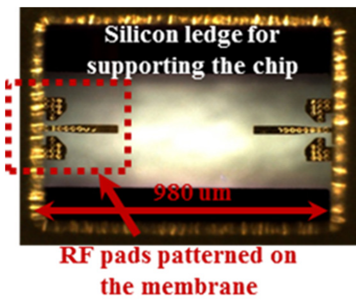

(b)

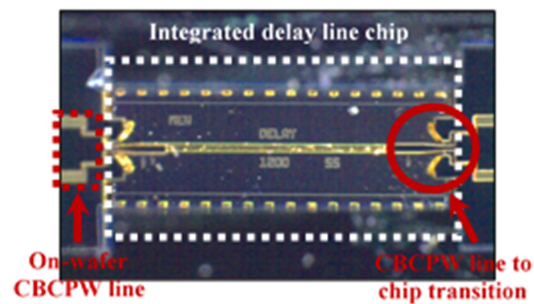

(c)

Figure 5.15. Close-up of the micromachined chip package with incorporated RF-choke and the bias network for integration of active and passive MMIC, (b) bottom-view of the package before insertion of the MMIC, showing the RF pads and the associated transitions, and (c) top view of the package with an integrated through-line MMIC.

substrates are ultimately bonded to form the complete structures. The characterization of the fabricated structures is described in the next chapter.

CHAPTER 6
MEASUREMENT TECHNIQUES

In this chapter, the developed measurement methods for sub-MMW characterization of the micromachined components and sub-systems are presented. Reliable and repeatable characterization of devices and components at high MMW and sub-MMW frequencies is often very challenging. This is partly due to the complexity of the measurement setup and tight constraints on alignment and quality of interconnections between the probes, device under test (DUT), and the measurements setup. Additionally, the low level of available output power of sources at these frequencies combined with the high losses in the measurement setup, which includes transmission lines, connectors, and probes, and lack of flexibility of such components are among other challenges that are encountered. In order to overcome these challenges and to enable reliable and repeatable on-wafer characterizations, novel measurement techniques are developed and presented in this chapter. Section 6.1 presents an overview of the measurement setup and the conventional measurement methods and their limitations at high frequencies. In Section 6.1, the overview of on-wafer MMW measurements and their challenges is discussed. Section 6.2 presents a novel waveguide probe measurement technique for on-wafer S-parameter measurements, which is utilized for on-wafer characterization of waveguide-based components including the antennas and the chip package for the radar RF front-end. In order to characterize the micromachined antennas, an on-wafer near-field pattern and gain measurement methods are also developed and

presented in Section 6.3 and 6.4, respectively, and the measurement results of the antennas are discussed. Finally, Section 6.5 presents the measurement of the chip packaging method.

6.1. On-wafer S-Parameter Measurement

6.1.1. S-Parameter Measurement Setup

The operation frequency of commercially available network analyzers is limited to the lower portion of MMW frequencies (up to W-band). Therefore, to extend the frequency range of measurements to high MMW and sub-MMW frequencies, frequency extender units are often used along with network analyzers to enable measurements up to THz frequencies. In this work, a WR-3 measurement setup is utilized for S-parameter measurements, as shown in Figure 6.1. The setup consists of:

1. Agilent PNA-X N5245A network analyzer
2. WR-3 OML frequency extending modules
3. Appropriate probes including WR-3 probes as well as GGB 220-325 GHz Ground-Signal-Ground (GSG) probes
4. Cascade probe station and micropositioners
5. Aerotech high resolution XY stage with 100 nm precision in positioning
6. Leica stereomicroscope

6.1.2. Conventional On-wafer Measurement Methods

As discussed earlier, measurement of *S*-parameters of micromachined components at high MMW frequencies is not straightforward. This becomes specifically challenging for on-wafer measurements as the performance of conventional probes deteriorates. At lower frequencies (up to G-band), coaxial and Coplanar Waveguide (CPW) line Ground-Signal-Ground (GSG) probes

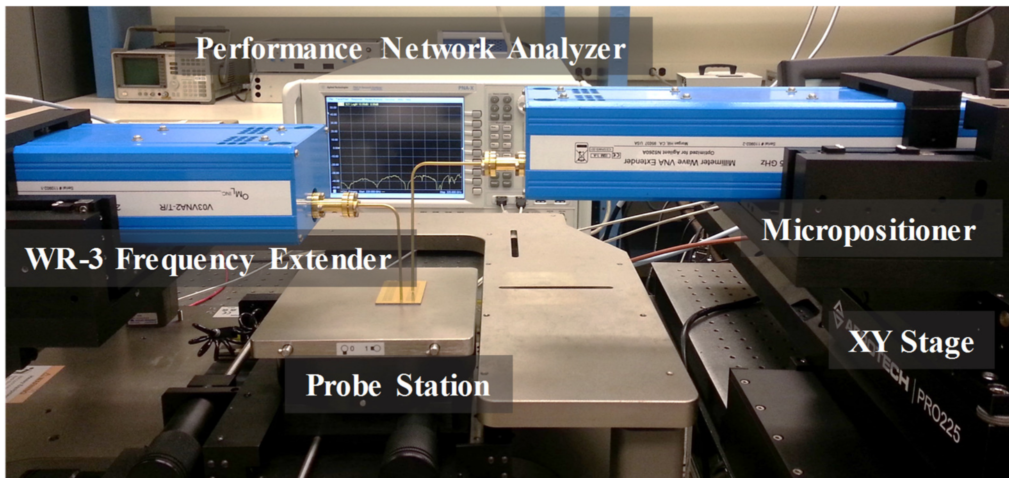

Figure 6.1. Photograph of the WR-3 measurement setup.

are commonly used for on-wafer S-parameter measurements [110], [111], as shown in Figure 6.2. However, at frequencies above G-band the dimensions of the coaxial lines and the probe tips become too small to be mechanically stable. Larger size coaxial probes and probe tips lead to excitation of higher order modes in the line and radiation from the probe tips. Also the parasitics from the probe tips and the pads on the wafer lead to unreliable and non-repeatable measurements.

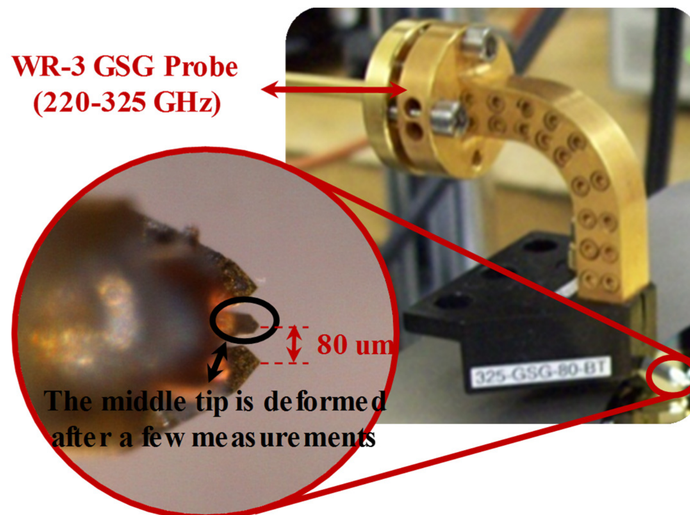

Figure 6.2. Photograph of a WR-3 GSG probe. The fragile tip of the probe makes repeatable and reliable measurements challenging, specifically because of the mechanical instability after a few measurements.

Other measurement approaches have been also reported in the literature [112]-[115]. Although good performances have been reported, most of these approaches require complex structures and involve assembly of multiple parts with high level of accuracy.

6.2. Proposed Non-Contact On-wafer Waveguide Measurement Method

To overcome the problems associated with conventional methods and to be able to directly interface with micromachined waveguide components, an alternative approach based on using open-ended waveguide probes together with probe to on-wafer waveguide transition is investigated and the performance of the measurement technique is demonstrated at WR3 band. Figure 6.3 shows a schematic of the proposed measurement approach. It consists of a network

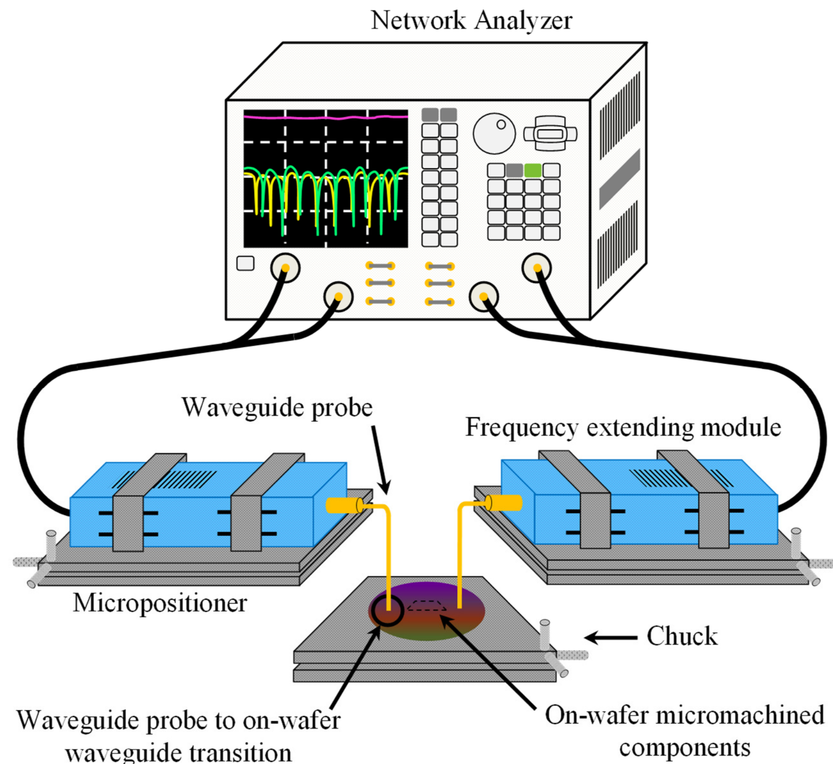

Figure 6.3. Conceptual illustration of the proposed measurement approach showing the open-ended waveguide probes coupling the electromagnetic power to on-wafer waveguide components through proper micromachined transitions.

analyzer, two frequency extending modules and two open-ended waveguide probes connected to the waveguide ports of the modules. The open ends of the probes effectively couple the electromagnetic power to on-wafer waveguide components through special waveguide transitions. The proposed transition is designed to be compatible with silicon micromachining technology and does not require assembly of multiple parts. Additionally, the waveguide probe and the transition are all rigid and immune to probe deformations resulting from wear and tear. In fact, the open-ended waveguide probe to the on-wafer waveguide transition can be non-contact. To facilitate this non-contact (imperfect contact) transition, an RF choke on the metallic wall of the waveguide cross section of the probe is created using electric discharge machining as further discussed. Another novelty pertains to a method for positioning the waveguide probe over the transition opening with a lateral alignment accuracy of better than 10 μm.

6.2.1. Transition Design

Our proposed method for measurement of the *S*-parameters of on-wafer waveguide components is based on connecting special open-ended waveguide probes, which are connected to the two ports of frequency extenders of a network analyzer, to on-wafer micromachined waveguides through an E-plane bend transitions. Here due to limitation of microfabrication process, a stepped transition compatible with fabrication process of the rest of the radar front-end is considered, as shown Figure 6.4. The width of the micromachined waveguide inside the lower silicon wafer can also easily be changed to a desired width depending on the band of operation and the requirement on the loss. The width tapered transition can easily be facilitated by micromachining. The number of steps, their widths and heights are calculated using a full-wave solver through an optimization process for maximum power coupling. The waveguide top is covered by a second silicon wafer patterned by a thin dielectric membrane and metalized on one

side. This wafer is attached to the lower wafer using gold-to-gold thermo-compression bonding which will be described later. To align the opening of the waveguide probe with that of the on-wafer waveguide, a rectangular window with dimensions slightly larger than those of the outer

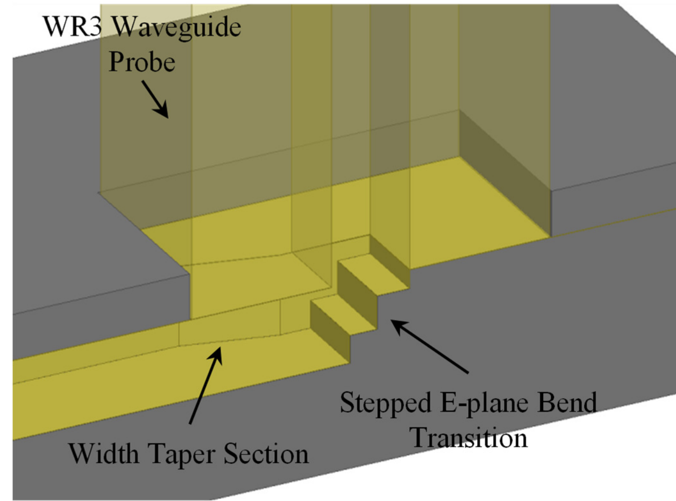

(a)

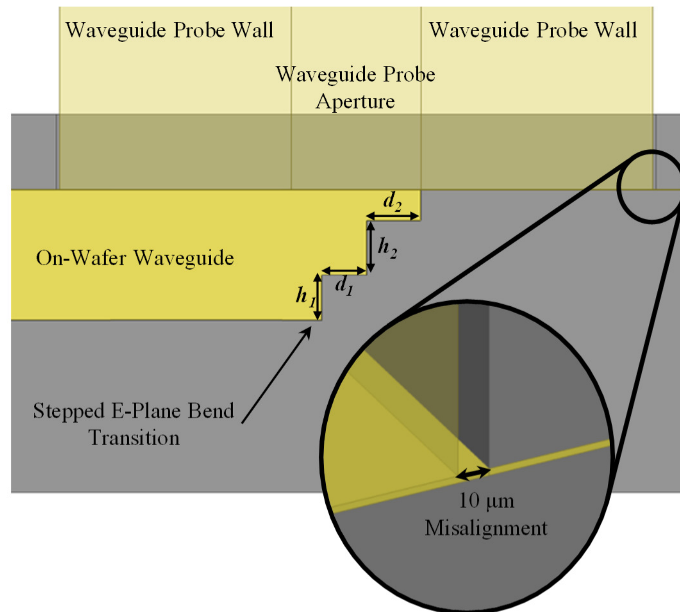

(b)

Figure 6.4. Schematic of the micromachined waveguide probe to on-wafer waveguide transition (a) 3-D view of half of the structure showing the waveguide probe in contact with stepped E-plane bend transition, (b) Side view of the structure showing an alignment accuracy of 10 μm. Optimized dimensions: d_1=184 μm, h_1=118 μm, d_2=109 μm, h_2=182 μm.

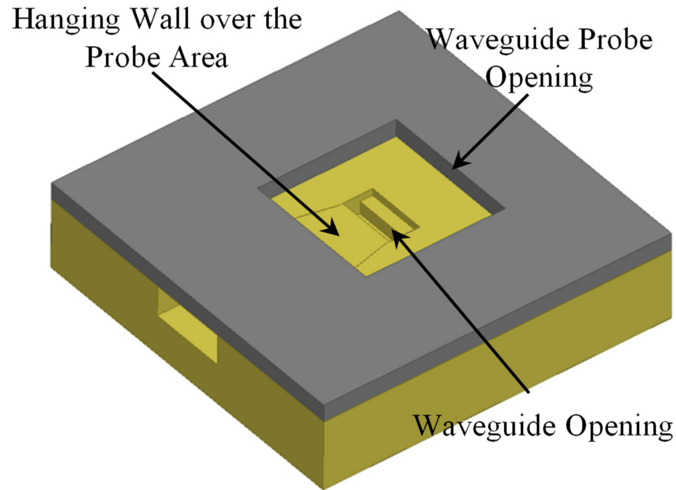

Figure 6.5. Diagram showing the probe opening on the top wafer for accurate alignment of the probe with the waveguide opening.

dimensions of the waveguide probe is micromachined on the top wafer. The open-ended waveguide probe can be inserted in the window (Figure 6.5) allowing alignment resolution of less than 10 μm (2% of waveguides dimensions). It should be mentioned that the membrane gold has rectangular opening exactly the same size as that of the open-ended probe. The dielectric membrane maintains the current distribution over the top wall of the waveguide and a minimum gap between the waveguide probe and the surface of the on-wafer waveguide at the transition point.

Full-wave analysis of the proposed structure was performed in a commercial Finite Element Method solver (Ansoft HFSS). Figure 6.6 shows the simulation results of the optimized WR-3 two-step transition. The metal loss is not included in this simulation and it is assumed that the waveguide probe and the on-wafer waveguide are physically connected with no misalignments. The result shows that the transition has a reflection loss of more than 30 dB with an insertion loss of less than 0.01 dB over the entire WR-3 band (220-325 GHz).

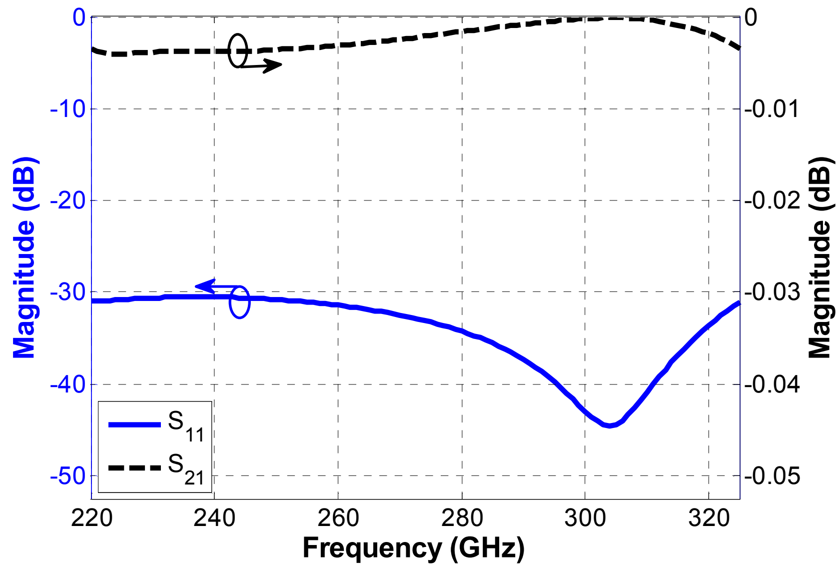

Figure 6.6. Full-wave simulation results of the optimized two-step transition from the WR3 waveguide probe to on-wafer WR3 waveguide. Optimized dimensions: d_1=184 μm, h_1=118 μm, d_2=109 μm, h_2=182 μm.

6.2.2. Waveguide Choke Design

When a waveguide is cut by machine tools, the surface of the cut area becomes rough with a roughness on the order of few micrometers and the cross section may not be exactly perpendicular to the waveguide axis. As a result, a good contact between the waveguide probe and the waveguide opening cannot be established. Also as mentioned before, a thin dielectric membrane also exists between the waveguide probe and the top of the on-wafer waveguide transition. This imperfection can result in high reflection and radiation loss through the gap. The uncertainty about the gap formation between the probe and the transition will adversely affect the measurement repeatability as well.

To circumvent these difficulties, the standard approach is to make a waveguide choke. A waveguide choke presents a very low series impedance at the junction independent of the gap value around the junction edge. However, the difficulty at sub-MMW band is the fabrication of

the choke itself due to its small dimensions. At these frequencies the waveguide walls are thick enough to support the choke structure. The geometry and the parameters of the choke are shown in Figure 6.7. The design includes a circular stub with the depth of approximately quarter-wavelength connected to a recessed circular disc around the waveguide opening. Full wave analysis of the probe coupling to the on-wafer waveguide is performed for different gaps between the probe cross section and the wafer surface. As shown in Figure 6.8, the insertion loss for an 80 μm gap between the surfaces is more than 1 dB for probe without the choke and it reduces to less than 0.2 dB for the probe with the choke. This shows that the presence of the choke reduces the

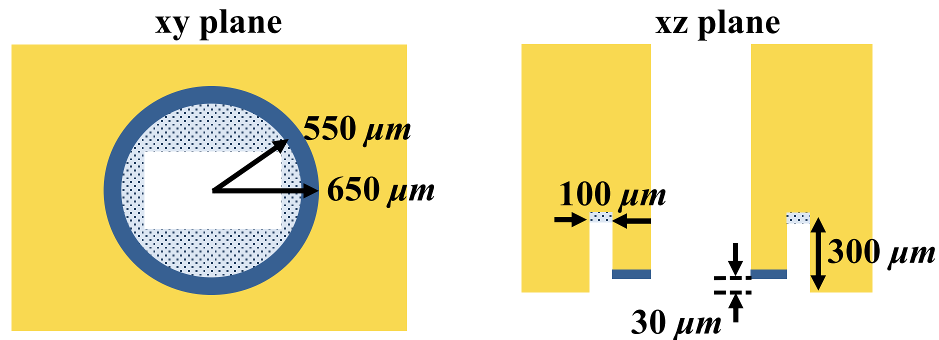

Figure 6.7. Diagram of the optimized choke design.

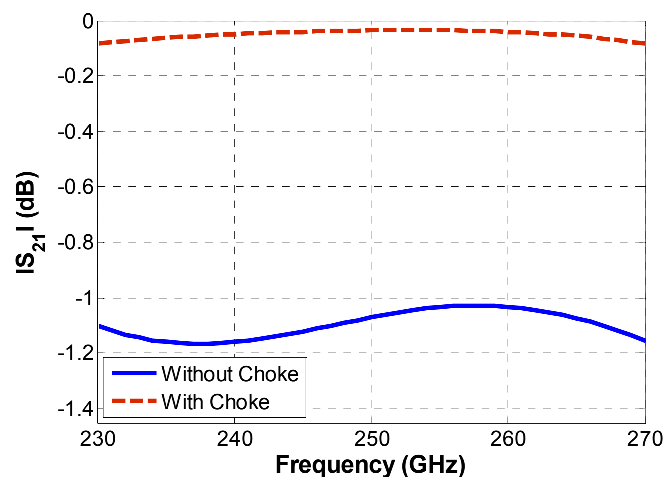

Figure 6.8. Full-wave simulation results of the effect of the choke on the performance of the measurements.

sensitivity of the measurements to the contact quality significantly. The design parameters are optimized to minimize the return loss in the desired band (230-270 GHz).

Grooves are milled using an Electrical Discharge Machining (EDM) technique to fabricate the choke with a high level of accuracy. The fabricated choke is shown in Figure 6.9. The choke dimensions can also be optimized for best full-band (220-325 GHz) performance. Figure 6.10

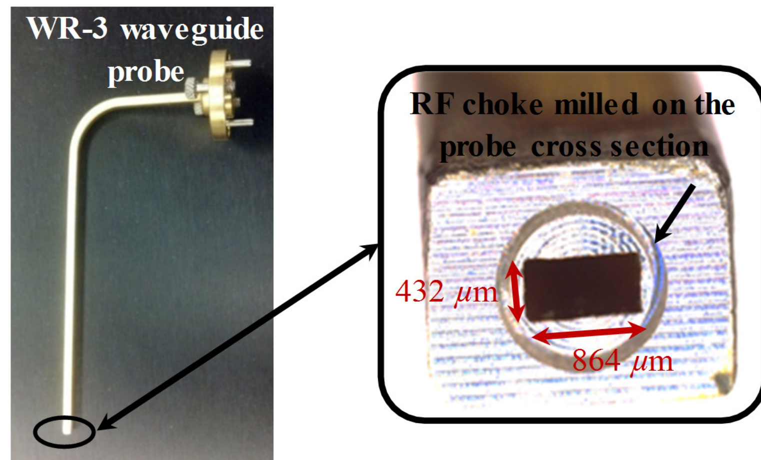

Figure 6.9. Choke milled on the cross-section of waveguide probe using the EDM technique.

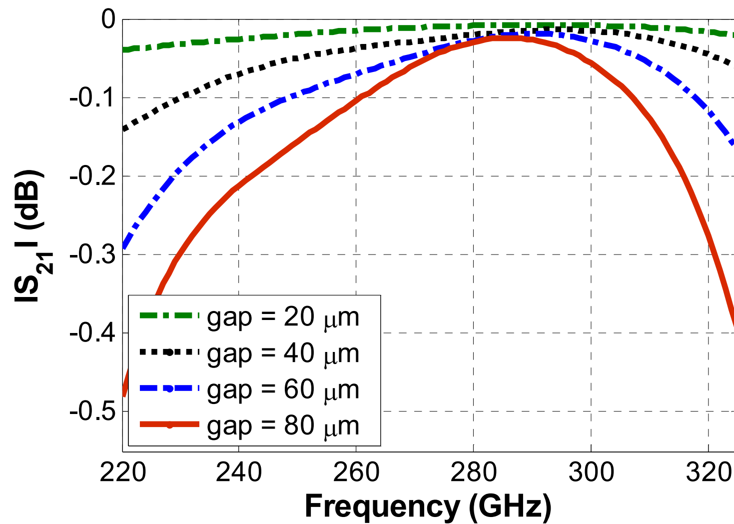

Figure 6.10. Full-wave simulation results of the optimized full-band choke design for different values of gap between the probe cross section and the surface of the wafer.

shows the coupling performance from the probe with a full-band choke to the on-wafer waveguide for different gaps between the probe cross section and the wafer surface.

6.2.3. Waveguide Probe Sensitivity Analysis

Perfect alignment of the waveguide probe with the waveguide opening is very challenging and without a reliable method it can be the major error source in measurements. In our approach, the provision of an opening on the top wafer restricts the possible sources of misalignment (rotation and lateral displacement) significantly. As mentioned earlier, this window limits the probe positioning error to a maximum of 10 μm. In addition to the measurement errors, the micromachining of the transition with multiple fabrication steps is prone to some errors. Errors caused by DRIE etching and small misalignments between the top and bottom wafers can degrade the performance of the transition to some extent. DRIE etch of the steps with the exact height over a large area is rather difficult if not impossible. The position of the sample inside the etching chamber, the temperature of the chamber, the depth of etch, etc. vary the etch rate from one etch to another. For the proposed transition fabrication, a maximum error of 20 μm can be encountered.

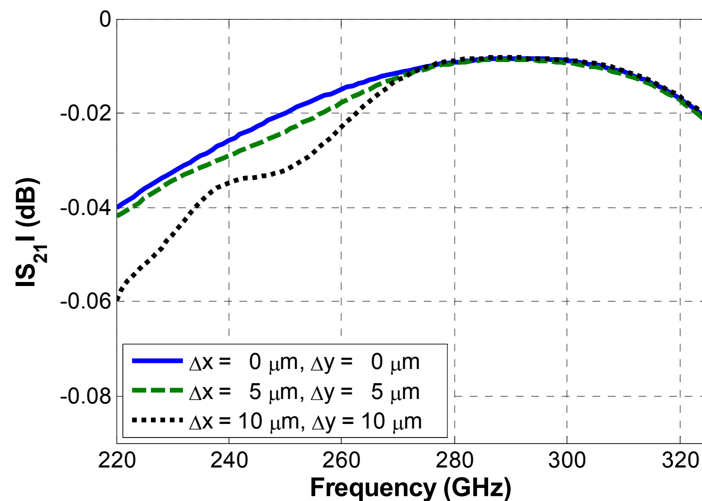

Figure 6.11. Transmission coefficient of the transition for different misalignments of the waveguide probe with the on-wafer waveguide opening.

To investigate the effects of probe positioning and microfabrication errors on the performance of the transition, full-wave simulations are carried out. Figure 6.11 illustrates how minor probe misalignments affect the performance of the transition. Figure 6.12 represents how step height variations affect the insertion and reflection coefficients of the transition, showing maximum insertion loss of 0.2 dB for all possible height variations of the steps.

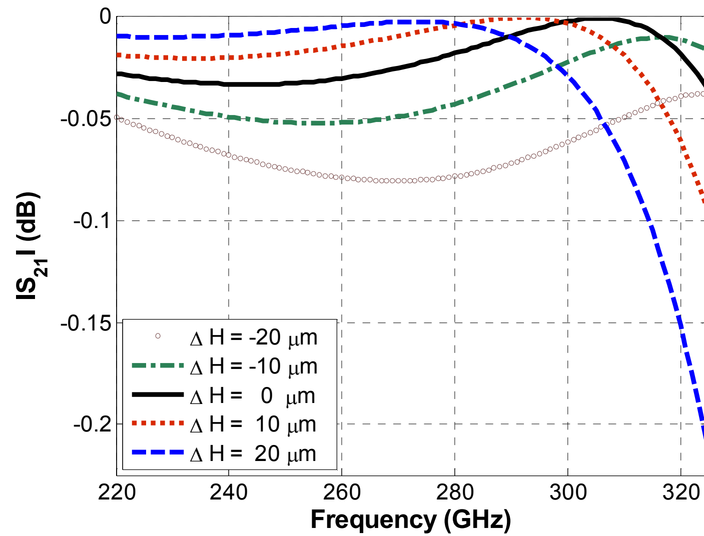

Figure 6.12. Variations in transmission coefficient of the transition with respect to height variations of the micromachined steps in the DRIE process.

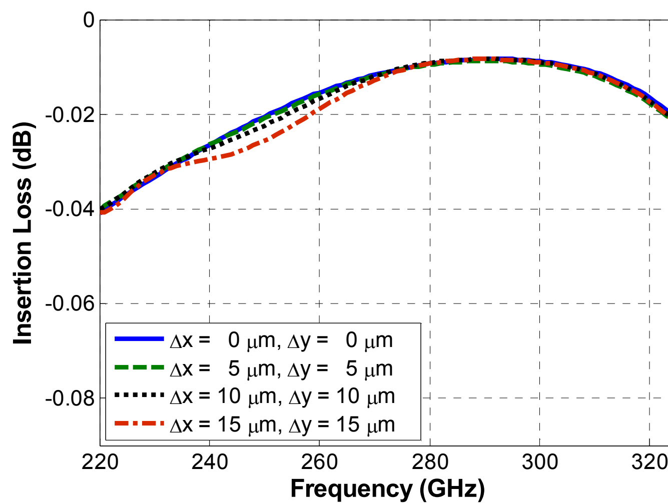

Figure 6.13 Transmission coefficient of the transition for different displacements between the centers of the milled choke and the waveguide.

Another source of error pertains to the milling of the choke on the waveguide probes. The EDM technique has a high precision tolerance of within 2 μm that has negligible effect on the choke performance. But the displacement between the centers of the milled choke and the waveguide can degenerate the performance of the choke in presence of a gap. Figure 6.13 shows the effect of this displacement in the performance of the transition, showing minimal deviation from the aligned milled choke.

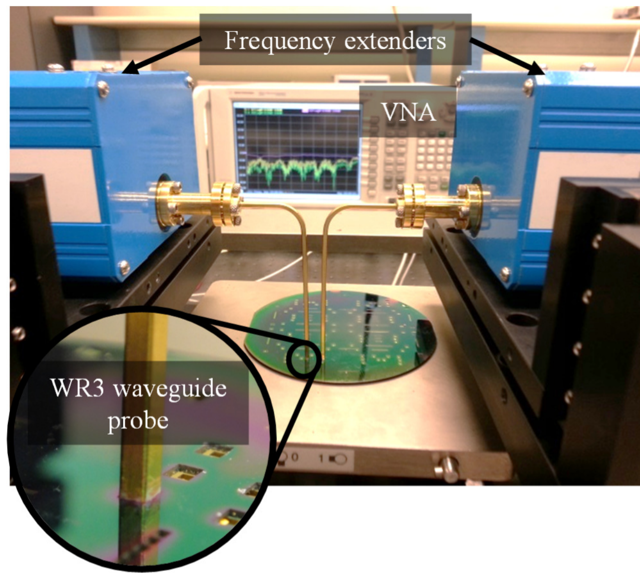

Figure 6.14. WR3 waveguide probe measurement setup.

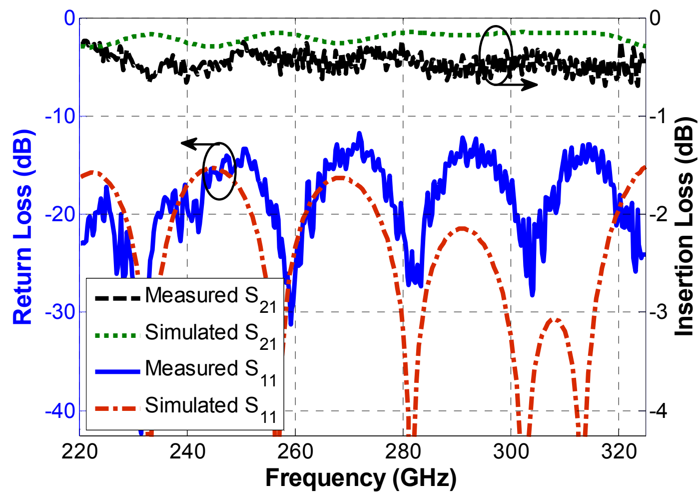

Figure 6.15. Simulated and measured S-parameter of an on-wafer back-to-back transition.

6.2.4. Waveguide Probe Measurements

The performance of the on-wafer E-bend stepped transition with probe alignment window and the waveguide probe with the RF choke is measured by the setup shown in Figure 6.14. An Agilent N5245 4-port network analyzer is used along with OML MMW frequency extending modules to perform full 2-port S-parameter measurement at WR-3. The two waveguide probes are connected to the output ports of the frequency extending modules from one end and connected to the openings of the on-wafer waveguides from the other end. The measurement setup is calibrated up to the output ports of the frequency extenders. Figure 6.15 illustrates the measured return loss and insertion loss of a back-to-back transition with a waveguide segment of 4.8 mm in between. For a fair evaluation of the transition, the insertion loss of the 10 cm long probes is removed from the measurements and the remainder is presented, representing the insertion loss of the back-to-back transition only. This is based on the assumption that the reflections from the connections of the probes to the modules and the on-wafer openings are negligible. The loss of the waveguide probes is estimated by short-circuiting the probes with a 1 μm gold coated wafer and measuring the reflection coefficient of the short-circuited probes. The results show that the back-to-back waveguide to on-wafer micro-machined transition has an insertion loss of less than 0.7 dB over the entire WR-3 band.

As shown in earlier, the misalignment of the probe with respect to the on-wafer waveguide opening as well as the gap between the probe and the wafer's surface will affect the performance of the measurements. To investigate the effect of these errors on uncertainty of the measurements, a repeatability test is carried out. In this test, 30 repeated measurements of the same back-to-back transition were taken over a 2 h span where in each measurement the probes were removed and then re-inserted into the openings after repositioning them. The transmission coefficients of the

measurements are illustrated in Figure 6.16 (a). For a clearer comparison of the measurements, the measured transmission coefficients are normalized to a single measurement and represented in Figure 6.16 (b), where it shows a repeatability error of less than 0.2 dB in the measurement of the transmission coefficient of a single back-to-back transition over the entire frequency range.

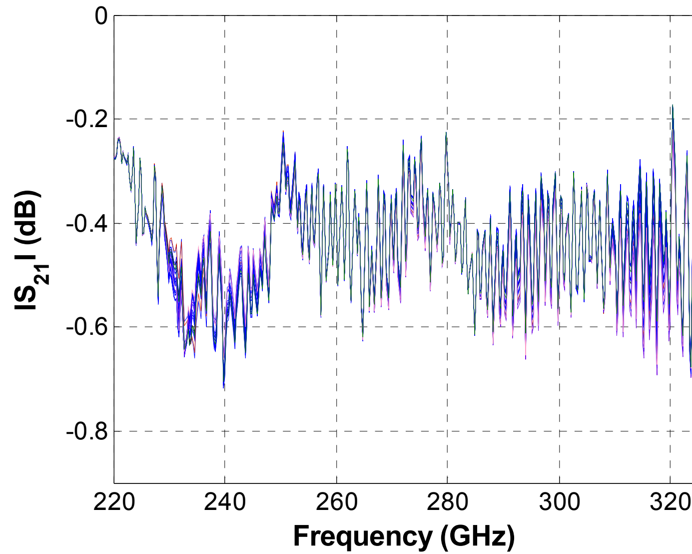

(a)

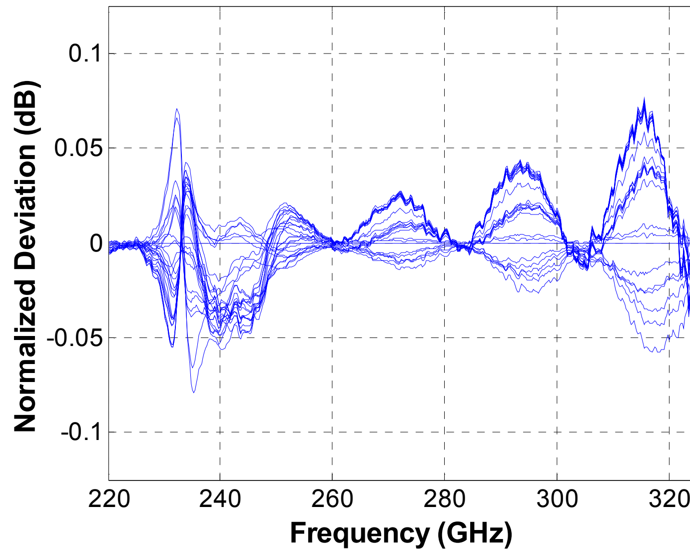

(b)

Figure 6.16. (a) Repeated transmission coefficient measurements of a single on-wafer back-to-back transition (N=30), (b) Transmission coefficient of the back-to-back transition for repeated measurements normalized to a reference measurement.

6.3. Antenna On-wafer 3D Pattern Measurement

There are two standard methods for measuring the radiation pattern of antennas: far-field and near-field measurement methods. Both of these methods are well established, but there are practical difficulties in their implementation at high frequencies. This is particularly the case for on-wafer antennas where the bulky sources attached to probe stations cannot be easily moved for far-field or even near-field measurements. In fact, most probe stations are mounted on optical tables as on-wafer probe measurements of circuits are very sensitive to vibrations. At microwave frequencies coaxial cables are usually used to connect antennas on turntables to stationary sources or receivers. Flexible coaxial cables allow for movement and rotation of the antenna under test (AUT). At MMW and sub-MMW bands where flexible transmission lines cannot be used, compact stable sources or receivers attached to the AUT must be mounted on positioners. Compact sources at such high frequencies are usually narrowband and can provide rather limited power levels. Also sensitive receivers with wide dynamic range are usually bulky. Powermeters or harmonic mixers in conjunction with spectrum analyzers can be used and provide wide bandwidth. Powermeter performance, however, is limited by relatively high input power level requirement (>-30 dBm) and low dynamic range (<40 dB). Harmonic mixers unfortunately have large conversion loss (>30-40 dB) which limits the spectrum analyzer's dynamic range. Considering the high free-space path-loss and the limited available power at these frequencies, the use of powermeters and harmonic mixers for antenna pattern measurements is quite limited to electrically small antennas with short far-field distances. Such a far-field measurement method for a small antenna is demonstrated in [116].

For near-field techniques the transmitter and receiver units [e.g. frequency extenders of a vector network analyzer (VNA)] are collocated and the far-field criterion need not be satisfied.

This allows for the use of coherent transceivers such as network analyzers that can provide wide frequency range of measurements with wide dynamic range and excellent accuracy. Another advantage at MMW and sub-MMW frequencies pertains to the fact that the physical extent of the probe movement over the antenna is rather small since the antenna's physical dimensions are quite small. This way the transmitter or receiver unit (frequency extender) attached to the probe can be moved with a small flexure requirement of connecting coaxial cables between the frequency extender and the VNA. Using appropriate probes, near-field technique also allows for on-wafer antenna measurements as is described next.

The desired test antenna has an aperture size of approximately 42 mm by 7 mm which is about 34λ by 6λ at the highest operational frequency, i.e. 245 GHz. To characterize such an electrically large antenna using the far-field technique, the far-field condition requires 2.8 m minimum separation distance between the AUT and the standard antenna which corresponds to a free-space path loss of 90 dB. Noting that measurement of sidelobes with gains much less 0 dBi are required, even using a sensitive VNA with frequency extenders (dynamic range<75 dB), accurate far-field measurement is not possible.

6.3.1. Proposed Near-Field Measurement Setup

To enable on-wafer characterization of antennas at sub-MMW frequencies, a near-field measurement setup is assembled. The proposed setup consists of an Agilent N5245 4-port PNA-X network analyzer connected to the ports of two OML frequency extenders. A diagram of the measurement setup is illustrated in Figure 6.17. To measure the electric field distribution in the near-field region of the AUT, two open-ended waveguide probes (one for E-plane measurements and another probe with 90˚ twist for H-plane measurements) for near-field scanning are used. The waveguide probes are then connected to the receiving port of the VNA frequency extender. The

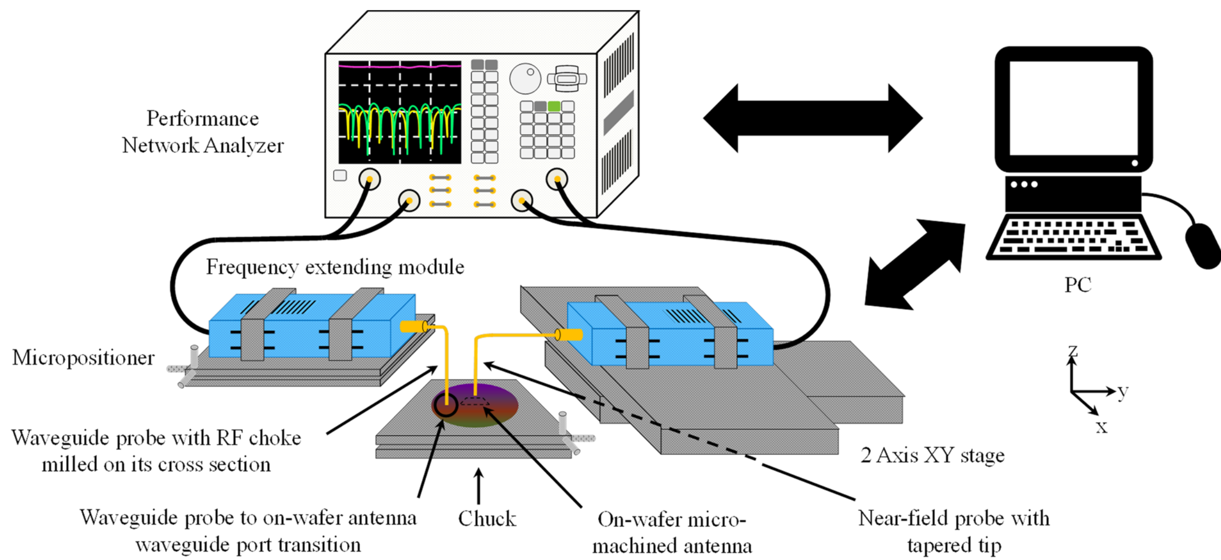

(a)

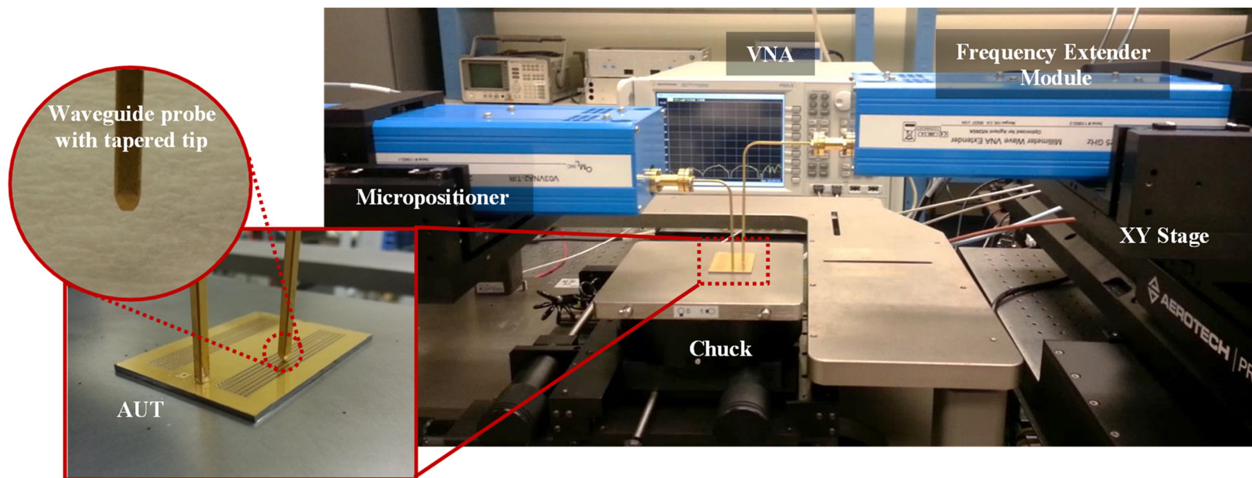

(b)

Figure 6.17. (a) Diagram of the proposed near-field measurement system for MMW, sub-MMW and THz on-wafer antenna characterizations, and (b) Photo of the proposed WR-3 band near-field measurement setup used for on-wafer characterization of the antenna array. Special waveguide probe with tapered tip is used for near-field measurement of the antenna under test. Another open-ended waveguide with on-wafer transition are devised to feed the waveguide port of the antenna.

thickness of the metal around the tip of the waveguide probes are tapered to minimize the field perturbation caused by the probe over the AUT. The receiving frequency extender is mounted on

an Aerotech high resolution XY stage with 100 nm precision in positioning. The frequency extender is connected with relatively long (about a meter) semi-rigid coaxial cable to the network analyzer to minimize phase variations as a result of small motions. In order to map the near-field of the AUT, planar scanning configuration is chosen and the stage is programmed to move the probe on rectangular grids with fixed sampling distances. To excite the waveguide port of the on-wafer silicon micromachined antenna, a waveguide probe along with the stepped transition is used, as discussed in Section 6.2.

Both the network analyzer and the XY-stage are controlled by an external computer to synchronize the near-field probe motion and data collection. A program is used to simultaneously instruct the micro-positioner to scan over the surface of the antenna and to measure and store the near-field data taken by the network analyzer. Once the near-field data is measured, a near-field to far-field transformation is performed to extract the radiation pattern of the antenna from the stored near-field data. One major advantage of the proposed measurement setup is that by exchanging the frequency extenders and the associated waveguide probes to other frequency bands, the same setup can be used to perform near-field antenna measurements over any band within MMW to terahertz (THz) frequency range.

6.3.2. Measurement Parameters

Spatial resolution, the extent of the scanned area and the probe distance from the antenna are critical parameters for an accurate near-field measurement [117]. According to the sampling theorem in order to fully reconstruct the signal from its discrete samples, a sampling resolution more than the Nyquist rate is needed. This requires a sampling spacing of smaller than $\lambda/2$, where λ represents the wavelength of the highest measured frequency, i.e. 245 GHz. For this measurement a spacing of Δ = 400 μm is chosen. As far as the scanned area is concerned, the

scanned area theoretically needs to extend to infinity for exact pattern measurements. However, in practice the measurements are truncated over a portion of the near-field of the AUT resulting in achieving a far-field pattern that is accurate up to a certain angle from the boresight. This angle is wider for larger scanned area. In these measurements, the extended margin beyond the aperture is chosen to be about 2.5 mm where the measured near-field signal level drops by 30 dB. The separation distance between the probe and the AUT is adjusted to be large enough to prevent significant coupling of their reactive fields and to ensure that the effects of multiple scattering between them are negligible. For a sampling spacing of 400 μm (~ $\lambda/3$) a separation distance of approximately 2.5 mm (~ 2λ) is chosen. It should be mentioned that a trade-off exists between the accuracy and the measurement time. In order to extend the dynamic range of the measurement setup, the IF bandwidth of the network analyzer is reduced to 100 Hz and an averaging factor of 4 is used. Using these parameters, it takes about 12 hours to measure the 2-D near-field of the antenna over the desired bandwidth of 15 GHz with frequency interval of 500 MHz.

6.3.3. Co-Polarized Antenna Measurement Results

Using the proposed measurement setup with the stated parameters, the near-field magnitude and phase of the tangential electric field of the beam-steering antenna is measured. As mentioned earlier, an open-ended waveguide probe with tapered tip is used to measure the AUT field distribution. The provision of the tapered tip minimizes the effect of multiple scattering between the near-field probe and the AUT and therefore the perturbation of the primary fields generated by the AUT is made as small as possible. Additionally, the use of probe with small tip results in a wide radiation pattern which is required for scanning a large area. Although the effect of the probe on the measured data is minimal, for accurate pattern reconstruction the effect of

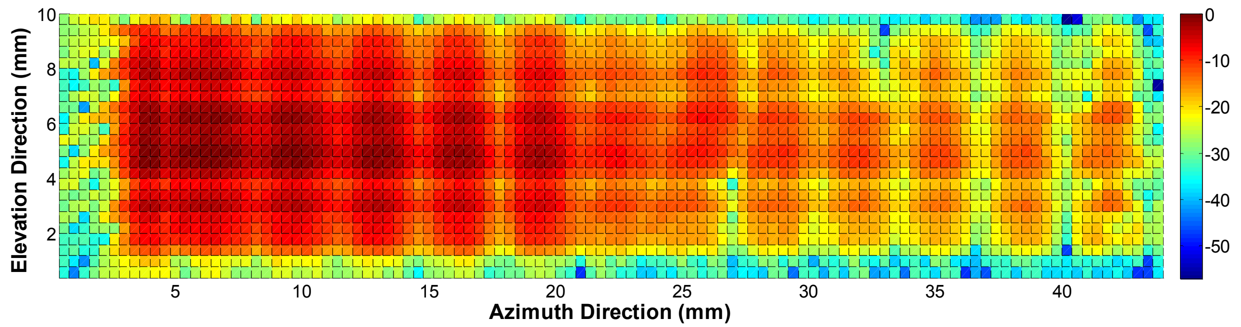

(a)

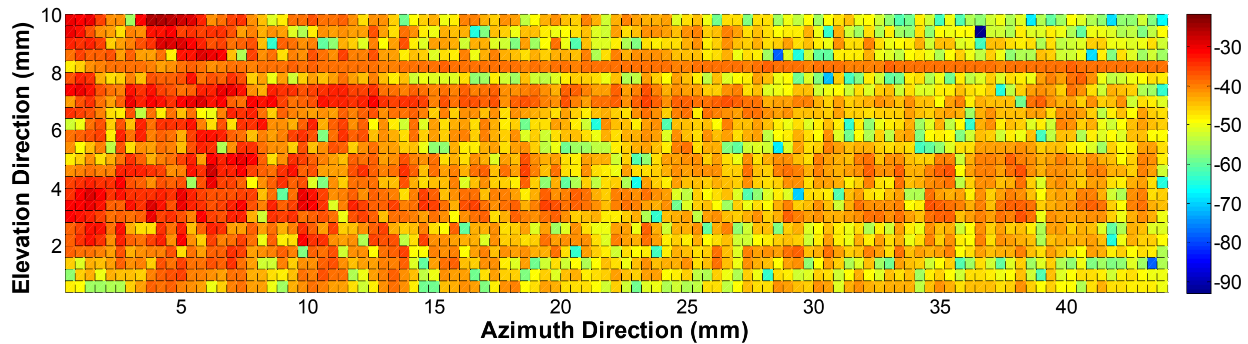

(b)

Figure 6.18. Measured normalized field intensity distribution at the center frequency over the area of the beam-steering antenna in the (a) co-polarized orientation, and (b) cross-polarized orientation with the measurements normalized to the co-polarized measurements.

radiation characteristics of the probe is taken into account using a probe-compensated near-field method, as will be discussed next.

Figure 6.18 illustrates the magnitude of the co- and cross-polarized raw data taken from the near-field measurement of the antenna at the center frequency. The cross-polarized near-field components of the antenna are significantly lower (30 dB) than the co-polarized components due to the nature of the patch array design. As shown in Figure 6.18, the input power is coupled strongly with the array elements near the antenna feed. As the wave travels along the meander waveguide, the power decays mainly due to the power coupling to the previous array elements. Some of the power loss is also attributed to the ohmic loss in the metallic waveguide. Per

simulation calculations the conductor loss is expected to be about 0.22 dB/cm and a coupling power drop of 4% per array element is expected. This amounts to a total decay of 0.44 dB per element. Hence 16 dB decay in the coupled power into the last array element compared to the first element is expected. This closely agrees with the measured 17 dB power drop shown in Figure 6.19 (a). In addition to the amplitude distribution, phase distribution is also a key factor in achieving the desired beam steering property. Figure 6.19 (b) illustrates the phase distribution in

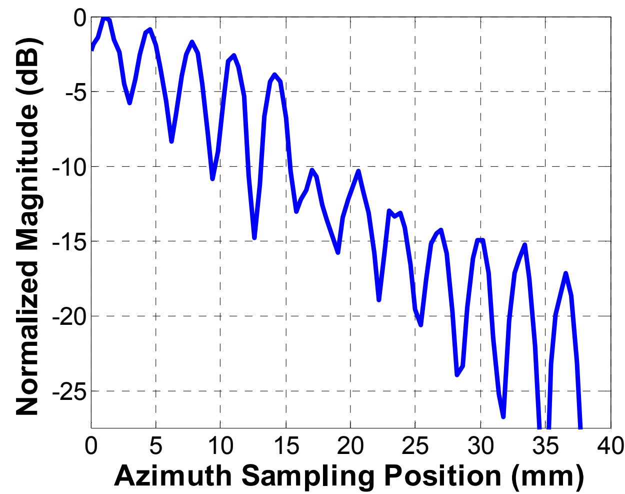

(a)

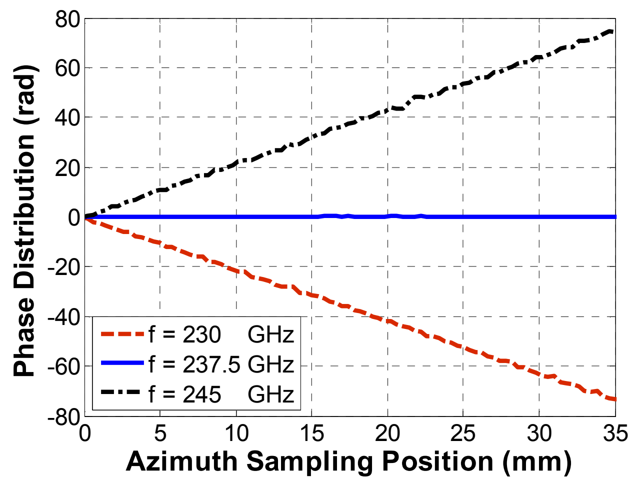

(b)

Figure 6.19. Measured (a) field intensity, and (b) phase distribution at the center frequency over the array elements along the azimuth (lateral) direction.

the azimuth (lateral) direction, where a linear phase distribution in the array elements at different operation frequencies is shown. This leads to the desired beam steering.

Once the AUT near-field data are collected, a probe-compensated near-field to far-field transformation [118] is used to obtain the far-field radiation pattern of the AUT using:

$$\vec{E}_{AUT}(\theta,\phi).\vec{E}_{probe}(\theta,-\phi) = \gamma \cos\theta e^{jk\cos\theta z_0} \times \int_{-\infty}^{\infty}\int_{-\infty}^{\infty} v(r).e^{jk\sin\theta(\cos\phi x+\sin\phi y)} d_x d_y \quad (6.1)$$

where $\vec{E}$ represents the far-field electric field pattern of the antenna and the *AUT* and *Probe* subscripts indicate the parameters related to the AUT and the open-ended near-field probe, respectively. γ is a measurement constant and the free-space wave number is expressed as k. z_0 represents the probe distance from the antenna as it is scanning in the *xy*-plane. Here θ and φ refer to the spherical coordinate angles used in characterizing the far-field radiation pattern, respectively. Also v(r) represents a term proportional to the open-circuit received voltage of the probe which is also proportional to the measured S_{21} at each scanned position. Using the measured voltages [v(r)] for both the co- and cross-polarized near-field components and the far-field electric field pattern of the probe ($\vec{E}_{Probe}$ determined analytically) the unknown far-field radiation pattern of the AUT is obtained from (6.1).

The measured normalized azimuth radiation pattern of the antenna is illustrated in Figure 6.20 (a). It is shown that the beam of the antenna steers from -23.5˚ to +25.3˚ as the frequency sweeps from 230 to 245 GHz with the beam pointing at the boresight of the antenna at the center frequency, i.e. 237.5 GHz. The measurements show that the antenna exhibits a narrow beamwidth of less than 2.8˚ (HPBW) over the entire scanning range. The exact control over the beam direction requires accurate adjustment of the phase shift between the elements and hence the propagation

constant in the microfabricated waveguide. This translates into accurate realization of the waveguide dimensions in the microfabrication process. The measured normalized pattern of the antenna in the elevation plane is also shown in Figure 6.20 (b). The antenna exhibits a HPBW of less than 10˚ in the elevation plane over the entire frequency range as expected from the simulation.

With the 3-D pattern of the antenna known (Figure 6.21), the directivity of the array antenna is calculated by integrating the measured 3-D radiation pattern at each frequency. After such computations, the plot of the directivity versus frequency is reported in Figure 6.22. The

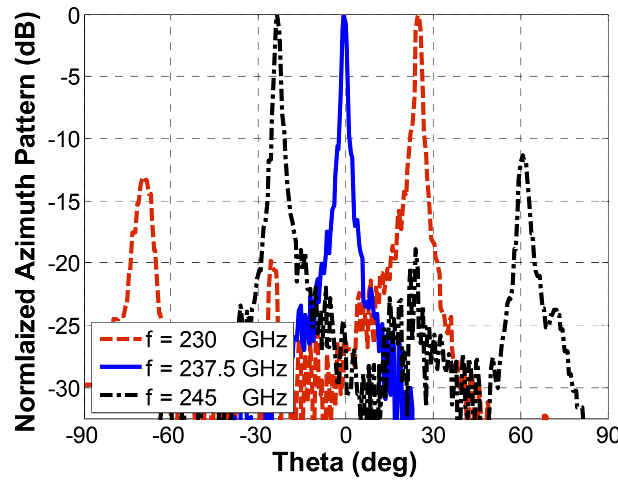

(a)

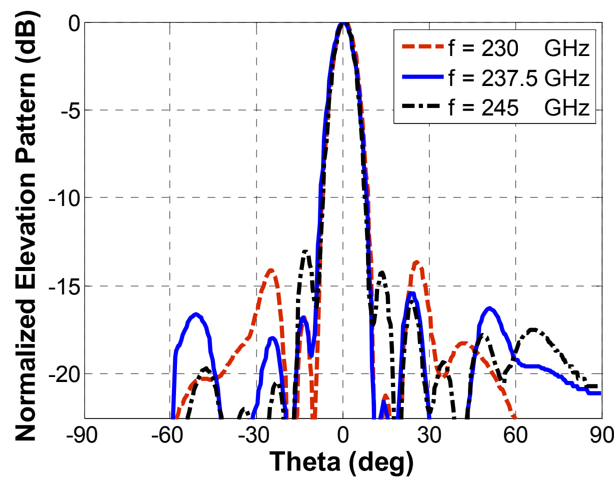

(b)

Figure 6.20. Normalized pattern of the co-polarized beam-steering antenna in the (a) azimuth plane, and (b) elevation plane.

maximum directivity is measured to be approximately 32.5 dB at the center frequency where the beam is pointing at the boresight of the antenna and the beamwidth is minimum. As the beam steers away from the boresight, the beamwidth increases and the array directivity drops. The appearance of suppressed grating lobes as side-lobes, when the beam is steered away from the boresight, also contributes to the drop in directivity for scanning angles beyond 15˚. As shown in Figure 6.22, the drop in directivity at the beginning and the end of the band is only about 1.5 dB. This is accomplished at the design stage where more coupling to the array elements is furnished as the frequency is moved away from the center frequency.

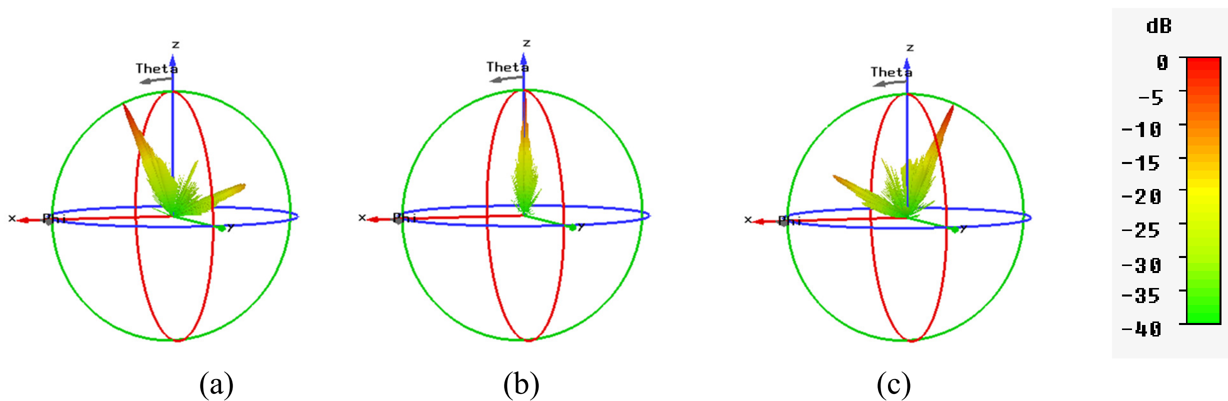

Figure 6.21. Measured normalized 3-D pattern of the co-polarized beam-steering antenna at (a) 230 GHz, (b) 237.5 GHz, and (c) 245 GHz.

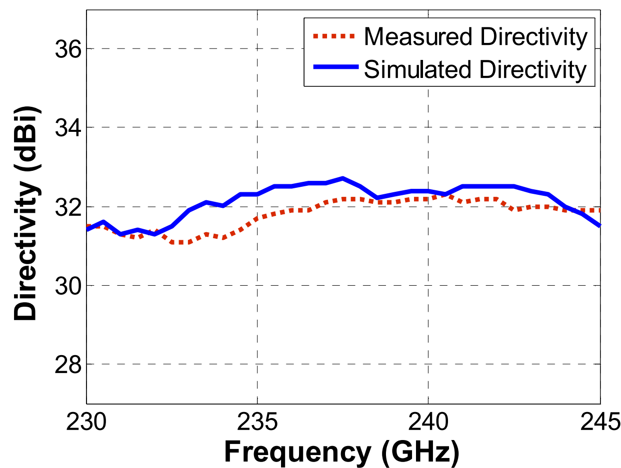

Figure 6.22. Measured directivity of the co-polarized antenna over the operation frequency range.

6.3.4. Cross-Polarized Antenna Measurement Results

The proposed near-field measurement setup along with the on-wafer transitions and probes are also used to characterize the radiation parameters of the cross-polarized beam-steering antenna. The measured normalized azimuth and elevation radiation pattern of the antenna are illustrated in Figure 6.23 (a) and Figure 6.23 (b), respectively. It is shown that the beam of the antenna steers

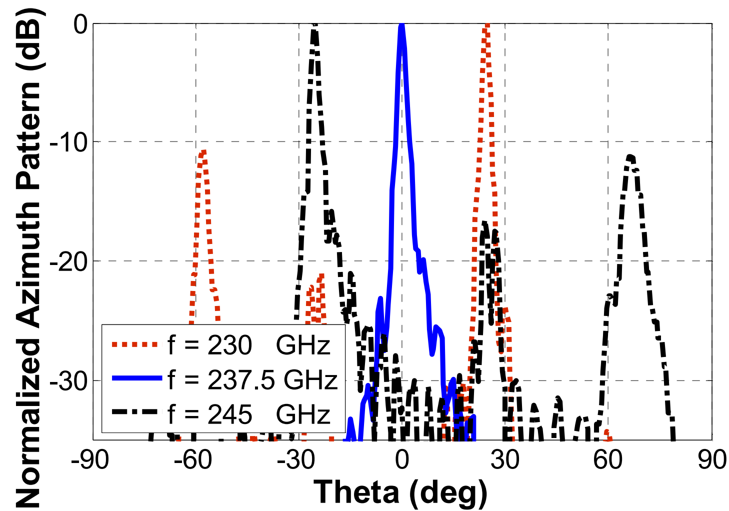

(a)

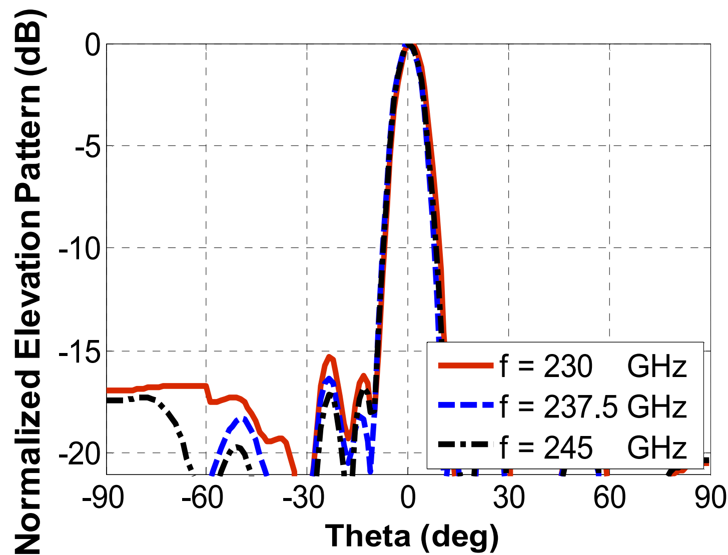

(b)

Figure 6.23. Normalized pattern of the cross-polarized beam-steering antenna in the (a) azimuth plane, and (b) elevation plane.

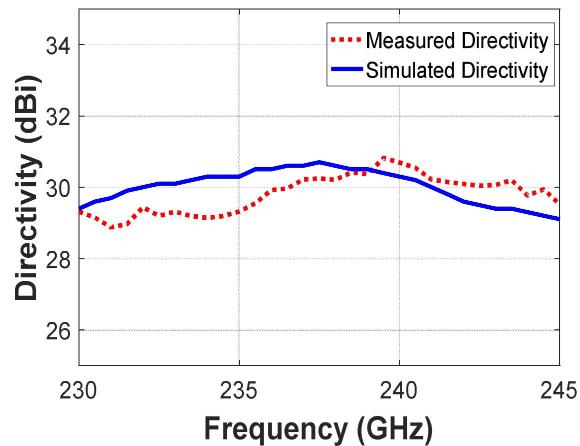

Figure 6.24. Measured directivity of the cross-polarized antenna over the operation frequency range.

from -24˚ to +24.5˚ as the frequency sweeps from 230 to 245 GHz with the beam pointing at the boresight of the antenna at the center frequency, i.e. 237.5 GHz. The measurements show that the antenna exhibits a narrow beamwidth of less than 3˚ and 10˚ (HPBW) in azimuth and elevation planes, respectively. The directivity of the array antenna is also calculated by integrating the measured 3-D radiation pattern at each frequency and the presented in Figure 6.24. The maximum directivity is measured to be approximately 30.8 dB at the center frequency where the beam is pointing at the boresight of the antenna and the beamwidth is minimum. As the beam steers away from the boresight, the beamwidth increases and the array directivity drops.

6.4. Near-field Antenna Gain Measurement Method

Near-field measurement methods are commonly used to characterize the radiation pattern of antennas and cannot provide the antenna gain directly. Further measurements are required for absolute gain characterization. Traditionally, the method of substitution in the far-field region is used to measure the gain of an unknown antenna. However, due to the limitations stated in Section 6.2, the far-field approach is not a viable approach for high MMW frequencies and the type of

antennas considered in this work. To characterize the gain of on-wafer broadband antennas using the aforementioned near-field system, a near-field gain measurement approach is employed [119].

6.4.1. Theoretical Background

Similar to the far-field gain measurement approaches, the near-field gain measurement methods can be divided into two main categories, namely, the absolute and relative gain measurement techniques. In the absolute near-field gain measurement technique, the system transfer function must be characterized. That is, the transfer function from the field intensity to the received power by the near-field probe must be characterized to compute the gain. This is rather a complicated task as it requires the creation of known fields within the probe station environment.

In the relative or so-called the method of substitution, the antenna gain is determined by establishing a comparison between the measured near-field data of the AUT and a standard antenna with a known gain. This allows determining the gain of the AUT based on the gain and the near-field data of the standard antenna. The gain of the AUT can easily be computed using:

$$G_{AUT} = \left(\frac{1 - |\Gamma_{STD}|^2}{1 - |\Gamma_{AUT}|^2} \right) \left(\frac{\left| \overrightarrow{FF}_{AUT} \right|_{Max}}{\left| \overrightarrow{FF}_{STD} \right|_{Max}} \right)^2 G_{STD} \tag{6.2}$$

where Γ represents the reflection from the port of the antenna and the *STD* subscript indicate the parameters related to the standard antenna. $\overrightarrow{FF}$ denotes the far-field pattern function of the antenna determined from the near-field data assuming all measurement parameters are kept unchanged. $\left|\overrightarrow{FF}_{Max}\right|$ also represents the maximum magnitude value of $\overrightarrow{FF}$ over the entire 2-D angle.

6.4.2. Measured Antenna Gain Results

A pyramidal horn antenna is used as the reference antenna in the following measurements, as shown in Figure 6.25. This antenna has aperture size of 6 mm by 8.5 mm and has a far-field

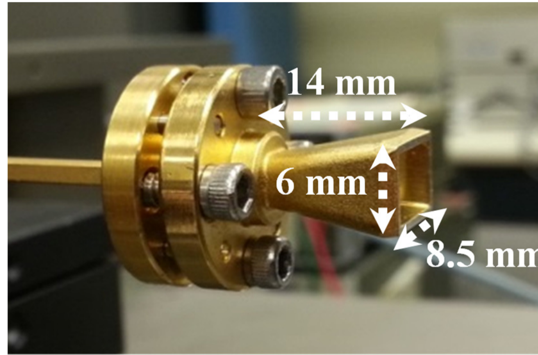

Figure 6.25. Close-up of the WR-3 pyramidal horn antenna as the reference antenna.

range of 200 mm at the desired frequency range. This allows for the provision of the gain using the method of identical antennas [120]. For measurement of absolute gain of the pyramidal horn antenna, a far-field measurement setup consisting of two identical pyramidal horn antennas positioned at the far-field of each other is used. The antennas are connected to the output ports of two frequency extenders that are calibrated up to their ports. The extenders are placed on two micro-positioners and the positions of the extenders are adjusted so that the boresight of the two antennas are aligned, as show in Figure 6.26. By measuring the S_{21}, the gain value of the antenna can be obtained using the Friis transmission formula

$$\frac{P_r}{P_t} = \left(\frac{\lambda_0}{4\pi R}\right)^2 G_t G_r \xrightarrow{G_t = G_r = G} G = \left(\frac{4\pi R}{\lambda_0}\right)\sqrt{\frac{P_r}{P_t}} \tag{6.3}$$

Here R is the distance between the two antennas and $\sqrt{P_r/P_t} = |S_{21}|$ is the ratio of the square root of the receive to transmit powers, respectively. G represents the gain values of transmit and receive antennas. Figure 6.27 illustrates the measured gain of the standard antenna over the desired frequency band.

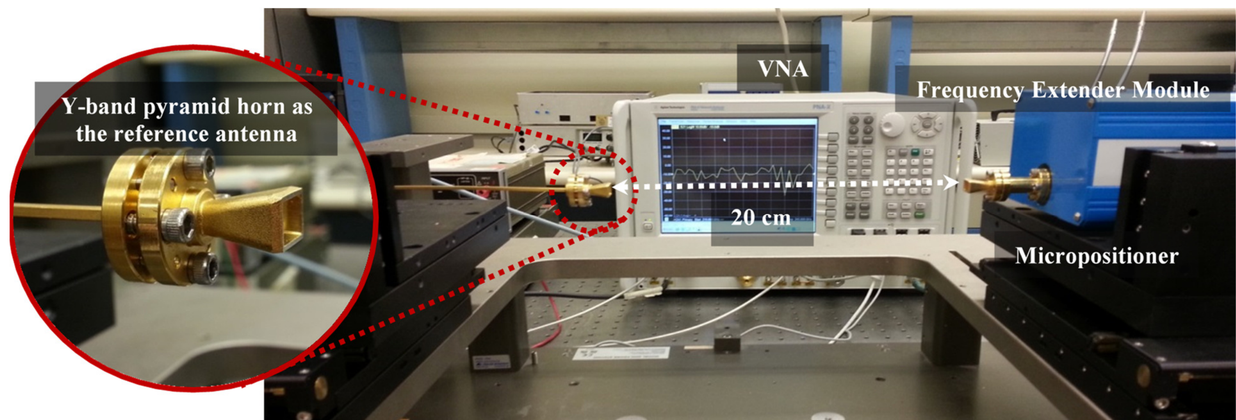

Figure 6.26. Photo of the WR-3 band antenna far-field measurement setup for gain characterization of the WR-3 band pyramid horn antenna as the reference antenna.

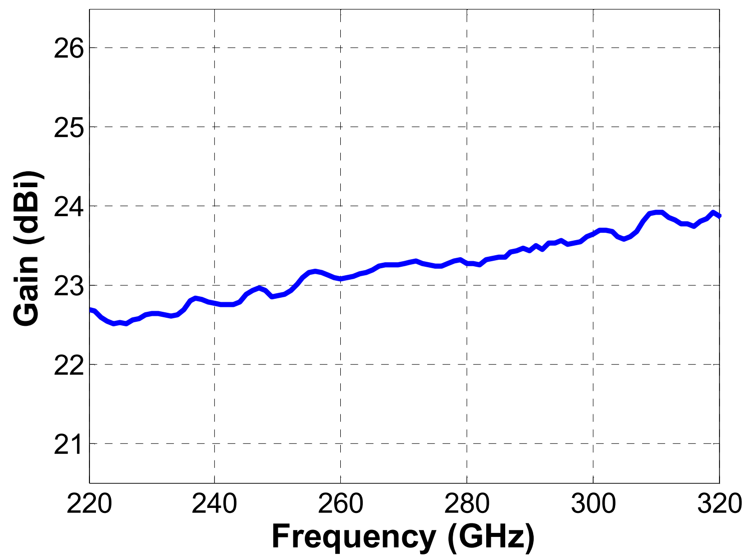

Figure 6.27. Measured gain of the standard pyramidal horn antenna.

With the gain of the standard antenna determined, the near-field pattern measurement of the standard antenna is needed in order to find the gain of the AUT as given by (6.3). As mentioned before, the measurement parameters of the near-field setup must be kept constant between the two measurements. In order to feed the horn antenna and keep the antennas aperture aligned with the horizontal scanning plane, a custom-made WR-3 waveguide segment is fabricated and used with

its ports connected to the waveguide port of the frequency extender and the horn antenna, as shown in Figure 6.28. The difference between the insertion losses of the waveguides that feed the AUT and the horn antenna is measured and considered in the gain measurements. Since these waveguides are bent and one does not have flange at one end, their insertion loss is measured by measuring the reflection coefficient of these waveguides when short-circuited. In this case, the

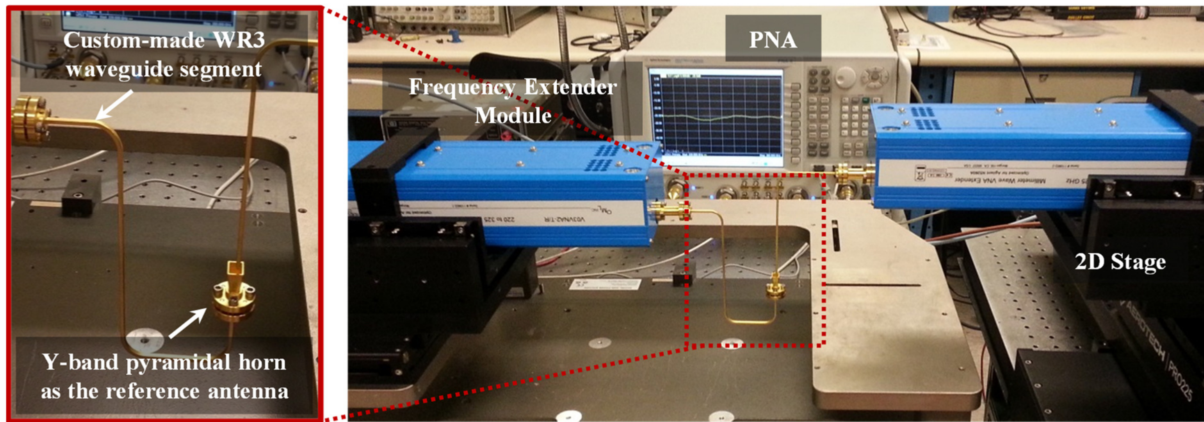

Figure 6.28. Photo of the WR-3 band antenna near-field measurement setup for characterization of the pyramidal horn antenna fed by custom-made waveguide segment.

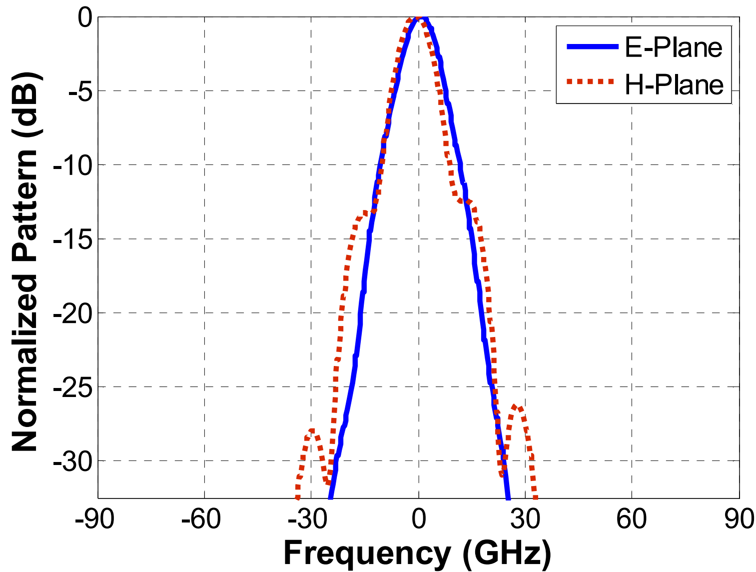

Figure 6.29. Normalized pattern of the pyramidal horn antenna at 260 GHz.

magnitude of reflection coefficient is simply twice the value of insertion loss. Figure 6.29 also shows the extracted far-field pattern of the standard antenna in E and H planes.

The gain of the co-polarized beam steering antenna is illustrated in Figure 6.30 where comparison between the measured and simulated antenna gains is presented and close agreement

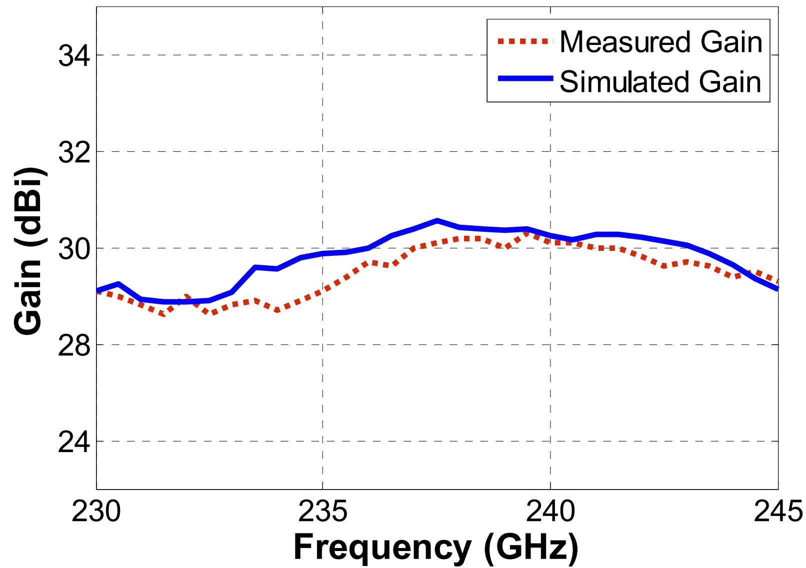

Figure 6.30. Comparison between the measured and simulated gain of the co-polarized beam-steering antenna.

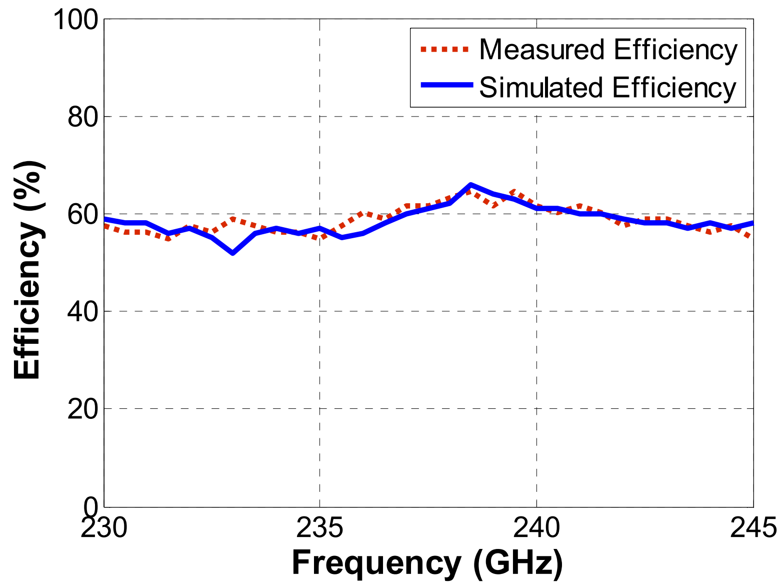

Figure 6.31. Measured and simulated efficiency of the microfabricated co-polarized beam-steering antenna over the desired frequency band.

Table 6.1. Summary of the co-polarized beam-steering antenna radiation characteristics: Comparison of the measured and simulated performance

Frequency (GHz)	Parameter	Simulated	Measured
230	Beam Direction (deg)	-24.1	-23.5
	Azimuth HPBW Beamwidth (deg)	2.4	2.8
	Elevation HPBW Beamwidth (deg)	9.3	9.6
	Gain (dB)	29.1	29.1
	Efficiency (%)	59	57
237.5	Beam Direction (deg)	0.0	0.0
	Azimuth HPBW Beamwidth (deg)	2.2	2.5
	Elevation HPBW Beamwidth (deg)	8.6	8.9
	Gain (dB)	30.7	30.2
	Efficiency (%)	61	62
245	Beam Direction (deg)	24.7	25.3
	Azimuth HPBW Beamwidth (deg)	2.5	2.6
	Elevation HPBW Beamwidth (deg)	8.9	9.1
	Gain (dB)	29.3	29.4
	Efficiency (%)	58	56

of the two are shown. The antenna exhibits a maximum gain of 30.2 dB at the center frequency with less than 2 dB gain variations as the beam steers to the edge angles. With the gain and directivity of the microfabricated antenna measured, the efficiency of the antenna is determined by finding the ratio of the two as illustrated in Figure 6.31. The antenna exhibits a radiation efficiency of over 55% over the desired frequency band. Table 6.1 summarizes the radiation characteristics of the micromachined co-polarized antenna and presents a comparison between the measured and simulated performance, where close agreements are shown.

The gain and efficiency of the cross-polarized beam scanning antenna is also measured and the results are shown in Figure 6.32 and Figure 6.33, respectively. As shown, the cross-pol antenna

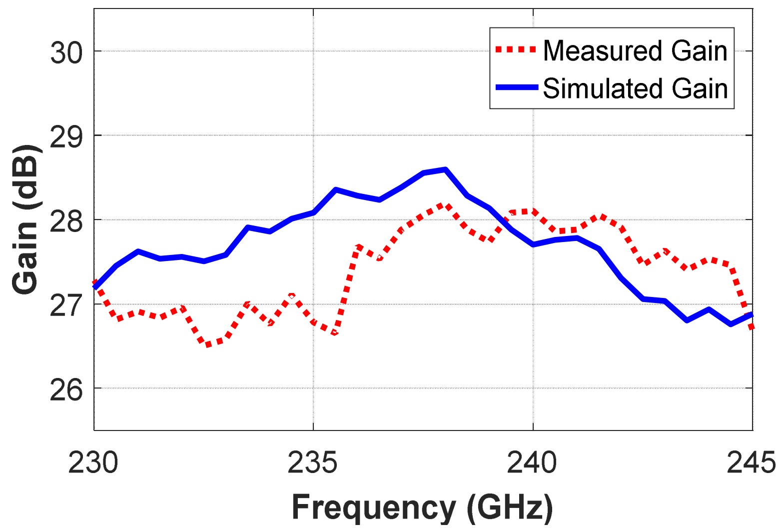

Figure 6.32. Comparison between the measured and simulated gain of the cross-polarized beam-steering antenna.

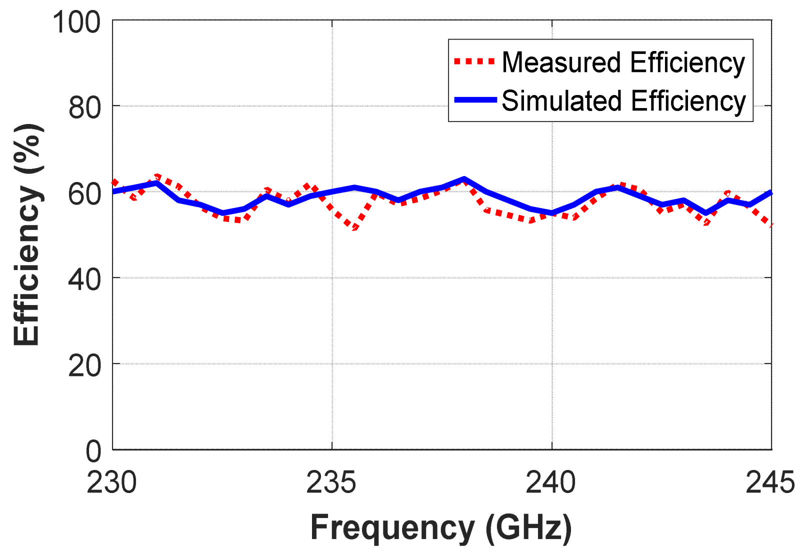

Figure 6.33. Measured and simulated efficiency of the microfabricated cross-polarized beam-steering antenna over the desired frequency band.

exhibits a maximum gain of 28.2 dB at the center frequency with a peak radiation efficiency of 50%. Table 6.2 summarizes the measured radiation characteristics of the cross-polarized antenna and presents a comparison between the measured and simulated results. The cross-pol isolation of

Table 6.2. Summary of the cross-polarized beam-steering antenna radiation characteristics: Comparison of the measured and simulated performance

Frequency (GHz)	Parameter	Simulated	Measured
230	Beam Direction (deg)	-23.1	-24.0
	Azimuth HPBW Beamwidth (deg)	2.5	2.9
	Elevation HPBW Beamwidth (deg)	9.8	9.8
	Gain (dB)	27.2	27.3
	Efficiency (%)	60	63
237.5	Beam Direction (deg)	0.0	0.0
	Azimuth HPBW Beamwidth (deg)	2.3	2.6
	Elevation HPBW Beamwidth (deg)	9.5	9.3
	Gain (dB)	28.7	28.2
	Efficiency (%)	62	60
245	Beam Direction (deg)	23.6	24.5
	Azimuth HPBW Beamwidth (deg)	2.4	2.8
	Elevation HPBW Beamwidth (deg)	9.4	9.5
	Gain (dB)	26.8	26.7
	Efficiency (%)	61	52

both horizontally and vertically polarized antennas is also measured and a cross-pol isolation of better than 50 dB is reported.

6.5. Chip Package Measurements

In this section, the characterization of the micromachined package for integration of the active and passive MMICs is presented. This includes characterization of both RF performance of the package as well as the performance of the biasing network and the associated RF choke, which are presents in the following sub-sections.

6.5.1. RF Measurement of the Package

To characterize the RF performance of the packaging block, a thru-line MMIC is integrated into the package and the *S*-parameters of the packaged chip is measured using a non-contact on-wafer measurement technique [121]. Figure 6.34 shows the close-up of the package along with the

RF transitions from waveguide ports of the package to the on-chip CPW ports of the packaged chip. In this measurement approach, the waveguide probe attached to the first frequency extender is used along with the on-wafer micromachined transition to feed the first port of the on-wafer package. An on-wafer near-field probe with tapered tip is also connected to the second frequency extender to allow full S-parameter measurements. Additionally, specially designed slots are devised at each port of the package to allow slight coupling of the signal propagating in the micromachined waveguides to the near-field probe. A matched load realized by an array of slots is also incorporated at the second port of the package to suppress the reflections from the second port. Next, by measuring the coupled signal at each port of the packaged chip, the *S*-parameters of the package with the integrated thru-line chip is extracted and the measurement results are shown in Figure 6.35. For fair evaluation of the RF performance of the package, the insertion loss of the MMIC itself are accurately measured using WR-3 GSG probes and are subtracted from the measurement of the packaged chip, to represent only the insertion loss introduced by the packaging method. This assumption is only valid under the situation where there are minimal reflections in

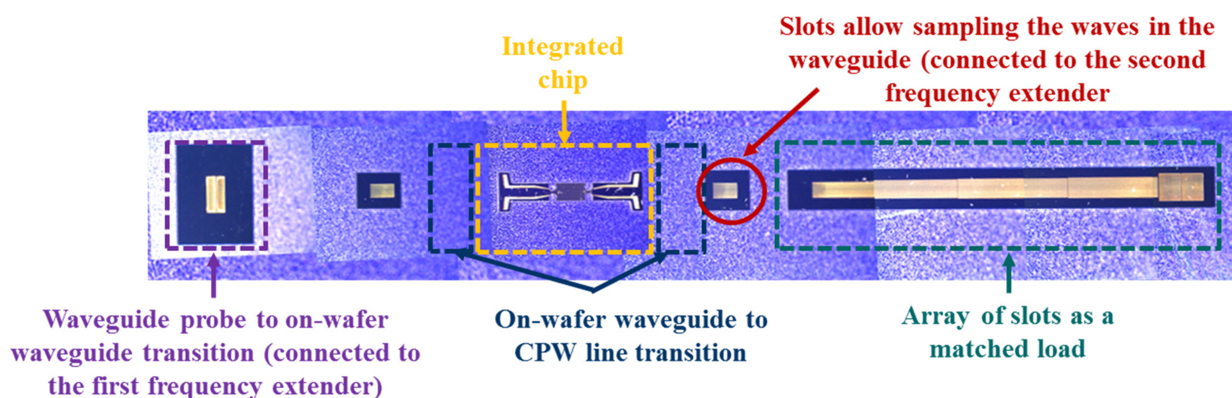

Figure 6.34. Close-up of the package along with the RF transitions from waveguide ports of the package to the on-chip CPW ports of the packaged chip. The MMIC is packaged at the center and its *S*-parameters are measured using a non-contact on-wafer measurement technique [121].

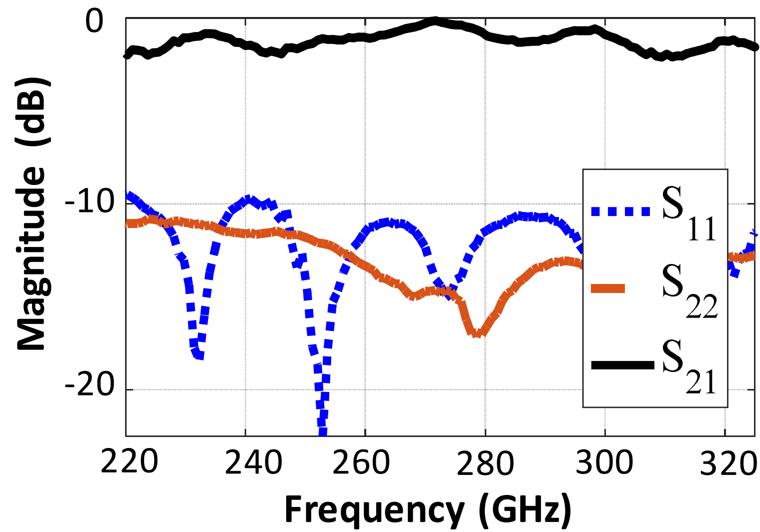

Figure 6.35. Measured *S*-parameters of a packaged thru-line InP chip over the WR-3 frequency band. For fair evaluation of the RF performance of the package, the insertion loss of the MMIC is measured separately and is de-embedded from the measurements to represent only the performance of the package.

the DUT, which is valid in this case. As shown, the package exhibits a very good match of less than -10 dB at each port with a low insertion loss of less than 1.2 dB per each transition.

6.5.2. RF Measurements of the Broadband RF-Choke

As discussed in Chapter 4, a broad-band RF-choke is developed to block the loading effects of the DC bias network from the RF circuit components and avoid the possible instability of the integrated active devices. To evaluate the performance of the RF-choke over a wide frequency range, a setup consisting of an Agilent N5245 4-port network analyzer along with OML MMW frequency extending modules with the appropriate GSG probes is used to enable two-port measurements from DC to 330 GHz with the exclusion of 40-70 GHz and 120-200 GHz frequency bands. Figure 6.36 illustrates the measured *S*-parameters of the RF-choke where a reflection loss

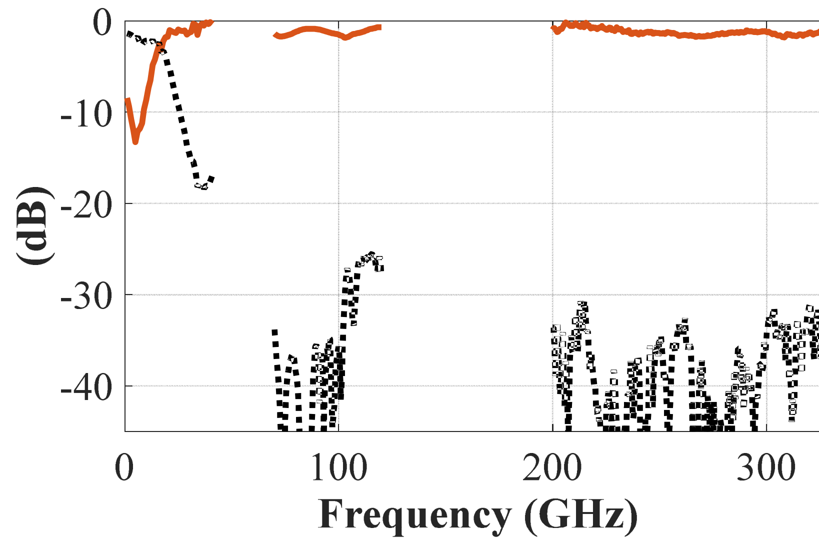

Figure 6.36. Measured *S*-parameters of the broad-band RF-choke over various frequency bands showing an RF isolation of better than 10 dB with a reflection loss of less than 2 dB over the entire desired frequency range (30-330 GHz).

of better than 2 dB with an RF isolation of better than 10 dB is achieved over the entire frequency range (30-330 GHz).

6.5.3. DC Measurements of the Package

In order to verify the biasing condition of the packaging block, DC measurements of a packaged chip is performed using an Agilent U2723A source measurement unit. In this measurement a single stage amplifier chip is integrated into the packaging block and the I-V characteristics of the transistor is extracted, as presented in Figure 6.37, where successful biasing of the device is shown. Additionally, the DC ohmic resistance between the on-wafer DC lines and the on-chip DC pads is measured, after de-embedding the resistance of the probes, and a resistance of 2.7 Ω per contact is reported.

6.5.4. RF Measurements of Active MMIC

To characterize the performance of the packaging block for integration of active MMIC, a single stage amplifier with a poor gain (loss) operating at 210-220 GHz frequency range is

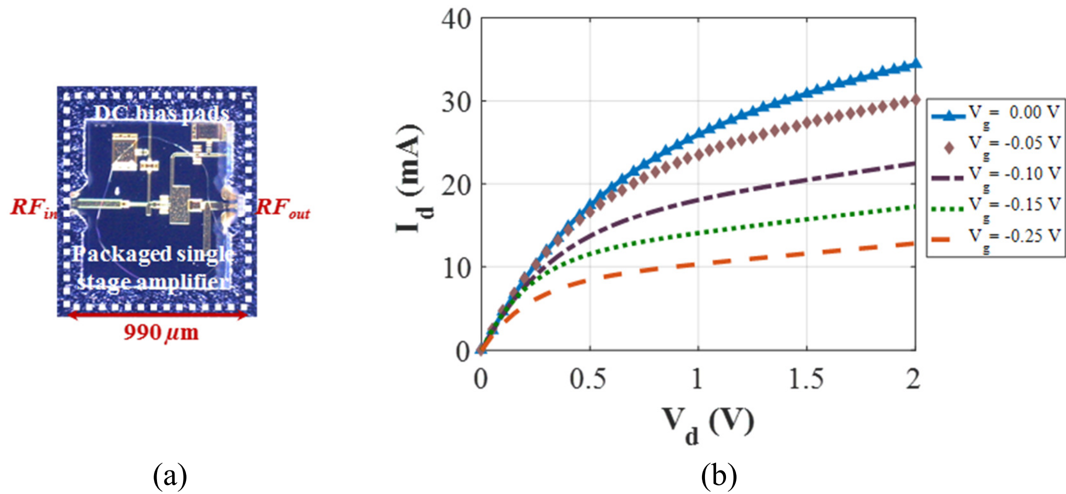

Figure 6.37. (a) Close-up of a packaged single stage amplifier, and (b) Measured I-V characteristics of the packaged MMIC, verifying successful biasing of active MMIC in the package.

integrated into the block and the *S*-parameters of the packaged amplifier are measured using the measurement setup with WR-3 frequency extender units. Figure 6.38 illustrates the measured *S*-parameters of the MMIC before and after packaging. As shown, the package introduces minimal effect (less than 1.2 dB of loss per transition) on the performance of the packaged MMIC.

6.6. Summary

Measurement methods for characterization of MMW and sub-MMW components and sub-systems are presented and the measurement results of the microfabricated components are shown in this chapter. This includes a near-field antenna characterization system for MMW and sub-MMW band measurements. The setup is based on using an open-ended waveguide probe with a tapered tip to measure the near-field distribution over the antenna. A waveguide probe approach is also devised to feed the waveguide port of the micromachined antenna. Moreover, to characterize the gain of the AUT a comparative near-field gain measurement method is employed where the gain of the AUT is determined based on a comparative approach. Full characterization

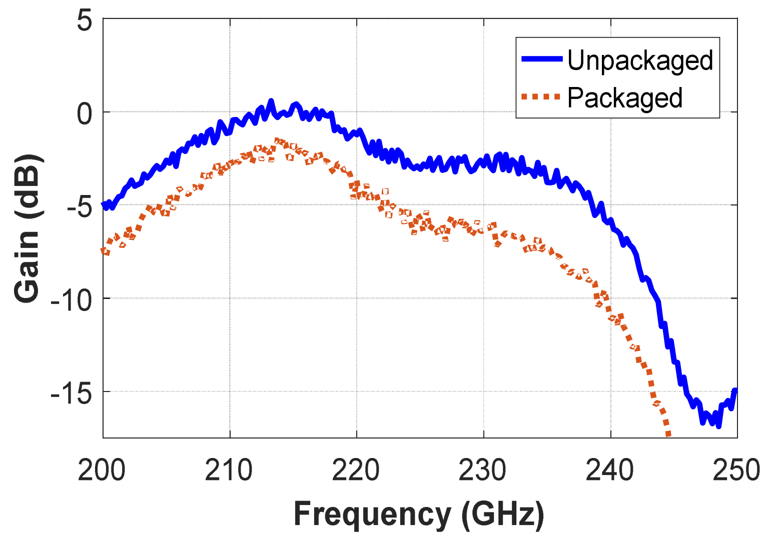

(a)

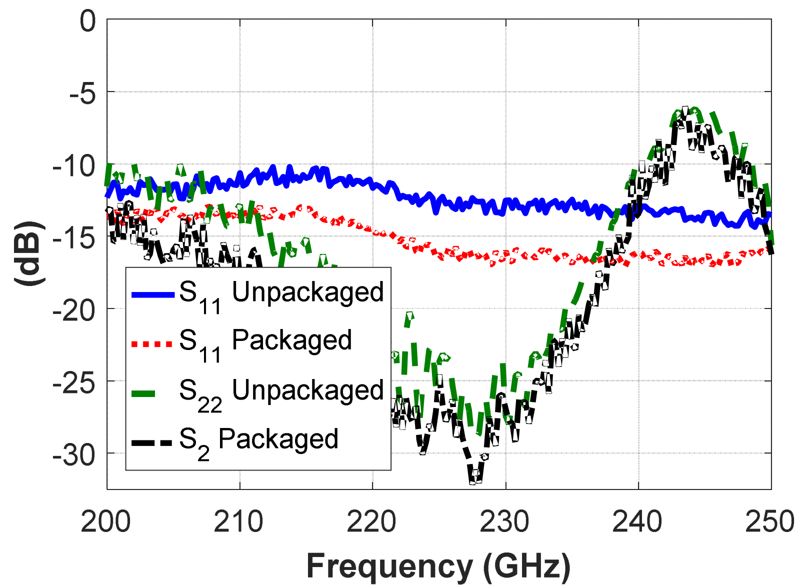

(b)

Figure 6.38. Measured *S*-parameters of a packaged single stage amplifier with poor gain (loss), before and after packaging. (a) Measured gain (S_{21}) of the amplifier showing minimal effect of the package (<1.2 dB per transition) on the performance of the MMIC, and (b) Measured reflections of the MMIC verifying minimal effects of the packaging technique.

of the co- and cross-polarized beam-steering antennas is performed and close agreement of the simulated and measured results is shown. In addition to the antenna characterizations, the

performance of the chip packaging method is measured for integration of active and passive MMICs, where low insertion loss of the package with very good matchings are reported.

CHAPTER 7
CONCLUDING REMARKS

7.1. Summary of Contributions

High frequency radars have gained considerable attention for navigation and mapping applications in autonomous systems. The key advantage of this high frequency sub-MMW radar system is that the short wavelength at the sub-MMW frequency band allows reduction of the size and mass of such sensor to fraction of that of lidars and low-frequency radars. Additionally, the short wavelength enables realization of electrically large but physically compact radar antennas with very narrow beams. This combined with the abundance of bandwidth at this frequency bands enables realization of a high performance radar system with centimeter-scale angular and range resolutions. Moreover, unlike lidars and optical sensors, the sub-MMW radar has the ability to see through poor weather, dust, smoke, cloth and other low loss but optically opaque materials and environments, all of which makes it very appealing for collision avoidance and navigation applications. However, there are many challenges that need to be overcome to fully exploit this band of electromagnetic wave spectrum. One major issue pertains to the difficulty in fabrication of components such as antennas, filters, couplers, power dividers and interconnects. Another issue is related to the complexity associated with measurement and characterization of components and RF sub-systems. Another challenge pertains to the design of high performance RF components

given the design challenges associated with design constraints imposed by standard fabrication methods, high RF losses at high MMW frequencies, etc.

This thesis presented the development of technology in support of a novel sub-MMW radar technology. This includes development and implementation of novel design, microfabrication, and measurement methods and techniques to develop the passive RF front-end of the radar system. The sub-MMW radar system is designed for navigation and mapping applications in autonomous systems. The salient features of the proposed radar are its ultra-lightweight (less than 5 grams), compact form factor (2 cm^3), low power consumption (6.7 mW for 1 fps), and ease of scalability to higher frequencies (up to 1 THz). The radar architecture is designed to be compatible with silicon micromachining technology for repeatable and reliable fabrications with high accuracies.

One of the major contributions of this dissertation is the development of the antenna systems for such high MMW radar system. In order to satisfy the requirements for high resolution and wide field of view for this imaging and navigation radar sensor, frequency scanning beam-steering antennas are developed to achieve ±25˚ of beam steering with a very narrow beam of 2.5˚ in the direction of scan. The designed array antenna has over 600 radiating elements and exhibits a radiation efficiency of over 55% over the entire scanning range and provides a gain of over 30 dBi over the entire operation frequency range. Additionally, for polarimetry applications, two versions of the antenna with both co- and cross-polarizations are developed to allow full-polarimetry imaging at sub-MMW frequencies. This is particularly important as targets show higher cross-pol signatures at such high frequencies. The co- and cross-pol antennas are designed to be compatible with silicon micromachining technology that allows implementation of both antennas with various antenna combinations on a single silicon block for full-polarimetric radar system.

Another major accomplishment of this work is design and implementation of a novel chip packaging methodology for sub-MMW integration of active and passive MMIC in the RF front-end. The packaging method is designed to be compatible with fabrication process of the antenna to allow seamless integration of the antennas and the MMIC on a single wafer for a compact and cost-effective solution. Additionally, the packaging method offers a low-loss (less than 1.2 dB per transition) and wideband (covering the entire WR-3 band) integration solution in the sub-MMW to THz frequency band which can be standardized for reliable and repeatable integrations at such frequencies. In order to enable biasing of the active MMIC, a seamless biasing network consisting of an ultra-wideband RF-choke with a decade bandwidth (30-330 GHz) as well as the associated DC pads are devised as part of the integration block. The new integration method is readily compatible with MMIC and silicon micromachining technology and should find a wide range of applications in sub-MMW frequencies.

One contribution of this work is development of fabrication methods for realization of MMW and sub-MMW systems and sub-systems. At high MMW frequencies, the dimensions of the lines and waveguides shrink which limits the use of standard machining methods. Silicon micromachining technology, on the other hand, offers a standard fabrication method for realization of complex structures with low mass and low cost with the required dimensional control. In this work, a silicon micromachining technique is developed to fabricate the entire radar front-end on a single silicon platform for high level of fabrication tolerance and accuracy. Various microfabrication procedures are optimized and employed to enable reliable fabrication of the radar RF front-end. This includes multi-layer mask deposition and patterning, multi-step silicon DRIE, gold deposition, gold-gold thermos-compression bonding, polymer membrane deposition and

patterning process, membrane alignment and transfer, low-stress silicon-oxide/silicon nitride deposition and releasing for free standing membranes, etc.

Repeatable and reliable characterization of sub-MMW components and sub-systems is a very challenging task and one major contribution of this dissertation pertains to development of novel measurement techniques to enable reliable on-wafer characterization of such devices in MMW to THz band. This includes development of a novel waveguide probe measurement technique along with specially designed probes and the associated transitions for on-wafer S-parameter measurements at sub-MMW frequencies. This method is used for on-wafer characterization of waveguide-based components including the antennas and the chip package for the radar RF front-end. Additionally, a novel on-wafer near-field measurement method is also developed to allow 3-D pattern and power (gain and efficiency) characterization of the antennas at sub-MMW frequencies. Successful characterization of all micromachined components are performed using the devised measurement methods and excellent agreement of designed and measured results are shown.

7.2. Future Directions

All passive components and sub-systems of the RF front-end of the sub-MMW radar, including co- and cross- polarized antennas as well as the chip packaging and the associated transitions, are successfully developed and tested. The active MMICs for driving the radar system are under development by other collaborators in this project. Upon successful development of these active modules, the future work on development of this radar system is to integrate all active modules with the passive RF front-end to realize and test the functional radar prototype.

Current fabrication of the radar RF front-end is based on silicon micromachining technology. While this technology offers very high fabrication tolerances, it requires many fabrication steps along with accurate tool characterization requirements, making it not compatible for mass-production of the radar. Another future direction for the radar system is to develop novel low-cost and mass-producible fabrication techniques to allow production of the sensor in large quantities. Perhaps one possible solution is to develop casting methods to mass produce the radar front-end by applying a mold to a substrate to cast the radar front-end. Another alternative is to develop novel 3-D printing techniques for rapid and accurate printing of the waveguide-based RF front-end.

BIBLIOGRAPHY

[1] R. W. McMillan, “Terahertz Imaging, Millimeter-wave Radar”, *Advances in Sensing with Security Applications, NATO Security Through Science Series*, vol 2. Springer, Dordrecht.

[2] J. C. Wiltse, "History of Millimeter and Submillimeter Waves," *in IEEE Transactions on Microwave Theory and Techniques*, vol. 32, no. 9, pp. 1118-1127, Sep 1984.

[3] P. H. Siegel, "Terahertz technology," *in IEEE Transactions on Microwave Theory and Techniques*, vol. 50, no. 3, pp. 910-928, Mar 2002.

[4] T. G. Phillips and J. Keene, "Submillimeter astronomy [heterodyne spectroscopy]," in *Proceedings of the IEEE*, vol. 80, no. 11, pp. 1662-1678, Nov 1992.

[5] P. H. Siegel, "Terahertz technology in biology and medicine," *in IEEE Transactions on Microwave Theory and Techniques*, vol. 52, no. 10, pp. 2438-2447, Oct. 2004.

[6] Z. D. Taylor *et al*., "THz Medical Imaging: in vivo Hydration Sensing," in *IEEE Transactions on Terahertz Science and Technology*, vol. 1, no. 1, pp. 201-219, Sept. 2011.

[7] T. Bowman, M. El-Shenawee and S. G. Sharma, "Terahertz spectroscopy for the characterization of excised human breast tissue," *2014 IEEE MTT-S International Microwave Symposium (IMS2014)*, Tampa, FL, 2014, pp. 1-4.

[8] H. J. Song, J. Y. Kim, K. Ajito, N. Kukutsu and M. Yaita, "50-Gb/s Direct Conversion QPSK Modulator and Demodulator MMICs for Terahertz Communications at 300 GHz," in *IEEE Transactions on Microwave Theory and Techniques*, vol. 62, no. 3, pp. 600-609, March 2014.

[9] S. Kim *et al*., "300 GHz Integrated Heterodyne Receiver and Transmitter With On-Chip Fundamental Local Oscillator and Mixers," in *IEEE Transactions on Terahertz Science and Technology*, vol. 5, no. 1, pp. 92-101, Jan. 2015.

[10] K. Katayama *et al*., "A 300GHz 40nm CMOS transmitter with 32-QAM 17.5Gb/s/ch capability over 6 channels," *2016 IEEE International Solid-State Circuits Conference (ISSCC)*, San Francisco, CA, 2016, pp. 342-343.

[11] K. Takano, K. Katayama, S. Amakawa, T. Yoshida and M. Fujishima, "A 300-GHz 64-QAM CMOS transmitter with 21-Gb/s maximum per-channel data rate," *2016 11th European Microwave Integrated Circuits Conference (EuMIC)*, London, 2016, pp. 193-196.

[12] K. Takano *et al*., "A 105Gb/s 300GHz CMOS transmitter," *2017 IEEE International Solid-State Circuits Conference (ISSCC)*, San Francisco, CA, 2017, pp. 308-309.

[13] I. Kallfass, F. Boes, T. Messinger, J. Antes, A. Inam, U. Lewark, A. Tessmann, R. Henneberger, "64 gbit/s transmission over 850 m fixed wireless link at 240 GHz carrier frequency", *Journal of Infrared Millimeter and Terahertz Waves*, vol. 36, no. 2, pp. 221-233, 2015.

[14] S. Koenig *et al.* “Wireless sub-THz communication system with high data rate”, *Nature Photonics 7*, no. 12, 977-981, 2013.

[15] B. Cooper *et al*., “Penetrating 3-D imaging at 4- and 25-m range using a submillimeter-wave radar,” *IEEE Trans. Microw. Theory Techn*., vol. 56, no. 12, pt. 1, pp. 2771–2778, Dec. 2008.

[16] Y. Alvarez, B. Gonzalez-Valdes, J. Á. Martinez, F. Las-Heras and C. M. Rappaport, "3D Whole Body Imaging for Detecting Explosive-Related Threats," in IEEE Transactions on Antennas and Propagation, vol. 60, no. 9, pp. 4453-4458, Sept. 2012.

[17] G. Rubio-Cidre *et al*., "Characterization of a 300 GHz imaging radar for standoff detection," *2014 International Radar Conference*, Lille, 2014, pp. 1-6.

[18] R. Appleby and H. B. Wallace, "Standoff Detection of Weapons and Contraband in the 100 GHz to 1 THz Region," in *IEEE Transactions on Antennas and Propagation*, vol. 55, no. 11, pp. 2944-2956, Nov. 2007.

[19] K. B. Cooper *et al*., "A High-Resolution Imaging Radar at 580 GHz," in *IEEE Microwave and Wireless Components Letters*, vol. 18, no. 1, pp. 64-66, Jan. 2008.

[20] D. M. Sheen, D. L. McMakin and T. E. Hall, "Three-dimensional millimeter-wave imaging for concealed weapon detection," in *IEEE Transactions on Microwave Theory and Techniques*, vol. 49, no. 9, pp. 1581-1592, Sep 2001.

[21] D. T. Petkie *et al.,* "Active and passive millimeter and sub-millimeter-wave imaging", Proc. SPIE, vol. 5989, pp. 5989181-5989188, 2005.

[22] J. C. Dickinson *et al.,* "Terahertz imaging of subjects with concealed weapons", Proc. SPIE, vol. 6212, pp. 62120Q-1-62120Q-12, 2006.

[23] M. Ijaz, Z. Ghassemlooy, J. Pesek, O. Fiser, H. Le Minh, and E. Bentley, "Modeling of Fog and Smoke Attenuation in Free Space Optical Communications Link Under Controlled Laboratory Conditions," *Journal of Lightwave Technology,* vol. 31, pp. 1720-1726, 2013.

[24] M. Ijaz, Z. Ghassemlooy, A. Gholami and X. Tang, "Smoke attenuation in free space optical communication under laboratory controlled conditions," *Telecommunications (IST), 2014 7th International Symposium on*, Tehran, 2014, pp. 758-762.

[25] M. Grabner and V. Kvicera, "Multiple Scattering in Rain and Fog on Free-Space Optical Links," in *Journal of Lightwave Technology*, vol. 32, no. 3, pp. 513-520, Feb.1, 2014.

[26] H. J. Liebe, T. Manabe, and G. A. Hufford, "Millimeter-wave attenuation and delay rates due to fog/cloud conditions," *Antennas and Propagation, IEEE Transactions on,* vol. 37, pp. 1617-1612, 1989.

[27] World Health Organization (WHO) (2015), *Road Traffic Deaths and Proportion of Road Users by Country/Area*, [Online]. Available: http://www.who.int/violence_injury_prevention/road_safety_status/2015/en/

[28] J. S. Humbert, I. Chopra, R. S. Fearing, R. J. Full, R. J. Wood, and M. H. Dickinson, "Development of micromechanics for micro-autonomous systems (ARL-MAST CTA Program)," 2009, pp. 73180L-73180L-6.

[29] X. Deng, L. Schenato, W. C. Wu, and S. S. Sastry, "Flapping flight for biomimetic robotic insects: Part I-system modeling," *IEEE Transactions on Robatics,* vol. 22, pp. 776-788, 2006.

[30] G. T. Sibley, M. H. Rahimi, and G. S. Sukhatme, "Robomote: A tiny mobile robot platform for large-scale ad-hoc sensor networks," in *Robotics and Automation, 2002. Proceedings. ICRA'02. IEEE International Conference on*, 2002, pp. 1143-1148.

[31] I. Kroo, F. Prinz, M. Shantz, P. Kunz, G. Fay, S. Cheng*, et al.*, "The Mesicopter: A miniature rotorcraft concept–phase ii interim report," ed: Stanford university, USA, 2000.

[32] A. M. Hoover, E. Steltz, and R. S. Fearing, "RoACH: An autonomous 2.4 g crawling hexapod robot," in *Intelligent Robots and Systems, 2008. IROS 2008. IEEE/RSJ International Conference on*, 2008, pp. 26-33.

[33] C. Niclass, M. Soga, H. Matsubara, S. Kato, and M. Kagami, "A 100-m Range 10-Frame/s 340 96-Pixel Time-of-Flight Depth Sensor in 0.18-CMOS," 2013.

[34] S. Chung, H. Abediasl and H. Hashemi, "15.4 A 1024-element scalable optical phased array in 0.18µm SOI CMOS," *2017 IEEE International Solid-State Circuits Conference (ISSCC)*, San Francisco, CA, 2017, pp. 262-263.

[35] J. Sun, E. Timurdogan, A. Yaacobi, E. S. Hosseini, M. R. Watts, "Large-scale nanophotonic phased array", *Nature*, vol. 493, no. 7431, pp. 195-199, Jan. 2013.

[36] R. A. Jarvis, "A Laser Time-of-Flight Range Scanner for Robotic Vision," in *IEEE Transactions on Pattern Analysis and Machine Intelligence*, vol. PAMI-5, no. 5, pp. 505-512, Sept. 1983.

[37] M. U. de Haag, D. Venable, and M. Smearcheck, "Use of 3D laser radar for navigation of unmanned aerial and ground vehicles in urban and indoor environments," in *Defense and Security Symposium*, 2007, pp. 65500C-65500C-12.

[38] Stanford Mass Shootings in America, courtesy of the Stanford Geospatial Center and Stanford Libraries [Online]. Avialable: https://library.stanford.edu/projects/mass-shootings-america

[39] R. Kompfner, "The invention of traveling wave tubes," in *IEEE Transactions on Electron Devices*, vol. 23, no. 7, pp. 730-738, Jul 1976.

[40] G. Caryotakis, "The klystron: A microwave source of surprising range and endurance," *Physics Plasmas*, vol. 5, no. 5, pp. 1590-1598, May 1998.

[41] R. H. Varian, S. F. Varian, "A high frequency oscillator and amplifier", *J. Appl. Phys.*, vol. 10, pp. 321-327, May 1939

[42] H. A. H. Boot and J. T. Randall, "Historical notes on the cavity magnetron," in *IEEE Transactions on Electron Devices*, vol. 23, no. 7, pp. 724-729, Jul 1976.

[43] H. P. Groll and J. Detlefsen, "History of automotive anticollision radars and final experimental results of a MM-Wave car radar developed by the Technical University of Munich," in *IEEE Aerospace and Electronic Systems Magazine*, vol. 12, no. 8, pp. 15-19, Aug 1997.

[44] M. SeyyedEsfahlan, E. Öztürk, M. Kaynak and I. Tekin, "77-GHz Four-Element Phased-Array Radar Receiver Front End," in *IEEE Transactions on Components, Packaging and Manufacturing Technology*, vol. 6, no. 8, pp. 1162-1173, Aug. 2016.

[45] W. Shin, B. H. Ku, O. Inac, Y. C. Ou and G. M. Rebeiz, "A 108–114 GHz 4 x 4 Wafer-Scale Phased Array Transmitter With High-Efficiency On-Chip Antennas," in *IEEE Journal of Solid-State Circuits*, vol. 48, no. 9, pp. 2041-2055, Sept. 2013.

[46] T. Y. J. Kao, Y. Yan, T. M. Shen, A. Y. K. Chen and J. Lin, "Design and Analysis of a 60-GHz CMOS Doppler Micro-Radar System-in-Package for Vital-Sign and Vibration Detection," in *IEEE Transactions on Microwave Theory and Techniques*, vol. 61, no. 4, pp. 1649-1659, April 2013.

[47] J. Lee, Y. A. Li, M. H. Hung and S. J. Huang, "A Fully-Integrated 77-GHz FMCW Radar Transceiver in 65-nm CMOS Technology," in *IEEE Journal of Solid-State Circuits*, vol. 45, no. 12, pp. 2746-2756, Dec. 2010.

[48] A. Tessmann, S. Kudszus, T. Feltgen, M. Riessle, C. Sklarczyk and W. H. Haydl, "Compact single-chip W-band FMCW radar modules for commercial high-resolution sensor applications," in *IEEE Transactions on Microwave Theory and Techniques*, vol. 50, no. 12, pp. 2995-3001, Dec 2002.

[49] P. N. Chen, P. J. Peng, C. Kao, Y. L. Chen and J. Lee, "A 94GHz 3D-image radar engine with 4TX/4RX beamforming scan technique in 65nm CMOS," *2013 IEEE International Solid-State Circuits Conference Digest of Technical Papers*, San Francisco, CA, 2013, pp. 146-147.

[50] A. Tessmann *et al.,* "Metamorphic HEMT MMICs and modules for use in a high-bandwidth 210 GHz radar," *IEEE J. Solid State Circuits*, vol. 43, no. 10, pp. 2194–2205, Oct. 2008.

[51] I. Kallfass, J. Antes, T. Schneider, F. Kurz, D. Lopez-Diaz, S. Diebold*, et al.*, "All active MMIC-based wireless communication at 220 GHz," *Terahertz Science and Technology, IEEE Transactions on,* vol. 1, pp. 477-487, 2011.

[52] R. Appleby and R. N. Anderton, "Millimeter-wave and submillimeter-wave imaging for security and surveillance," *Proceedings of the IEEE,* vol. 95, pp. 1683-1690, 2007.

[53] S. Hu *et al.*, "A SiGe BiCMOS Transmitter/Receiver Chipset With On-Chip SIW Antennas for Terahertz Applications," in *IEEE Journal of Solid-State Circuits*, vol. 47, no. 11, pp. 2654-2664, Nov. 2012.

[54] A. Tang *et al.*, "A 144GHz 0.76cm-resolution sub-carrier SAR phase radar for 3D imaging in 65nm CMOS," *2012 IEEE International Solid-State Circuits Conference*, San Francisco, CA, 2012, pp. 264-266.

[55] N. Llombart, G. Chattopadhyay, A. Skalare and I. Mehdi, "Novel Terahertz Antenna Based on a Silicon Lens Fed by a Leaky Wave Enhanced Waveguide," in *IEEE Transactions on Antennas and Propagation*, vol. 59, no. 6, pp. 2160-2168, June 2011.

[56] S. Jameson, B. Khamaisi and E. Socher, "A +6dBm 128GHz source module with full F-band waveguide package and wirebonded CMOS chip," *2016 IEEE MTT-S International Microwave Symposium (IMS)*, San Francisco, CA, 2016, pp. 1-4.

[57] R. Dahlbäck, T. Bryllert, G. Granström, M. Ferndahl, V. Drakinskiy and J. Stake, "Compact 340 GHz homodyne transceiver modules for FMWC imaging radar arrays," *2016 IEEE MTT-S International Microwave Symposium (IMS)*, San Francisco, CA, 2016, pp. 1-4.

[58] S. Jameson and E. Socher, "A packaged 86–98 GHz CMOS transmitter for FMCW radar applications with 30 dBm of EIRP," *2015 IEEE MTT-S International Microwave Symposium*, Phoenix, AZ, 2015, pp. 1-4.

[59] T. Reck *et al.*, "A Silicon Micromachined Eight-Pixel Transceiver Array for Submillimeter-Wave Radar," in *IEEE Transactions on Terahertz Science and Technology*, vol. 5, no. 2, pp. 197-206, March 2015.

[60] T. Bryllert, V. Drakinskiy, K. B. Cooper and J. Stake, "Integrated 200–240-GHz FMCW Radar Transceiver Module," in *IEEE Transactions on Microwave Theory and Techniques*, vol. 61, no. 10, pp. 3808-3815, Oct. 2013.

[61] N. Llombart *et al.*, "Silicon Micromachined Lens Antenna for THz Integrated Heterodyne Arrays," in *IEEE Transactions on Terahertz Science and Technology*, vol. 3, no. 5, pp. 515-523, Sept. 2013.

[62] M. Abbasi *et al.*, "Single-Chip 220-GHz Active Heterodyne Receiver and Transmitter MMICs With On-Chip Integrated Antenna," in *IEEE Transactions on Microwave Theory and Techniques*, vol. 59, no. 2, pp. 466-478, Feb. 2011.

[63] J. Grzyb, K. Statnikov, N. Sarmah, B. Heinemann and U. R. Pfeiffer, "A 210–270-GHz Circularly Polarized FMCW Radar With a Single-Lens-Coupled SiGe HBT Chip," in *IEEE Transactions on Terahertz Science and Technology*, vol. 6, no. 6, pp. 771-783, Nov. 2016.

[64] A. Jam, J. R. East, and K. Sarabandi, “A Dual-Polarized Micromachined Beam-Steering Radar at 240 GHz for Collision Avoidance Applications,” 2017 *IEEE URSI General Assembly and Scientific Symposium*, Montreal, Canada, to be published.

[65] A. Jam, M. Vahidpour, J. R. East, and K. Sarabandi, "A Novel Frequency Beam-Steering Antenna Array at Y-Band," *IEEE International Antennas and Propagation Symposium*, Memphis, Tennessee, 2014.

[66] A. Jam, M. Vahidpour, J. East and K. Sarabandi, "A sub-millimeterwave micromachined frequency beam-steering antenna array," *IEEE International Microwave Symposium*, Tampa, Florida, 2014, pp. 1-3.

[67] K. Sarabandi, A. Jam, M. Vahidpour, and J. R. East, "A Novel Frequency Beam-Steering Antenna Array for Submillimeter-wave Applications-Part I: Design," *IEEE Transactions on Terahertz Science and Technology*, to be published.

[68] A. Jam, and K. Sarabandi, "A Horizontally Polarized Beam-Steerable Antenna for Sub-millimeter-wave Polarimetric Imaging and Collision Avoidance Radars," *IEEE international Antennas and Propagation Symposium,* Fajardo, Puerto Rico, 2016.

[69] M. Vahidpour, "A Millimeter-Wave Radar Microfabrication Technique and Its Application in Detection of Concealed Objects," The University of Michigan, 2012.

[70] A. Jam, M. Vahidpour, J. R. East, and K. Sarabandi, "A Novel Frequency Beam-Steering Antenna Array for Submillimeter-wave Applications-Part II: Microfabrication," *IEEE Transactions on Terahertz Science and Technology*, to be published.

[71] A. Jam, M. Vahidpour, J. R. East, and K. Sarabandi, "Microfabricaion and Measurement of a Sub-Millimeterwave Beam-Scanning Antenna Array at Y-band," *IEEE URSI General Assembly and Scientific Symposium*, Beijing, China, 2014.

[72] M. Moallem, "A Momolithic Millimeter-Wave Radar and Its Application in Detection of Concealed Objects," The University of Michigan, 2014.

[73] A. Jam, J. R. East, and K. Sarabandi, "A Novel Method for Chip Integration and Packaging for Millimeter-Wave to Terahertz Band Applications," *IEEE International Microwave Symposium*, Phoenix, Arizona, 2015.

[74] A. Jam, J. R. East, and K. Sarabandi, "A Micromachined Packaging with Incorporated RF-Choke for Integration of Active Chips at SubMillimeter-wave Frequencies," 2017 *IEEE International Microwave Symposium*, Honolulu, Hawaii, June 2017.

[75] M. Moallem, J. East and K. Sarabandi, "A Broadband, Micromachined Rectangular Waveguide to Cavity-Backed Coplanar Waveguide Transition Using Impedance-Taper Technique," in *IEEE Transactions on Terahertz Science and Technology*, vol. 4, no. 1, pp. 49-55, Jan. 2014.

[76] A. Jam, M. Moallem, J. East, and K. Sarabandi, "A Non-Contact Waveguide Probe for On-Wafer S-Parameter Measurements for Submillimeter-Wave to Terahertz Band," *IEEE Transactions on Terahertz Science and Technology*, vol. 4, no. 4, pp. 515-522, July 2014.

[77] A. Jam and K. Sarabandi, "A Sub-Millimeter-wave Near-Field Measurement Setup for On-Wafer Pattern and Gain Characterization of Antennas and Arrays," *IEEE Transactions on Instrumentation and Measurement*, vol. 66, no. 4, pp. 802-811, April 2017.

[78] K. L. Klohn, R. E. Horn, H. Jacobs, and E. Freibergs, “Silicon waveguide frequency scanning linear array antenna,” *IEEE Trans. Microwave Theory Tech*., vol. MTT-26, pp. 764–773, Oct. 1978.

[79] Manasson, et. al., "MMW scanning antenna," *IEEE Aerospace and Electronic Systems Magazine*, vol. 11, no. 10, pp. 29-33, Oct. 1996

[80] K. V. Caekenberghe, T. Vaha-Heikkila, G. Rebeiz, and K. Sarabandi, “Ka-band MEMS TTD passive electronically scanned array (ESA),” *in Proc. IEEE APS/URSI Symp*., Albuquerque, NM, Jul. 2006, pp. 513–516.

[81] B. Schoenlinner, X. Wu, J. Ebling, G. Eleftheriades, and G. Rebeiz, “Wide-scan spherical-lens antennas for automotive radars,” *IEEE Trans. Microw. Theory Tech*., vol. 50, no. 9, pp. 2166–2175, Sep. 2002.

[82] I. Bahl and K. Gupta, "Frequency scanning by leaky-wave antennas using artificial dielectrics," in *IEEE Transactions on Antennas and Propagation*, vol. 23, no. 4, pp. 584-589, July 1975.

[83] H. Y. Yee, “The design of large waveguide arrays of shunt slots,” *IEEE Trans. Antennas Propag*., vol. 40, pp. 775–781, 1992

[84] A. Patrovsky, and K. Wu, “Substrate integrated image guide array antenna for the upper millimeter-wave spectrum,” *IEEE Trans Antennas Propagat.*, vol. 55, pp. 2994-3001, Nov. 2007.

[85] R. E. Collin, *Foundations for Microwave Engineering,* New York: McGraw-Hill, 1966.

[86] A. Abbaspour-Tamijani and K. Sarabandi, "An affordable millimeter-wave beam-steerable antenna using interleaved planar subarrays," in *IEEE Transactions on Antennas and Propagation*, vol. 51, no. 9, pp. 2193-2202, Sep 2003.

[87] F. J. Goebels and T. S. Fong, “Four independent beams from a single linear array,” *IEEE Trans. Antennas Propagat*., vol. AP-13, pp. 683–691, Sept. 1965.

[88] Adib Y. Nashashibi, Amr A. Ibrahim, Samuel Cook, Kamal Sarabandi, "Experimental Characterization of Polarimetric Radar Backscatter Response of Distributed Targets at High Millimeter-Wave Frequencies", *Geoscience and Remote Sensing IEEE Transactions on*, vol. 54, pp. 1013-1024, 2016.

[89] M. Moallem and K. Sarabandi, "Polarimetric Study of MMW Imaging Radars for Indoor Navigation and Mapping," in *IEEE Transactions on Antennas and Propagation*, vol. 62, no. 1, pp. 500-504, Jan. 2014.

[90] K. Sarabandi and M. Park, "Extraction of power line maps from millimeter-wave polarimetric SAR images," in *IEEE Transactions on Antennas and Propagation*, vol. 48, no. 12, pp. 1802-1809, Dec 2000.

[91] K. Leong et al., "A 340 GHz integrated CB-CPW-to-waveguide transition for sub millimeter-wave MMIC packaging", *IEEE Microw. Wireless Compon. Lett.*, vol. 19, no. 6, pp. 413-415, Jun. 2009.

[92] L. Samoska, "An overview of solid-state integrated circuit ampliers in the submillimeter-wave and THz regime", *IEEE Trans. THz Sci. Tech*, vol. 1, no. 1, pp. 9-24, Sept. 2011.

[93] J.-H. Hwang and Y. Oh, "Millimeter-Wave Waveguide Slot-Array Antenna Covered by a Dielectric Slab and Arrayed Patches," *IEEE Antennas Wireless Propag. Lett*., vol.8, no., pp.1050-1053, 2009.

[94] M. Ando, J. Hirokawa, T. Yamamoto, A. Akiyama, Y. Kimura, Naohisa Goto, "Novel single-layer waveguides for high-efficiency millimeter-wave arrays," *IEEE Trans. Microwave Theory Tech*., vol.46, no.6, pp.792-799, Jun 1998.

[95] Al-Hasan, M.J.; Denidni, T.A.; Sebak, A.R., "Millimeter-Wave Compact EBG Structure for Mutual Coupling Reduction Applications," *in IEEE Transactions on Antennas and Propagation*, vol.63, no.2, pp.823-828, Feb. 2015.

[96] S. Beer, C. Rusch, H. Gulan, B. Gottel, M. G. Girma, J. Hasch, W. Winkler, W. Debski, T. Zwick, "An Integrated 122-GHz Antenna Array With Wire Bond Compensation for SMT Radar Sensors," *IEEE Trans. Antennas Propag.*, vol.61, no.12, pp.5976-5983, Dec. 2013.

[97] S. Beer, H. Gulan, C. Rusch, T. Zwick, "Integrated 122-GHz Antenna on a Flexible Polyimide Substrate With Flip Chip Interconnect," *IEEE Trans. Antennas Propag.*, vol.61, no.4, pp.1564-1572, April 2013.

[98] W. Lee, J. Kim, C. S. Cho, Y. J. Yoon, "Beamforming Lens Antenna on a High Resistivity Silicon Wafer for 60 GHz WPAN," *IEEE Trans. Antennas Propag.*, vol.58, no.3, pp.706-713, March 2010.

[99] X. Shang, M. Ke, Y. Wang and M. J. Lancaster, "WR-3 band waveguides and filters fabricated using SU8 photoresist micromachining technology", *IEEE Trans. THz Sci. Tech.* , vol. 2 , no. 6 , pp.477 -487 , 2012.

[100] X. Shang, Y. Tian, M.J. Lancaster, S. Singh, "A SU8 micromachined WR-1.5 band waveguide filter, " *IEEE Microwave and Wireless Components Letters*, vol.23, (6), pp.300-302, 2013.

[101] N. Llombart, C. Lee, M. Alonso-delPino, G. Chattopadhyay, C. Jung-Kubiak, L. Jofre, I. Mehdi, "Silicon Micromachined Lens Antenna for THz Integrated Heterodyne Arrays," *IEEE Trans. THz Sci. Tech.*, vol.3, no.5, pp.515-523, Sept. 2013.

[102] T.J. Reck, C. Jung-Kubiak, J. Gill, G. Chattopadhyay, "Measurement of Silicon Micromachined Waveguide Components at 500–750 GHz," *IEEE Trans. THz Sci. Tech.*, vol.4, no.1, pp.33-38, Jan. 2014.

[103] Microchem.com. (2017). SU-8 Negative Epoxy Series Resists - MicroChem. [online] Available at: http://www.microchem.com/Prod-SU8_KMPR.htm

[104] C. H. Tsau, S. M. Spearing, and M. A. Schmidt, "Characterization of wafer-level thermocompression bonds," *Microelectromechanical Systems, Journal of,* vol. 13, pp. 963-971, 2004.

[105] S. X. Jia, J. Wu, J. Zhu, and Y. X. Wang, "Study on the Gold-Gold Thermocompression Bonding for Wafer-Level Packaging," *Advanced Materials Research,* vol. 60, pp. 325-329, 2009.

[106] H. Sharifi, R. R. Lahiji, H. Lin, P. D. Ye, L. P. B. Katehi and S. Mohammadi, "Characterization of Parylene-N as Flexible Substrate and Passivation Layer for Microwave and Millimeter-Wave Integrated Circuits," *IEEE Trans. Adv. Packag.*, vol.32, no.1, pp.84-92, Feb. 2009.

[107] M. Moallem, K. Sarabandi, "Miniaturized-Element Frequency Selective Surfaces for Millimeter-Wave to Terahertz Applications," *IEEE Trans. THz Sci. Tech*, vol.2, no.3, pp.333-339, May 2012.

[108] H. Kim and K. Najafi, "Characterization of low-temperature wafer bonding using thin-film parylene," *J. Microelectromech. Syst.*, vol.14, no.6, pp.1347-1355, Dec. 2005

[109] DYMAX Corporation Torrington, U. (2017). 4-20418. [online] Dymax.com. Available at: http://www.dymax.com/index.php/adhesives/products/4-20418

[110] E. M. Godshalk, "A W-band wafer probe", *IEEE MTT-S Int. Microw. Symp. Dig.*, pp. 171-174, 1993.

[111] S. A. Wartenberg, "Selected topics in RF coplanar probing", *IEEE Trans. Microw. Theory Techn.*, vol. 51, no. 4, pp. 1413-1421, Apr. 2003.

[112] A. Fung, D. Dawson, L. Samoska, K. Lee, T. Gaier, P. Kangaslahti, C. Oleson, A. Denning, Y. Lau, G. Boll, "Two-port vector network analyzer measurements in the 218-344 and 356-500-GHz frequency bands", *IEEE Trans. Microw. Theory Techn.*, vol. 54, no. 12, pp. 4507-4512, Dec. 2006.

[113] P. Kirby, D. Pukala, H. Manohara, I. Mehdi, J. Papapolymerou, "Characterization of micromachined silicon rectangular waveguide at 400 GHz", *IEEE Microw. Wireless Compon. Lett.*, vol. 16, no. 6, pp. 366-368, June 2006.

[114] T. J. Reck, L. Chen, C. Zhang, A. Arsenovic, C. Groppi, A. W. Lichtenberger, R. M. Weikle, N. S. Barker, "Micromachined probes for submillimeter-wave on-wafer measurements—Part II: RF design and characterization", *IEEE Trans. THz Sci. Technol.*, vol. 1, no. 2, pp. 357-363, Nov. 2011.

[115] T. Skaik, Y. Wang, M. Ke, S. Qian, "A micromachined WR-3 waveguide with embedded bends for direct flange connections", *Eur. Microw. Conf.*, pp. 1225-1228, 2010-Sep.

[116] H. Gulan et al., "Probe based antenna measurements up to 325 GHz for upcoming millimeter-wave applications", *Proc. Int. Workshop Antenna Technol.*, pp. 228-231, Mar. 2013.

[117] A. D. Yaghjian, "An overview of near-field antenna measurements", *IEEE Trans. Antennas Propag.*, vol. 34, no. 1, pp. 30-45, Jan. 1986.

[118] D. Paris, W. Leach, E. B. Joy, "Basic theory of probe-compensated near-field measurements", *IEEE Trans. Antennas Propag.*, vol. 26, no. 3, pp. 373-379, May 1978.

[119] A. C. Newell, R. D. Ward, E. J. McFarlane, "Gain and power parameter measurements using planar near-field techniques", *IEEE Trans. Antennas Propag.*, vol. 36, no. 6, pp. 792-803, Jun. 1988.

[120] C. A. Balanis, Antenna Theory: Analysis and Design, New York, NY, USA:Wiley, pp. 1029-1030, 2005.

[121] M. Moallem and K. Sarabandi, "A Non-Contact Submillimeter-Wave S-Parameters Measurement Technique for Multiport Micromachined Devices," in *IEEE Transactions on Terahertz Science and Technology*, vol. 4, no. 3, pp. 338-346, May 2014.